NASA-CR-205022

ANALYSES OF TECHNOLOGY FOR SOLID STATE COHERENT LIDAR

CONTRACT No. NAS8-38609

Delivery Order No. 150

Contract Period:
October 1, 1995 - June 30, 1997

Submitted To:

NASA/MSFC
Marshall Space Flight Center, AL 35812

Prepared By:
Farzin Amzajerdian
Center For Applied Optics
University Of Alabama In Huntsville
Huntsville, Al 35899
(205) 890-6030 ext. 452

June 30, 1997

FOREWORD

This report describes the work performed under NASA contract NAS8-38609, Delivery Order number 150, over the period of October 1, 1995 through June 30, 1997.

ACKNOWLEDGMENTS

The author wishes to acknowledge Dr. Anees Ahmad, Ye Li, and Deborah R. Bailey for significantly contributing to this work by designing and analyzing the lidar optical and mechanical subsystems. The author would also like to acknowledge the other members of The Center for Applied Optics at UAH, in particular, Dr. John O. Dimmock and Freya W. Bailey for their support and valuable assistance.

CONTENTS

1.0 INTRODUCTION

Over past few years, considerable advances have been made in the areas of the diode-pumped, eye-safe, solid state lasers and room temperature, wide bandwidth, semiconductor detectors operating in the near-infrared region. These advances have created new possibilities for the development of reliable and compact coherent lidar systems for a wide range of applications. This research effort is aimed at further developing solid state coherent lidar technology for remote sensing of atmospheric processes such as wind, turbulence and aerosol concentration.

The work performed by the UAH personnel under this Delivery Order concentrated on design and analyses of laboratory experiments and measurements, and development of advanced lidar optical subsystems in support of solid state laser radar remote sensing systems which are to be designed, deployed, and used to measure atmospheric processes and constituents. Under this delivery order, a lidar breadboard system was designed and analyzed by considering the major aircraft and space operational requirements. The lidar optical system was analyzed in detail using SYNOPSIS and Code V optical design packages. The lidar optical system include a wedge scanner and the compact telescope designed by the UAH personnel. The other major optical components included in the design and analyses were: polarizing beam splitter, routing mirrors, wave plates, signal beam derotator, and lag angle compensator. This lidar system is to be used for demonstrating all the critical technologies for the development of a reliable and low-cost space-based instrument capable of measuring global wind fields. A number of laboratory experiments and measurements were performed at the NASA/MSFC Detector Characterization Facility, previously developed by the UAH personnel. These laboratory measurements include the characterization of a 2-micron InGaAs detectors suitable for use in coherent lidars and characterization of Holographic Optical Element Scanners.

UAH personnel actively participated in the development of performance and operational requirements for the development of the high pulse energy transmitter laser and frequency-agile local oscillator laser, that are in-progress at NASA Langley Research Center and Jet Propulsion Laboratory. During the period of performance of this delivery order, UAH personnel participated several technical coordination meetings with the other NASA centers, and attended several meetings and conferences to report on the progresses and accomplishments made under this work.

2.0 DETECTOR CHARACTERIZATION

2.1 INTRODUCTION

A number of semiconductor detectors, operating at 2 micron wavelength region, were characterized and their heterodyne detection properties were analyzed. The detector measurements were performed using the Detector Characterization Facility (DCF) that had previously been developed by the UAH personnel at NASA/MSFC. A detail description of the DCF design and capabilities was provided in the NASA report NAS8-38609/DO77[1], and the DFC principles of measurements, calibration and data analysis procedures were reported in the NASA report NAS8-38609/DO 118[2]. The DCF is capable of providing all the necessary detection parameters for design, development and calibration of coherent and incoherent solid state laser radar (lidar) systems. The coherent lidars in particular require an accurate knowledge of detector heterodyne quantum efficiency[3-5], nonlinearity properties[6-8] and voltage-current relationship[9-11] as a function of applied optical power. At present no detector manufacturer provides these quantities or adequately characterizes their detectors for heterodyne detection operation. In addition, the detector characterization facility measures the detectors DC and AC quantum efficiencies noise equivalent power and frequency response up to several GHz. The DCF is also capable of evaluating various heterodyne detection schemes such as balanced detectors and fiber optic interferometers. It should also be noted that the DCF design was further improved to allow for characterization of diffractive and holographic optical elements and other critical optical components of coherent lidar systems.

2.2 CHARACTERIZATION OF A 2-MICRON InGaAs DETECTOR

A number of 75 microns diameter InGaAs detector with a cutoff wavelength of 2.5 microns, acquired from Sensors Unlimited and Epitaxx were fully characterized in the NASA/MSFC Detector Characterization Facility. The following data are the results of the measurements performed on a Sensors Unlimited detector identified by model number: SU75-2.5TO and serial number: 3495S4061.

RESPONSIVITY AND LINEARITY MEASUREMENTS

V_B=0.00 V

Notes:
Detector anode terminated by 50 ohms
With laser beam blocked, InAs laser power monitor detector reads 18.9 mV and detector direct output is 0.0 mV.

InAs Power Monitor (mV)	Detector Output (mV)	Incident Power P_{in} (mW)	Detector current I_d (mA)
117	12.5	0.254	0.2432
120	13.0	0.261	0.2529
174	19.6	0.391	0.3813
204	23.1	0.464	0.4494
308	35.0	0.714	0.6809
410	45.7	0.960	0.8891
454	50.2	1.066	0.9767
518	55.9	1.220	1.0875
596	62.3	1.408	1.2121
718	70.3	1.702	1.3677
802	74.5	1.905	1.4494
907	78.7	2.158	1.5311
1015	82.2	2.418	1.5992
1111	84.6	2.650	1.6459
1238	87.3	2.956	1.6984
1317	88.8	3.146	1.7276
1394	89.9	3.332	1.7490
1493	91.3	3.570	1.7763
1539	91.8	3.681	1.7860

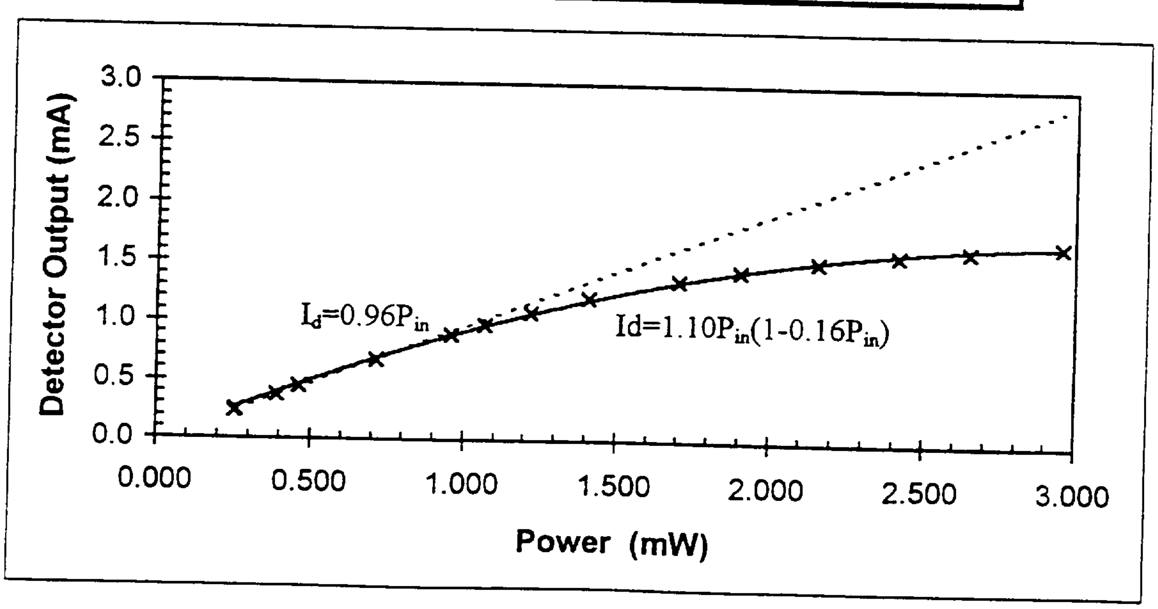

V_B=1.00 V

Notes:
With laser beam blocked, InAs laser power monitor detector reads 19.0 mV and detector direct output is 0.0 mV.

InAs Power Monitor (mV)	Detector Output (mV)	Incident Power P_{in} (mW)	Detector current I_d (mA)
118	13.1	0.256	0.2549
156	18.1	0.348	0.3521
203	24.0	0.461	0.4669
306	36.9	0.709	0.7179
354	42.2	0.825	0.8210
405	47.9	0.948	0.9319
514	55.0	1.211	1.0700
619	56.8	1.464	1.1051
716	57.6	1.698	1.1206
819	58.1	1.946	1.1304
907	58.4	2.158	1.1362
1010	58.7	2.406	1.1420
1108	58.9	2.642	1.1459
1253	59.1	2.992	1.1498
1429	59.4	3.416	1.1556
1656	59.6	3.963	1.1595

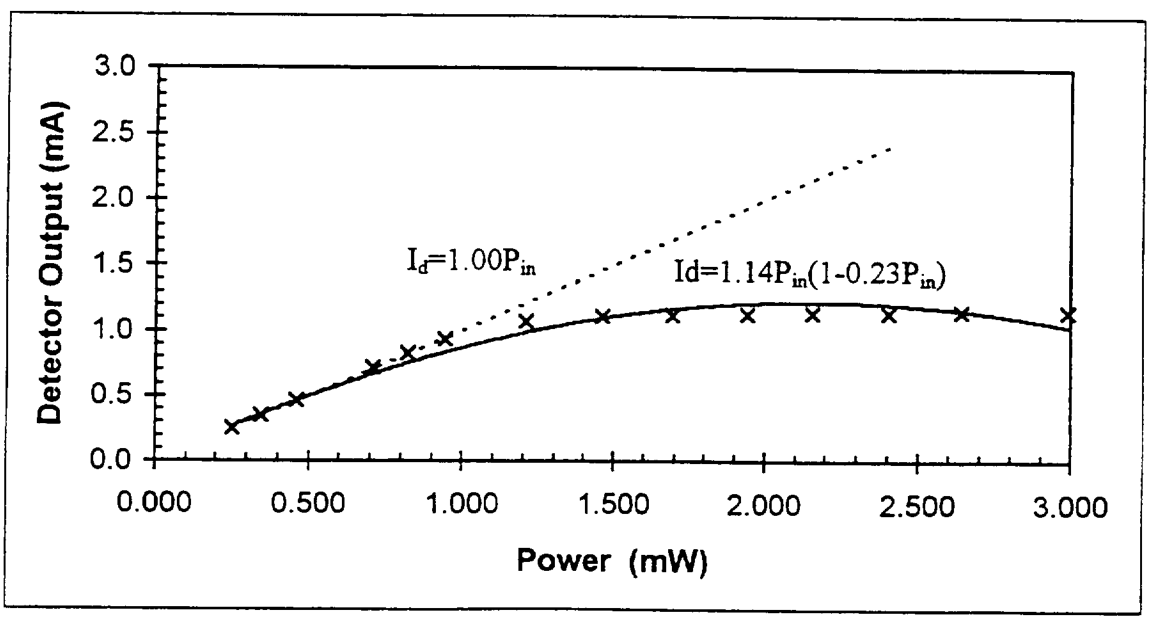

V_B=1.50 V

Notes:
With laser beam blocked, InAs laser power monitor detector reads 18.8 mV and detector direct output is 0.0 mV.

InAs Power Monitor (mV)	Detector Output (mV)	Incident Power P_{in} (mW)	Detector current I_d (mA)
103	12.0	0.220	0.2335
136	16.6	0.300	0.3230
190	23.7	0.430	0.4611
218	27.4	0.497	0.5331
286	35.6	0.661	0.6926
348	42.7	0.811	0.8307
411	49.7	0.963	0.9669
557	63.4	1.314	1.2335
637	69.9	1.507	1.3599
750	76.6	1.780	1.4903
892	79.7	2.122	1.5506
1129	81.2	2.693	1.5798
1316	81.8	3.144	1.5914
1530	82.3	3.659	1.6012
1664	82.5	3.982	1.6051
1798	82.6	4.305	1.6070

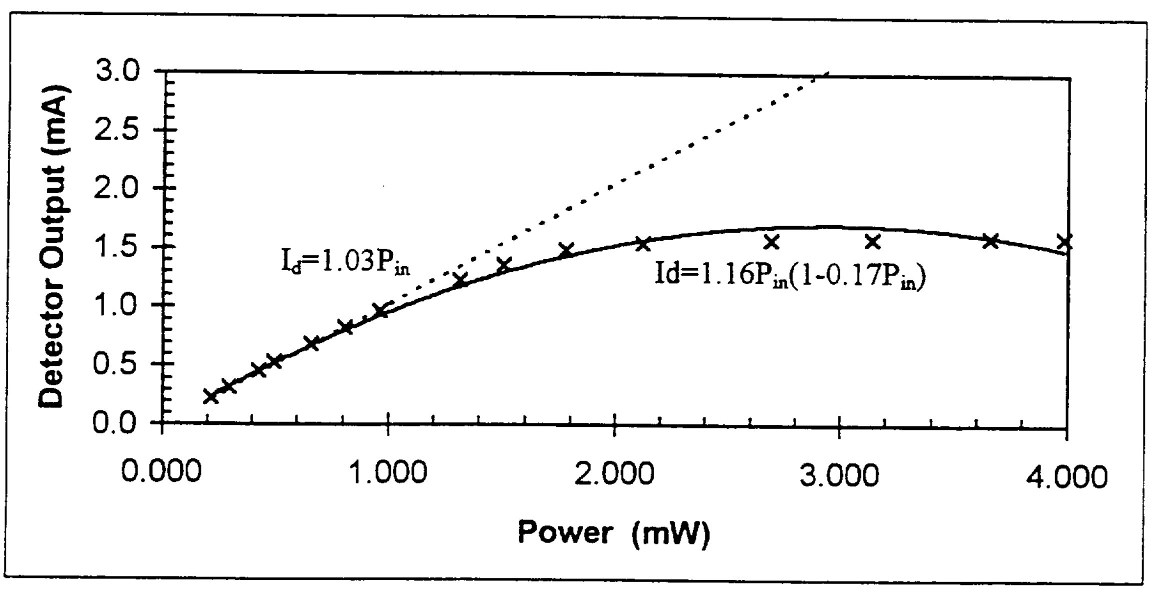

V_B=2.00 V

Notes:
With laser beam blocked, InAs laser power monitor detector reads 19.8 mV and detector direct output is 0.0 mV.

InAs Power Monitor (mV)	Detector Output (mV)	Incident Power P_{in} (mW)	Detector current I_d (mA)
117	14.0	0.254	0.2724
138	17.0	0.305	0.3307
161	20.0	0.360	0.3891
203	25.7	0.461	0.5000
300	37.9	0.695	0.7374
410	51.0	0.960	0.9922
440	54.1	1.032	1.0525
505	61.1	1.189	1.1887
636	73.9	1.505	1.4377
728	82.1	1.726	1.5973
811	88.5	1.927	1.7218
902	94.9	2.146	1.8463
1050	101.5	2.503	1.9747
1242	104.0	2.965	2.0233
1426	104.9	3.409	2.0409
1565	105.3	3.744	2.0486
1664	105.5	3.982	2.0525
1775	105.7	4.250	2.0564

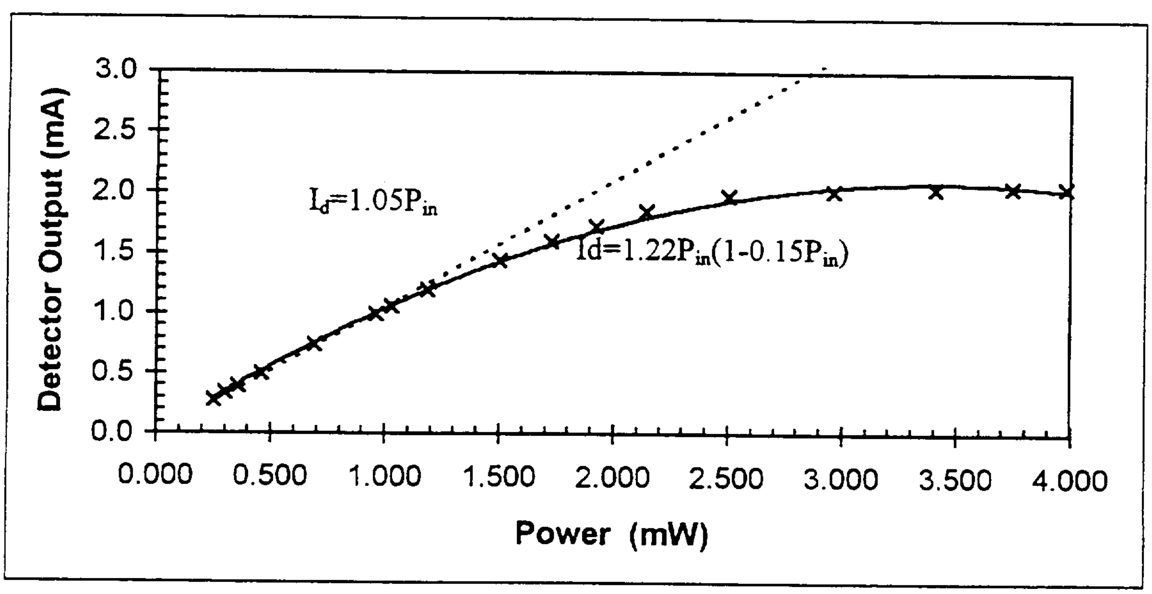

V_B=2.50 V

Notes:
With laser beam blocked, InAs laser power monitor detector reads 20.1 mV and detector direct output is 0.06 mV.

InAs Power Monitor (mV)	Detector Output (mV)	Incident Power P_{in} (mW)	Detector current I_d (mA)
110	13.2	0.237	0.2556
139	17.2	0.307	0.3335
172	21.8	0.387	0.4230
222	28.7	0.507	0.5572
325	41.6	0.755	0.8082
461	57.5	1.083	1.1175
559	68.5	1.319	1.3315
690	81.9	1.635	1.5922
757	88.1	1.796	1.7128
870	98.0	2.069	1.9054
930	103.2	2.213	2.0066
1179	119.9	2.813	2.3315
1292	124.3	3.086	2.4171
1520	127.2	3.635	2.4735
1670	128.0	3.997	2.4891
1815	128.5	4.346	2.4988
1905	128.7	4.563	2.5027

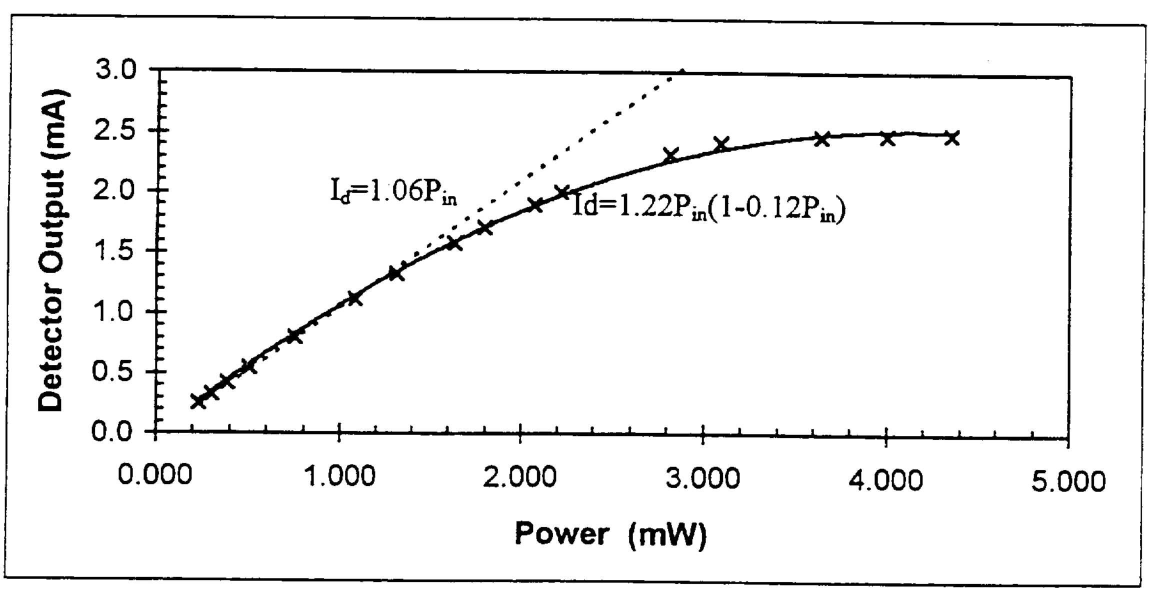

V_B=3.00 V

Notes:
With laser beam blocked, InAs laser power monitor detector reads 20.4 mV and detector direct output is 0.1 mV.

InAs Power Monitor (mV)	Detector Output (mV)	Incident Power P_{in} (mW)	Detector current I_d (mA)
116	14.2	0.252	0.2743
137	17.3	0.302	0.3346
179	23.2	0.403	0.4494
203	26.4	0.461	0.5117
256	33.7	0.589	0.6537
352	46.1	0.820	0.8949
448	57.8	1.052	1.1226
545	68.8	1.285	1.3366
700	85.5	1.659	1.6615
759	91.5	1.801	1.7782
843	99	2.004	1.9241
990	112.8	2.358	2.1926
1128	124.6	2.690	2.4222
1300	137.2	3.105	2.6673
1453	144.7	3.474	2.8132
1580	148.7	3.780	2.8911
1744	150.4	4.175	2.9241
1895	151.2	4.539	2.9397
2015	151.7	4.828	2.9494

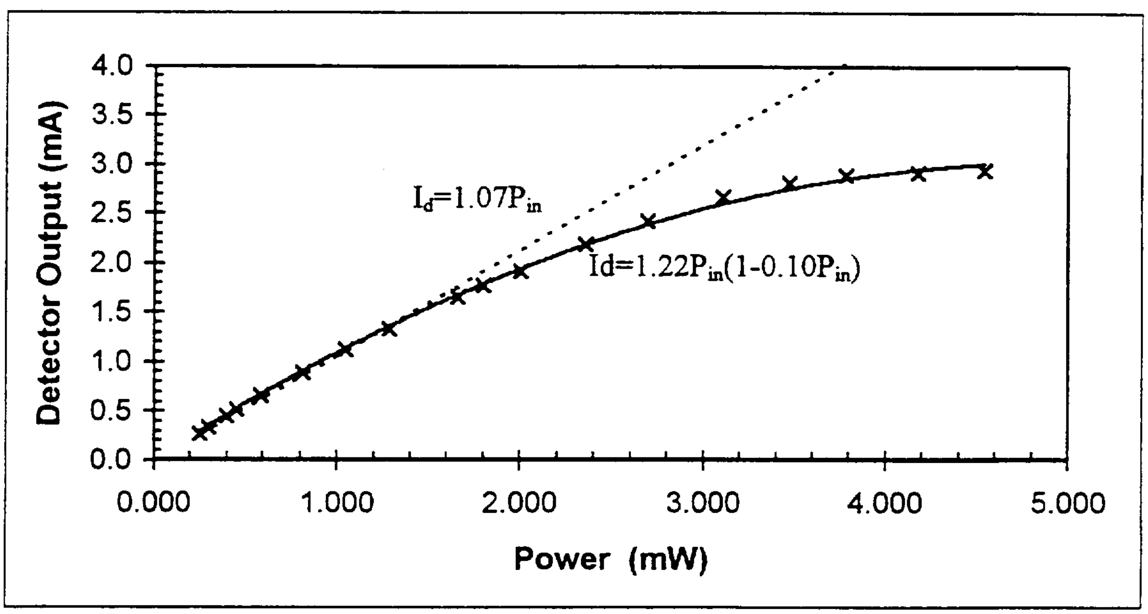

V_B=3.50 V

Notes:
With laser beam blocked, InAs laser power monitor detector reads 20.3 mV and detector direct output is 0.1 mV.

InAs Power Monitor (mV)	Detector Output (mV)	Incident Power P_{in} (mW)	Detector current I_d (mA)
113	14.0	0.244	0.2704
151	19.6	0.336	0.3794
192	25.4	0.435	0.4922
237	31.8	0.543	0.6167
302	40.5	0.700	0.7860
418	55.4	0.979	1.0759
518	67.4	1.220	1.3093
621	79.1	1.469	1.5370
784	96.2	1.861	1.8696
876	105.6	2.083	2.0525
952	112.8	2.266	2.1926
1090	125.5	2.599	2.4397
1200	135.0	2.864	2.6245
1365	147.9	3.262	2.8755
1517	158.4	3.628	3.0798
1725	169.1	4.129	3.2879
1904	173.3	4.561	3.3696
2034	174.4	4.874	3.3911

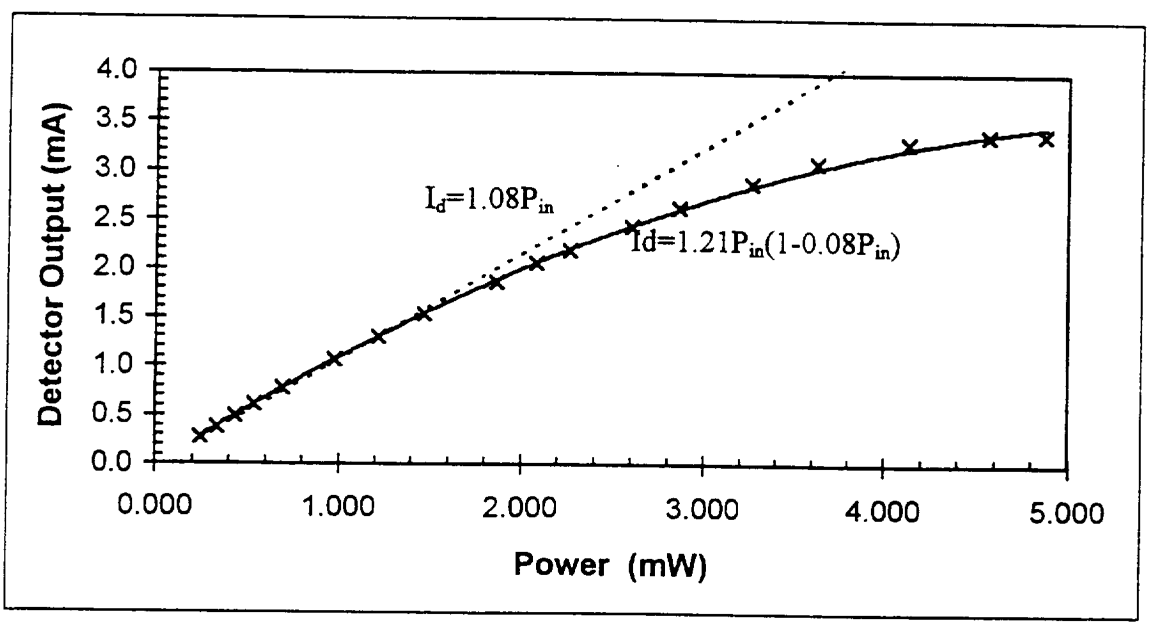

V_B=4.00 V

Notes:
With laser beam blocked, InAs laser power monitor detector reads 20.6mV and detector direct output is 0.2 mV.

InAs Power Monitor (mV)	Detector Output (mV)	Incident Power P_{in} (mW)	Detector current I_d (mA)
117	14.9	0.254	0.2860
137	17.8	0.302	0.3424
156	20.7	0.348	0.3988
207	28.1	0.471	0.5428
278	38.2	0.642	0.7393
335	46.0	0.779	0.8911
437	59.4	1.025	1.1518
512	68.8	1.206	1.3346
617	81.2	1.459	1.5759
712	92.0	1.688	1.7860
819	103.2	1.946	2.0039
950	116.4	2.262	2.2607
1060	127.1	2.527	2.4689
1221	142.9	2.915	2.7763
1385	156.4	3.310	3.0389
1535	169.4	3.671	3.2918
1763	185.6	4.221	3.6070
1912	194.6	4.580	3.7821
2042	200.6	4.893	3.8988
2206	204.2	5.288	3.9689

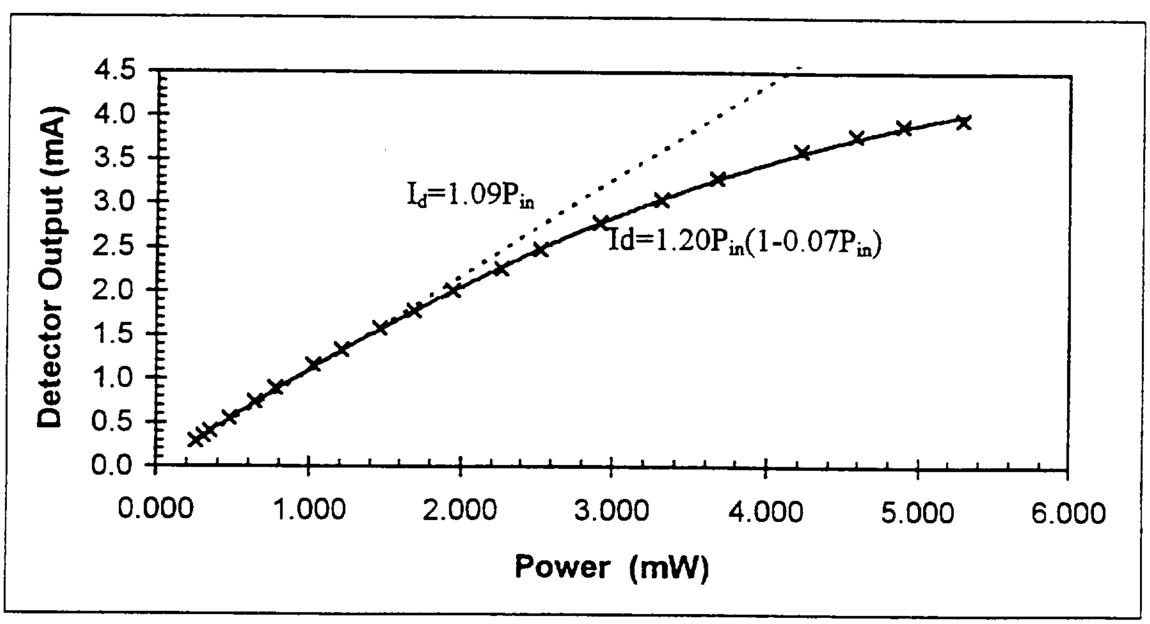

V_B=4.50 V

Notes:
With laser beam blocked, InAs laser power monitor detector reads 20.8 mV and detector direct output is 0.2 mV.

InAs Power Monitor (mV)	Detector Output (mV)	Incident Power P_{in} (mW)	Detector current I_d (mA)
119	15.3	0.259	0.2938
148	19.9	0.329	0.3833
177	24.2	0.399	0.4669
208	28.8	0.473	0.5564
307	43.1	0.712	0.8346
404	56.4	0.946	1.0934
518	71.2	1.220	1.3813
632	84.6	1.495	1.6420
704	93.4	1.669	1.8132
830	106.8	1.972	2.0739
908	115.2	2.160	2.2374
1041	128.8	2.481	2.5019
1191	143.1	2.842	2.7802
1441	164.8	3.445	3.2023
1698	186.1	4.064	3.6167
1930	202.1	4.623	3.9280
2055	209.8	4.925	4.0778
2191	214.9	5.252	4.1770

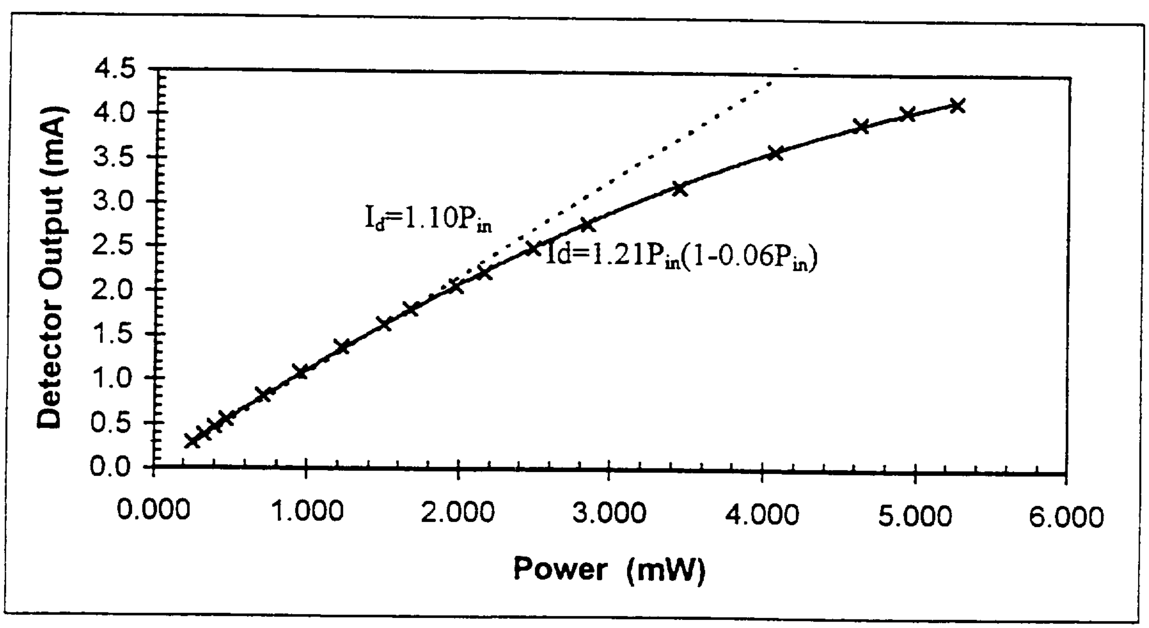

V_B=5.00 V

Notes:
With laser beam blocked, InAs laser power monitor detector reads 20.6 mV and detector direct output is 0.3 mV.

InAs Power Monitor (mV)	Detector Output (mV)	Incident Power P_{in} (mW)	Detector current I_d (mA)
124	16.4	0.271	0.3132
156	21.4	0.348	0.4105
168	23.2	0.377	0.4455
201	28.2	0.456	0.5428
309	44.1	0.717	0.8521
418	59.4	0.979	1.1498
524	73.3	1.235	1.4202
609	83.7	1.440	1.6226
722	97.4	1.712	1.8891
821	108.7	1.951	2.1089
932	120.4	2.218	2.3366
1086	136.2	2.589	2.6440
1198	146.6	2.859	2.8463
1340	159.6	3.201	3.0992
1584	180.4	3.789	3.5039
1700	189.9	4.069	3.6887
1820	197.7	4.358	3.8405
1919	206.9	4.597	4.0195
2085	218.4	4.997	4.2432
2203	225.7	5.281	4.3852
2288	230.7	5.486	4.4825
2367	236.1	5.676	4.5875

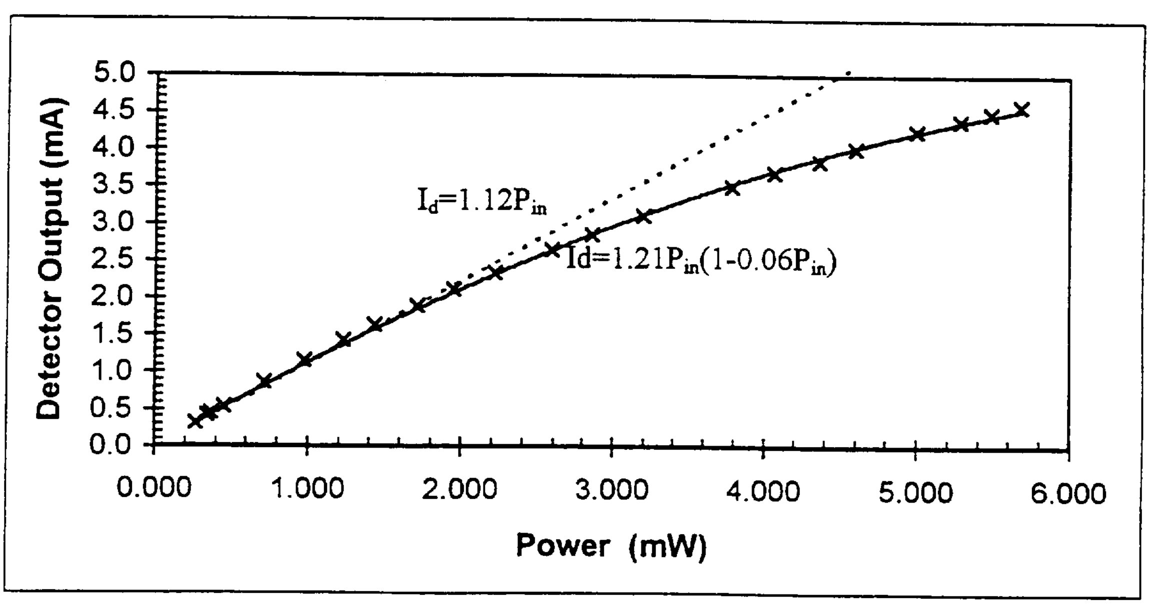

V_B=5.50 V

Notes:
With laser beam blocked, InAs laser power monitor detector reads 20.9 mV and detector direct output is 0.3 mV.

InAs Power Monitor (mV)	Detector Output (mV)	Incident Power P_{in} (mW)	Detector current I_d (mA)
118	15.8	0.256	0.3016
145	20.0	0.321	0.3833
199	28.3	0.452	0.5447
298	43.6	0.690	0.8424
406	59.0	0.950	1.1420
503	72.7	1.184	1.4086
612	87.0	1.447	1.6868
707	98.3	1.676	1.9066
811	110.9	1.927	2.1518
920	123.2	2.189	2.3911
1052	137.6	2.507	2.6712
1208	153.4	2.883	2.9786
1419	172.3	3.392	3.3463
1603	188.7	3.835	3.6654
1840	208.1	4.406	4.0428
2050	224.9	4.913	4.3696
2216	237.7	5.313	4.6187
2388	248.0	5.727	4.8191

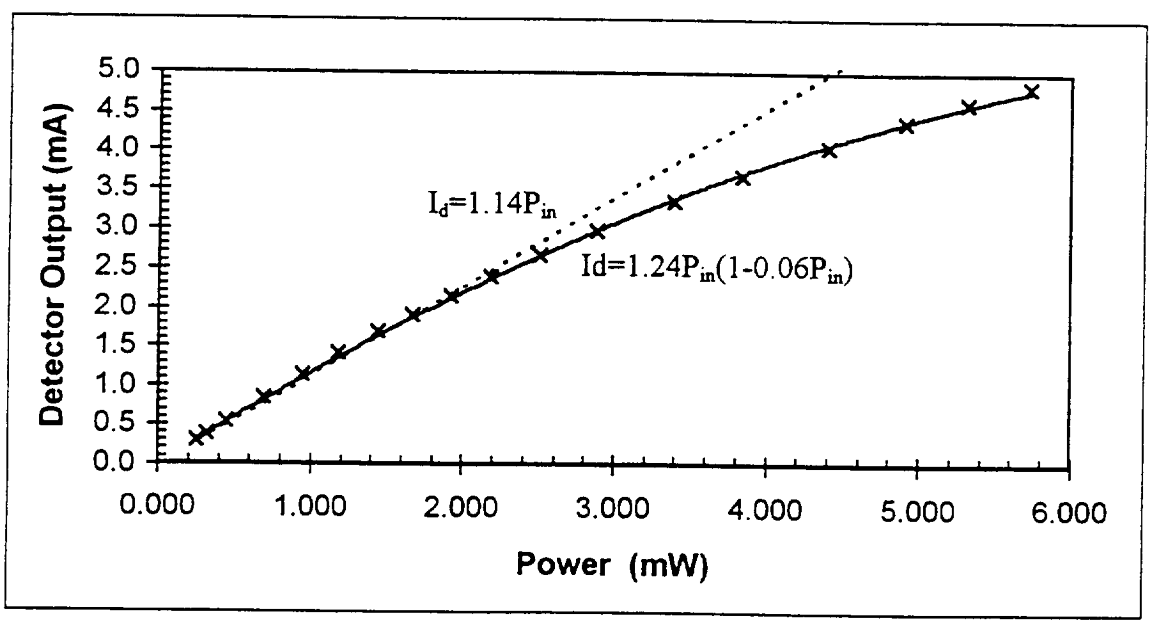

Detector Responsivity and Linearity
Summary Of Results

V_B (V)	Linear Responsivity ρ_0 (A/W)	Linear Responsivity η_{DC}	Non-Linear Responsivity ρ (mA/mW)	Non-Linear Responsivity α (1/mW)
0.00	0.96	0.5763	1.10	0.16
1.00	1.00	0.6004	1.14	0.23
1.50	1.03	0.6184	1.16	0.17
2.00	1.05	0.6304	1.22	0.15
2.50	1.06	0.6364	1.22	0.12
3.00	1.07	0.6424	1.22	0.10
3.50	1.08	0.6484	1.21	0.08
4.00	1.09	0.6544	1.20	0.07
4.50	1.10	0.6604	1.21	0.06
5.00	1.12	0.6724	1.21	0.06
5.50	1.14	0.6844	1.24	0.06

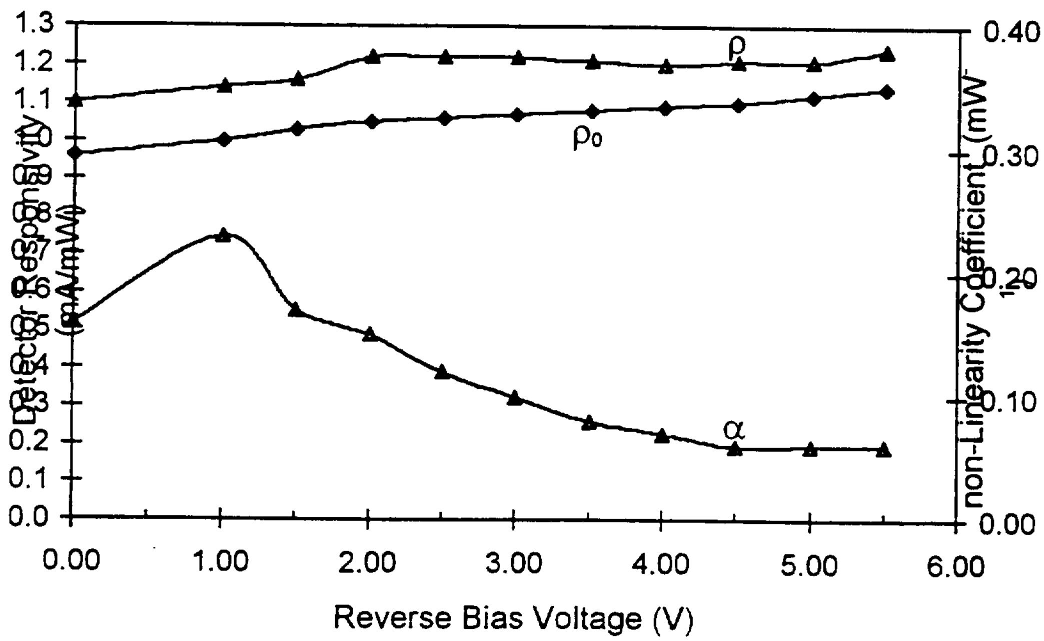

Optimum Local Oscillator Power

$$SNR = (\rho P_s/Be)\,\frac{(1-2\alpha P_{LO})^2 P_{LO}}{P_{LO}(1-\alpha P_{LO})+(2KT_e/\rho eR_e)}$$

For V_B =5.0V and T_e=300, the signal-to-noise ratio is shown below as a function of local oscillator power.

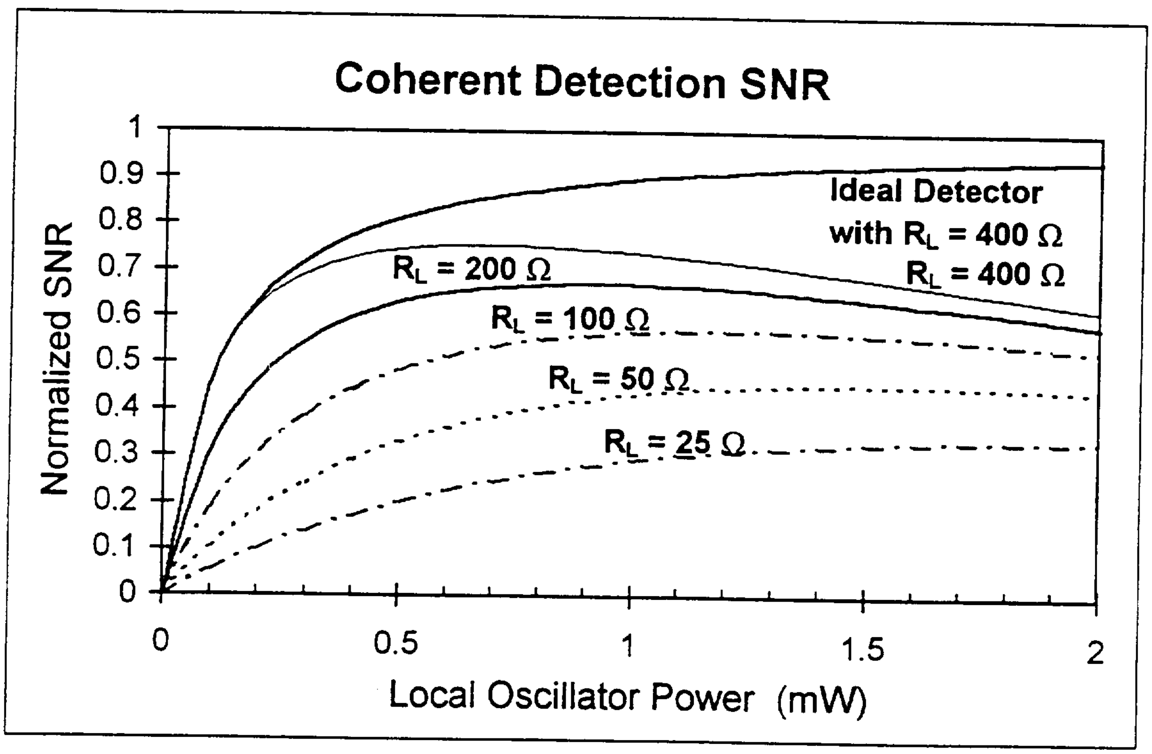

For a 50 ohms load, the optimum local oscillator power is 1.53 mW.

Voltage-Current Characteristics

Optical Power=0.0

Bias Current Monitor V_{Bi} (mV)	Bias Voltage Monitor V_B (mV)	Detector Voltage V_d (V)	Detector Current I_d (μA)	Detector Resistance R_d (Ω)
1756.0	353.0	0.280304	1414.315	
1731.0	351.0	0.279496	1391.129	24.9
1686.0	348.0	0.278672	1348.790	25.9
1648.0	345.0	0.277486	1313.508	42.0
1535.0	335.0	0.272823	1209.677	44.1
1500.0	332.0	0.271481	1177.419	35.4
1448.0	328.0	0.269968	1129.032	41.7
1197.0	306.0	0.259833	898.185	45.6
1100.0	297.0	0.255393	809.476	49.7
1024.0	290.0	0.251968	739.919	56.1
967.0	284.0	0.248611	688.508	79.8
536.0	233.0	0.217300	305.444	82.2
512.0	230.0	0.215388	284.274	133.4
415.0	214.0	0.203585	202.621	209.4
267.0	179.0	0.174440	88.710	382.6
162.0	137.0	0.135705	25.202	713.5
140.9	124.1	0.123230	16.935	2014.8
109.9	101.8	0.101380	8.165	3321.4
83.7	79.9	0.079703	3.831	10288.3
20.8	20.5	0.020484	0.302	18851.7
11.5	11.3	0.011290	0.202	52855.3
4.5	4.5	0.004500	0.000	51201.9
-4.3	-4.2	-0.004195	-0.101	360044.6
-31.9	-31.8	-0.031795	-0.101	542572.6
-59.1	-58.9	-0.058890	-0.202	305179.4
-72.0	-71.8	-0.071788	-0.232	1163068.6
-106.0	-105.8	-0.105788	-0.242	3174348.6
-200.1	-199.8	-0.199786	-0.272	3172695.3
-298.0	-297.7	-0.297684	-0.302	3965964.6
-400.0	-399.7	-0.399683	-0.323	1949228.6
-494.6	-494.2	-0.494179	-0.403	1186490.8
-615.5	-615.0	-0.614974	-0.504	1557884.6
-808.9	-808.3	-0.808269	-0.605	3375228.6
-1023.9	-1023.3	-1.023268	-0.625	3883628.6
-1513.8	-1513.0	-1.512960	-0.786	3679914.3
-2062.9	-2062.0	-2.061953	-0.907	4752530.4
-2568.0	-2567	-2.566948	-1.008	875614.1
-3035.0	-3033	-3.032896	-2.016	1403444.9
-4097.1	-4095	-4.094892	-2.097	1482988.6
-4531.0	-4528	-4.527845	-3.024	1952948.6

Bias Current Monitor V_{Bi} (mV)	Bias Voltage Monitor V_B (mV)	Detector Voltage V_d (V)	Detector Current I_d (μA)	Detector Resistance R_d (Ω)
-5228	-5224	-5.223793	-4.032	493964.6
-6028	-6022	-6.021689	-6.048	367187.0
-7084	-7075	-7.074534	-9.073	378148.6
-7557	-7547	-7.546482	-10.081	479084.6
-8052	-8041	-8.040430	-11.089	451308.6
-8925	-8912	-8.911326	-13.105	352902.2
-9836	-9820	-9.819171	-16.129	

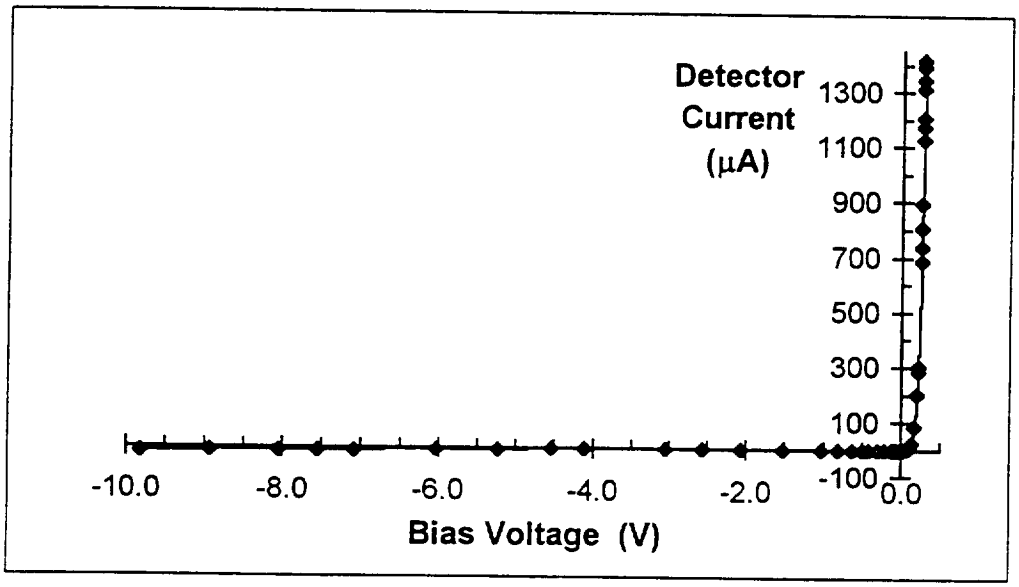

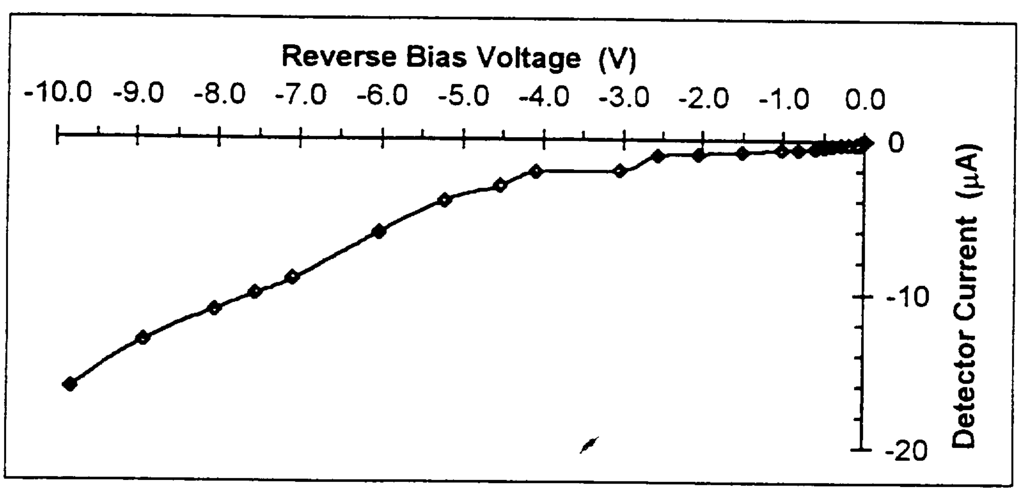

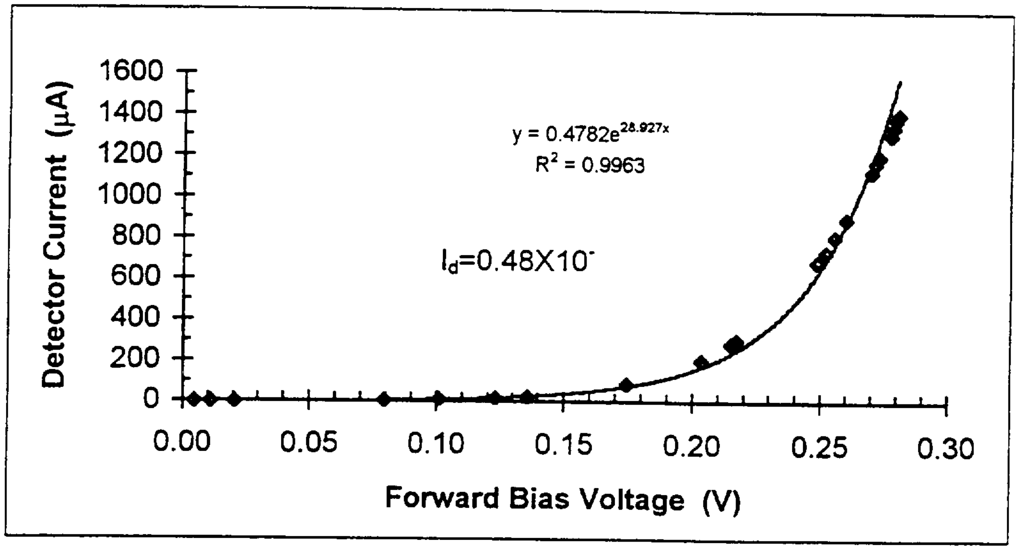

V-I Characteristic equation:

$I_d=0.48X10^{-6}exp(28.93V_d)$ V_d>50mV

$I_d=0.90X10^{-6}(exp(20.91V_d)-1)$ V_d<50mV

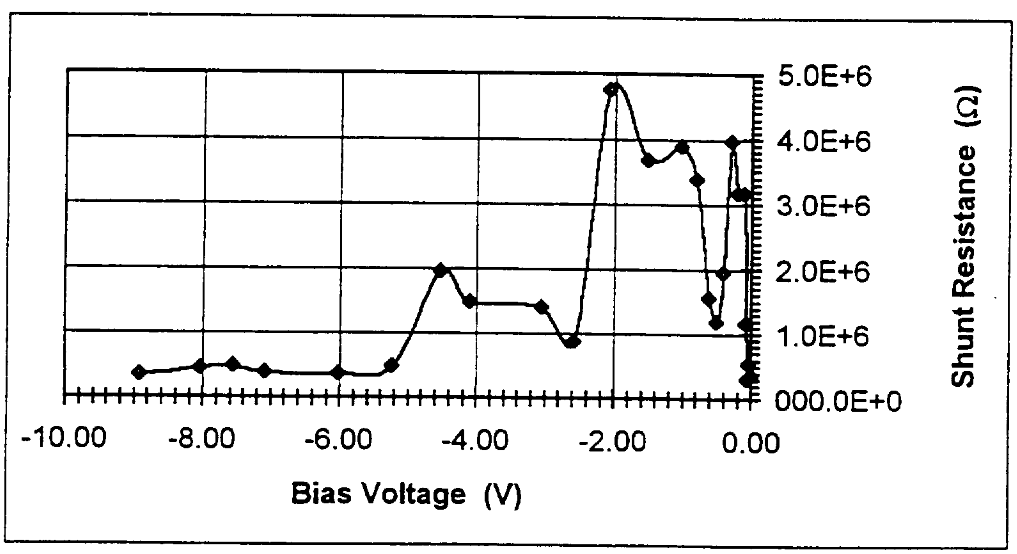

$1/R_f = dI_d/dV_d$

$R_f = 7.20 X 10^4 \exp(-28.93 V_d)$

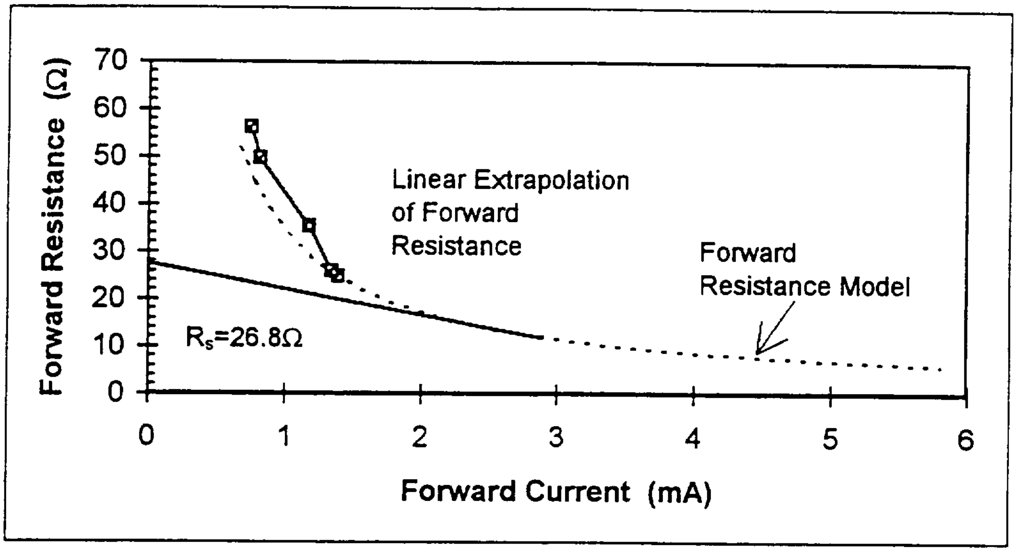

Optical Power=0.5mW

InAs Monitor=260mV

Bias Current Monitor V_{Bi} (mV)	Bias Voltage Monitor V_B (mV)	Detector Voltage V_d (V)	Detector Current I_d (μA)	Detector Resistance R_d (Ω)
1745.0	355.0	0.28298	1401.210	45.4
1700.0	351.0	0.28110	1359.879	27.3
1632.0	346.0	0.27937	1296.371	50.9
1525.0	336.0	0.27439	1198.589	7.0
1435.0	331.0	0.27380	1112.903	37.7
1310.0	320.7	0.26944	997.278	35.1
1214.0	313.0	0.26632	908.266	47.8
1115.0	304.0	0.26198	817.540	39.6
996.0	294.0	0.25763	707.661	34.9
971.0	292.0	0.25682	684.476	51.4
460.0	244.0	0.23281	217.742	78.7
391.0	236.0	0.22797	156.250	14.7
375.0	235.0	0.22775	141.129	84.9
226.0	217.0	0.21653	9.073	96.8
126.0	204.0	0.20804	-78.629	209.0
20.2	182.0	0.19038	-163.105	133.4
-169.6	152.2	0.16887	-324.395	604.3
-345.0	82.4	0.10455	-430.847	1421.9
-429.0	32.2	0.05610	-464.919	7087.7
-479.0	-11.7	0.01251	-471.069	8944.1
-627.0	-145.0	-0.12003	-485.887	50143.8
-885.0	-398.0	-0.37277	-490.927	61452.6
-1011	-522	-0.49666	-492.944	407660.6
-1423	-933	-0.90761	-493.952	78316.6
-1663	-1170	-1.14446	-496.976	377900.6
-2045	-1551	-1.52540	-497.984	506860.6
-2557	-2062	-2.03635	-498.992	569356.6
-3132	-2636	-2.61030	-500.000	395756.6
-3532	-3035	-3.00925	-501.008	67900.6
-4088	-3583	-3.55683	-509.073	86252.6
-4528	-4018	-3.99157	-514.113	28016.4
-5026	-4499	-4.47169	-531.250	47706.3
-6058	-5510	-5.48161	-552.419	40350.1
-6517	-5958	-5.92904	-563.508	54839.3
-7024	-6456	-6.42657	-572.581	74348.6
-7480	-6906	-6.87626	-578.629	58697.0
-8022	-7439	-7.40879	-587.702	51753.0
-8501	-7909	-7.87833	-596.774	19739.0
-8920	-8308	-8.27629	-616.935	34952.0
-9174	-8555	-8.52293	-623.992	

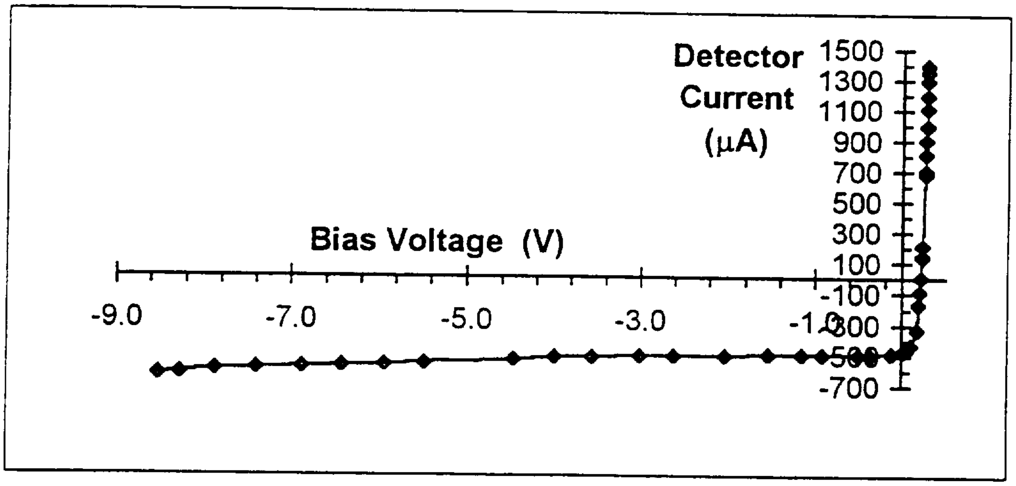
Detector Current (μA)
1500
1300
1100
900
700
500
300
100
-100
-300
-500
-700
Bias Voltage (V)
-9.0
-7.0
-5.0
-3.0
-1.0

Optical Power=1.0mW

InAs Monitor=423mV

Bias Current Monitor V_{Bi} (mV)	Bias Voltage Monitor V_B (mV)	Detector Voltage V_d (V)	Detector Current I_d (μA)	Detector Resistance R_d (Ω)
1758	358	0.285460	1411.290	19.5
1743	357	0.285185	1397.177	24.9
1659	351	0.283227	1318.548	29.6
1500	339	0.278843	1170.363	31.7
1306	324	0.273118	989.919	39.7
1199	315	0.269196	891.129	35.3
1000	299	0.262678	706.653	33.4
340	247	0.242181	93.750	93.5
238	234	0.233793	4.032	53.4
102	221	0.227166	-119.960	68.5
0	210	0.220881	-211.694	72.6
-99	199	0.214441	-300.403	66.9
-221	186	0.207089	-410.282	84.8
-337	172	0.198374	-513.105	116.2
-510	147	0.181042	-662.298	220.6
-747	96	0.139680	-849.798	1168.4
-1048	-70	-0.019325	-985.887	12377.8
-1508	-496	-0.443564	-1020.161	35792.9
-2065	-1038	-0.984786	-1035.282	71372.6
-2503	-1470	-1.416476	-1041.331	56161.9
-3022	-1980	-1.926009	-1050.403	25299.7
-3500	-2440	-2.385077	-1068.548	19788.6
-4004	-2920	-2.863833	-1092.742	27614.4
-4524	-3422	-3.364900	-1110.887	46211.9
-5048	-3935	-3.877330	-1121.976	22667.8
-6028	-4874	-4.814206	-1163.306	21051.1
-7008	-5810	-5.747926	-1207.661	15971.9
-8020	-6763	-6.697869	-1267.137	25660.2
-9016	-7722	-7.654952	-1304.435	38282.3
-9571	-8263	-8.195227	-1318.548	

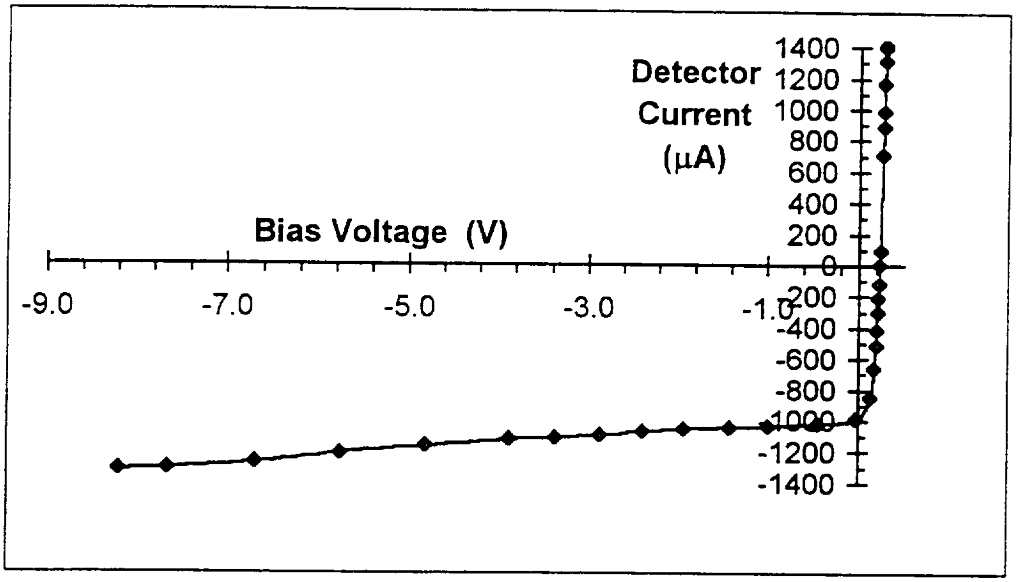
Detector Current (μA)
1400
1200
1000
800
600
400
200
0
-200
-400
-600
-800
-1000
-1200
-1400
Bias Voltage (V)
-9.0
-7.0
-5.0
-3.0
-1.0

Optical Power=1.5mW

InAs Monitor=625mV

Bias Current Monitor V_{Bi} (mV)	Bias Voltage Monitor V_B (mV)	Detector Voltage V_d (V)	Detector Current I_d (μA)	Detector Resistance R_d (Ω)
1783	362	0.28837	1432.460	29.3
1650	352	0.28474	1308.468	27.7
1501	341	0.28090	1169.355	27.3
1229	321	0.27395	915.323	30.0
1018	305	0.26806	718.750	20.7
959	301	0.26691	663.306	36.3
319	249	0.24537	70.565	38.8
295	247	0.24451	48.387	53.0
253	243	0.24248	10.081	47.8
121	231	0.23670	-110.887	49.6
2	220	0.23130	-219.758	47.8
-97	211	0.22696	-310.484	54.9
-252	196	0.21921	-451.613	67.6
-504	169	0.20387	-678.427	86.4
-750	139	0.18506	-896.169	133.7
-998	100	0.15689	-1106.855	844.0
-1506	-141	-0.07027	-1376.008	12183.3
-2026	-622	-0.54925	-1415.323	24417.9
-2488	-1066	-0.99232	-1433.468	268780.6
-3032	-1608	-1.53422	-1435.484	148417.9
-3484	-2057	-1.98306	-1438.508	14415.3
-4045	-2582	-2.50620	-1474.798	12288.1
-4596	-3092	-3.01407	-1516.129	76828.6
-5224	-3712	-3.63366	-1524.194	9694.3
-6025	-4439	-4.35682	-1598.790	32684.6
-7011	-5396	-5.31232	-1628.024	15222.7
-8208	-6520	-6.43254	-1701.613	18796.6
-9048	-7318	-7.22836	-1743.952	

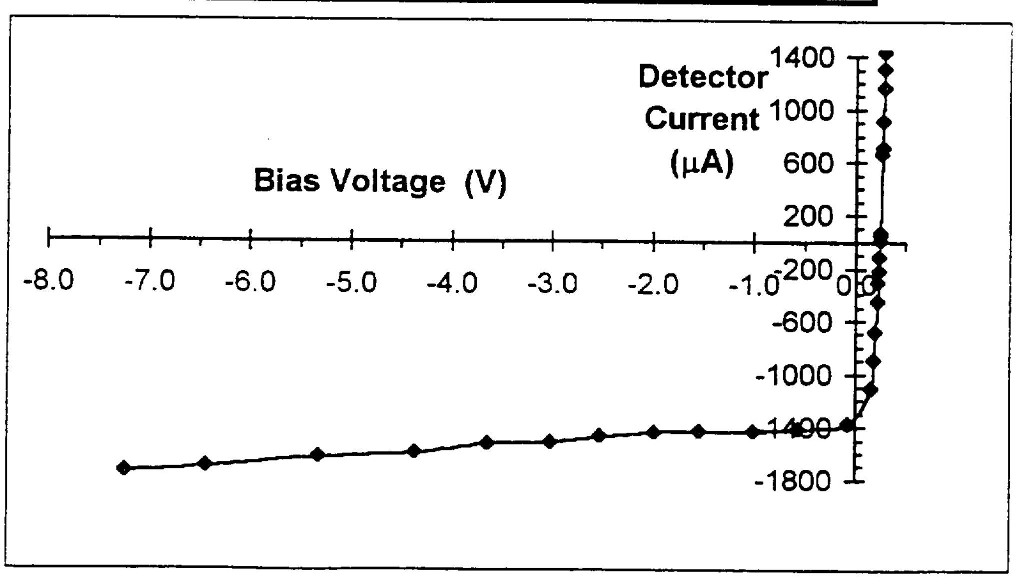

Optical Power=2.0mW

InAs Monitor=835mV

Bias Current Monitor V_{Bi} (mV)	Bias Voltage Monitor V_B (mV)	Detector Voltage V_d (V)	Detector Current I_d (μA)	Detector Resistance R_d (Ω)
1765	361	0.288252	1415.323	19.0
1584	349	0.285009	1244.960	25.9
1501	343	0.282999	1167.339	21.5
1428	338	0.281522	1098.790	27.5
1238	324	0.276642	921.371	25.5
974	305	0.270336	674.395	32.6
449	264	0.254414	186.492	36.8
253	248	0.247741	5.040	38.1
108	236	0.242632	-129.032	41.6
3	227	0.238606	-225.806	37.2
-58	222	0.236508	-282.258	45.6
-204	209	0.230399	-416.331	47.8
-512	181	0.216907	-698.589	63.7
-762	155	0.202514	-924.395	73.7
-1012	127	0.186017	-1148.185	120.3
-1500	55	0.135572	-1567.540	1086.8
-2039	-233	-0.139423	-1820.565	10761.4
-2515	-669	-0.573350	-1860.887	16025.8
-3014	-1139	-1.041848	-1890.121	21125.6
-3528	-1630	-1.531656	-1913.306	47186.7
-4549	-2630	-2.530568	-1934.476	20308.2
-5001	-3061	-2.960480	-1955.645	6478.6
-5964	-3897	-3.789899	-2083.669	9363.1
-7055	-4884	-4.771511	-2188.508	11221.3
-8007	-5759	-5.642521	-2266.129	16402.1
-9027	-6721	-6.601516	-2324.597	

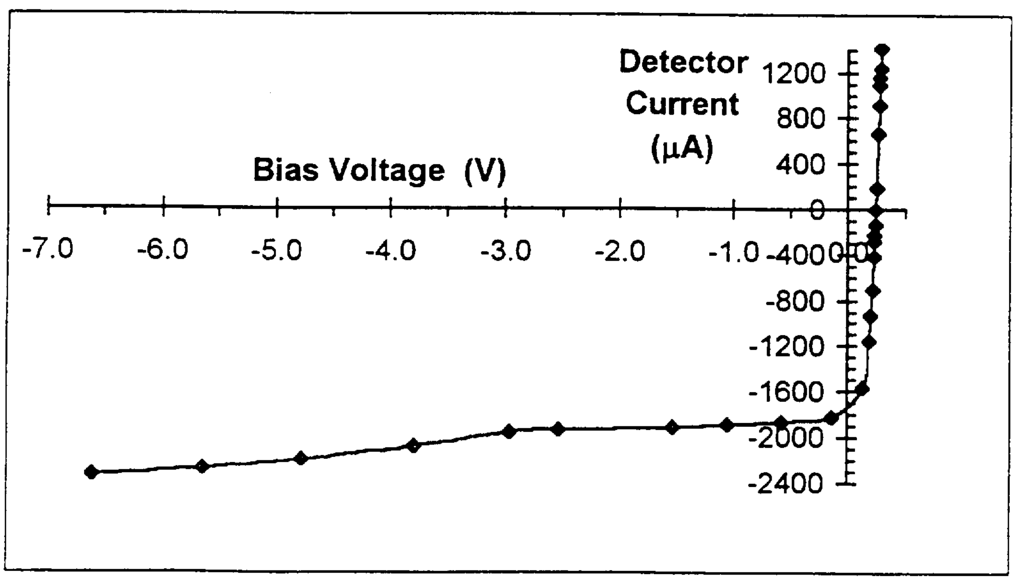

Optical Power=2.5mW

InAs Monitor=1040mV

Bias Current Monitor V_{Bi} (mV)	Bias Voltage Monitor V_B (mV)	Detector Voltage V_d (V)	Detector Current I_d (μA)	Detector Resistance R_d (Ω)
1758	363	0.290719	1406.250	28.3
1516	345	0.284325	1180.444	26.1
1447	340	0.282641	1115.927	21.2
1227	325	0.278263	909.274	26.2
979	307	0.272181	677.419	29.5
369	261	0.255404	108.871	33.6
255	252	0.251845	3.024	33.6
103	240	0.247099	-138.105	34.9
3	232	0.243866	-230.847	32.1
-100	224	0.240788	-326.613	38.2
-257	211	0.235249	-471.774	45.2
-505	189	0.224959	-699.597	49.1
-1005	143	0.202483	-1157.258	76.9
-1529	83	0.166525	-1625.000	148.0
-2001	4	0.107888	-2021.169	1342.4
-2482	-277	-0.162749	-2222.782	7113.0
-3074	-797	-0.679018	-2295.363	13228.6
-3520	-1212	-1.092412	-2326.613	44588.6
-3980	-1662	-1.541894	-2336.694	41460.0
-4537	-2206	-2.085220	-2349.798	16641.6
-5054	-2694	-2.571718	-2379.032	8835.3
-6010	-3554	-3.426744	-2475.806	8197.9
-7072	-4502	-4.368837	-2590.726	8918.4
-8026	-5361	-5.222914	-2686.492	10059.0
-9134	-6370	-6.226785	-2786.290	

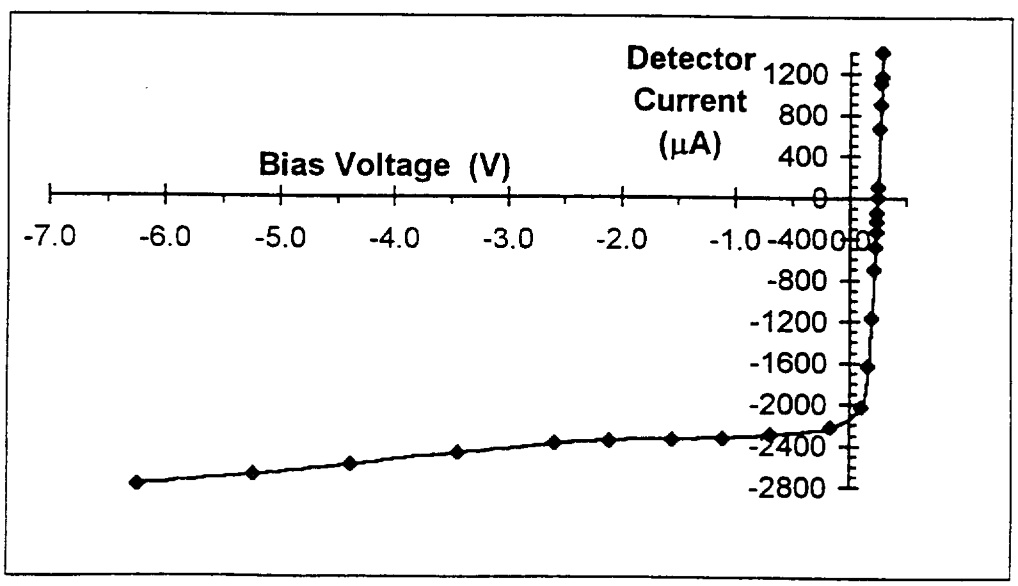

FAMILY OF V-I CURVES

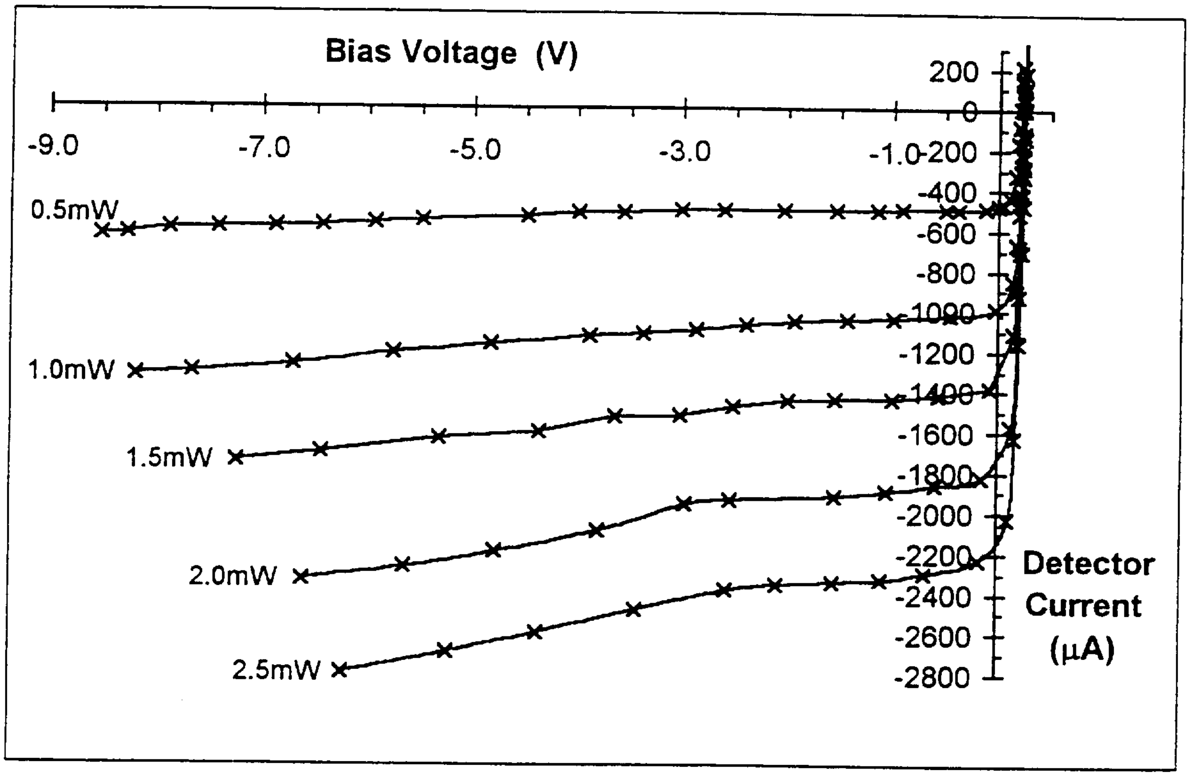

FREQUENCY RESPONSE MEASUREMENTS

VB=0.0
amplifier bias=2.9mV

Frequency (MHz)	Beam #1 (mV)	Beam #2 (mV)	Het. Sig. (RMS mV)	Frequency Response	Detector RC Model	Het. Qum. Efficiency	RC Model MS Error
0					1.00		
20	142.9	42.9	4.56	0.98	0.973556	0.599981	4.48E-05
40	140.2	41.7	3.74	0.83	0.909876	0.425172	0.007173
60	140.8	41.7	3.26	0.72	0.826852	0.321736	0.011887
80	144.2	40.9	2.93	0.64	0.741388	0.257995	0.00972
90	144.6	41.4	2.93	0.64	0.700852	0.253926	0.003987
150	143.2	41.8	2.64	0.57	0.508321	0.206346	0.004428
200	142.6	41.2	2.11	0.46	0.404911	0.134706	0.003548
250	142.5	24.9	1.39	0.40	0.333973	0.101945	0.004913
300	140.5	24.4	1.10	0.33	0.283195	0.06657	0.001877
350	268.6	22	1.01	0.23	0.24537	0.032351	0.000315
400	265.6	20.9	0.96	0.22	0.216232	0.031492	6.97E-05
500	258.1	20.4	0.91	0.22	0.174458	0.030093	0.002032
600	252	19	0.82	0.21	0.146057	0.026827	0.003748
700	285.9	16.8	0.62	0.16	0.125541	0.015994	0.001191
						MS Error	0.002891

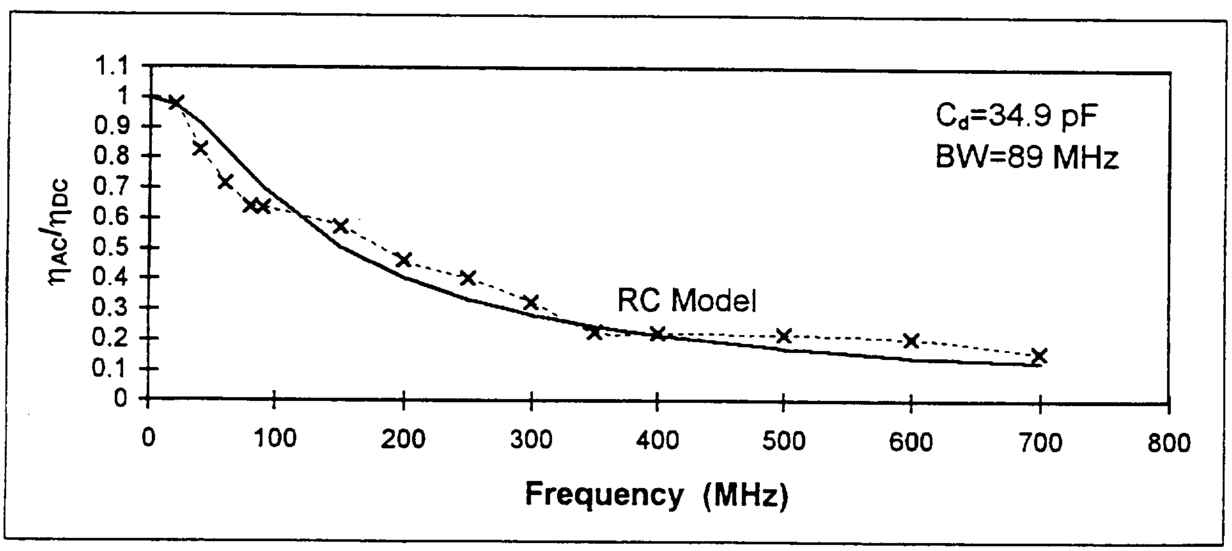

VB=-0.5V
amplifier bias=10.8mV

Frequency (MHz)	Beam #1 (mV)	Beam #2 (mV)	Het. Sig. (RMS mV)	Frequency Response	Detector RC Model	Het. Qum. Efficiency	RC Model MS Error
0					1.00		
20	154.8	37.4	3.84	1.00	0.991394	0.622034	4.5E-05
50	154.8	37.7	4.26	1.10	0.958972	0.757007	0.020194
70	154.8	37.7	4.3	1.11	0.925549	0.77129	0.034547
145	155.4	37.7	3.93	1.01	0.765941	0.641594	0.061372
150	154.8	38	2.62	0.67	0.755133	0.283183	0.006673
180	154.8	38	2.18	0.56	0.69279	0.196055	0.017541
250	153.7	38	2.21	0.57	0.569216	0.203039	1.05E-06
300	154.6	37.8	2.26	0.58	0.499836	0.212564	0.006994
350	153.7	38	1.84	0.47	0.443435	0.140744	0.000982
400	154	37.8	1.72	0.44	0.397301	0.123636	0.002273
450	197.4	29.7	1.78	0.48	0.359174	0.145165	0.015128
500	194	29.8	1.56	0.43	0.327303	0.112971	0.009614
550	235	24.6	1.1	0.32	0.300358	0.063193	0.000316
600	262	24.8	0.76	0.21	0.277334	0.026538	0.005066
650	256	24.8	0.38	0.10	0.257468	0.006797	0.02345
700	278	22.2	0.2	0.06	0.240173	0.002122	0.03308
750	282	22.2	0.17	0.05	0.224995	0.00151	0.03091
800	311	19.5	0.11	0.03	0.211577	0.000749	0.031312
						MS Error	0.016639

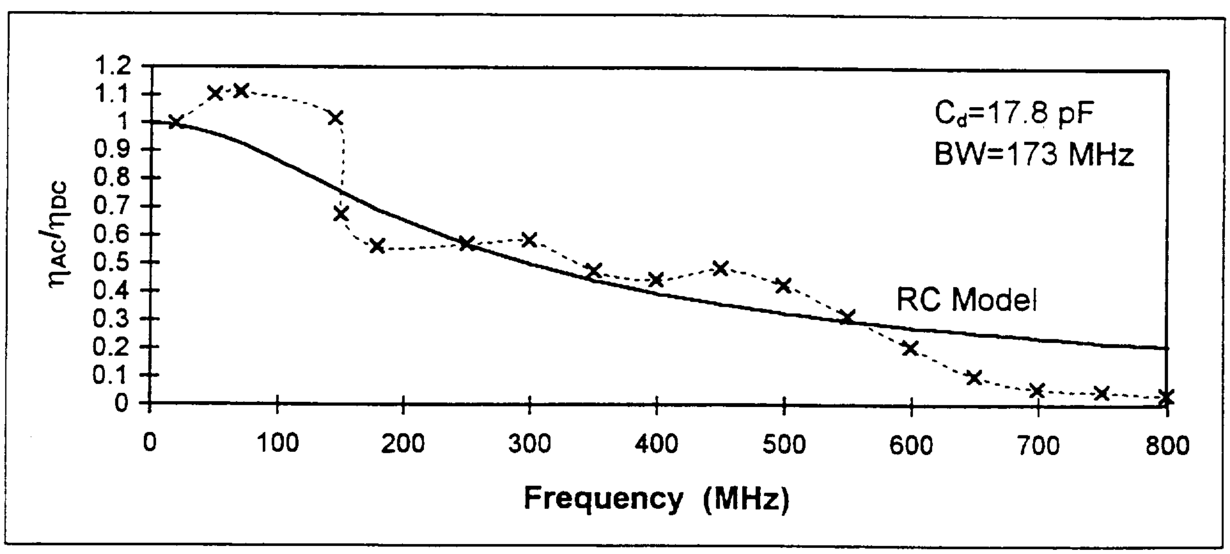

VB=-1.0V

amplifier bias=12.6mV

Frequency (MHz)	Beam #1 (mV)	Beam #2 (mV)	Het. Sig. (RMS mV)	Frequency Response	Detector RC Model	Het. Qum. Efficiency	RC Model MS Error
0					1.00		
20	175.2	50.8	5.25	1.07	0.99646	0.717019	0.005646
50	206	32.6	4.02	1.04	0.988747	0.675089	0.002606
150	208	32.6	4.01	1.03	0.923263	0.66486	0.0118
250	207	32.6	2.78	0.72	0.823765	0.321188	0.011353
300	254	24.4	2.29	0.69	0.771457	0.297473	0.006598
350	253	24.4	2.2	0.66	0.720852	0.275692	0.003178
400	250	24.4	2.1	0.64	0.673246	0.254373	0.001223
450	246	24.6	2.1	0.64	0.62924	0.254421	8.26E-05
650	332	24.7	2.14	0.55	0.489156	0.191471	0.004173
700	330	24.7	1.8	0.47	0.461912	0.136316	2.84E-05
750	326	24.7	1.6	0.42	0.437184	0.109082	0.000369
800	383	22.8	1.3	0.34	0.414693	0.072279	0.005545
886	384	24.3	1.18	0.29	0.380535	0.051776	0.00857
985	353	24.3	1.12	0.29	0.347112	0.050893	0.003797
1000	354	24.3	1.17	0.30	0.342518	0.055376	0.002
1050	355	24.3	1.17	0.30	0.327994	0.055214	0.000938
1100	359	24.3	1.33	0.34	0.314583	0.070524	0.000462
1150	356	24.3	1.17	0.30	0.302169	0.055053	2.74E-05
1200	355	24.3	1.3	0.33	0.290652	0.068165	0.00158
1400	161	35	1.07	0.30	0.25192	0.055652	0.002174
1500	165	35	0.96	0.26	0.236064	0.043622	0.000798
1550	164	35	1.07	0.30	0.228839	0.054549	0.004453
1600	165	35	0.9	0.25	0.222031	0.03834	0.000664
1700	166	34.8	0.91	0.25	0.20953	0.039292	0.001708
1750	52	69	0.82	0.28	0.203779	0.048893	0.005784
1850	125	79.6	1.6	0.30	0.193154	0.054928	0.0107
1900	43.8	80.5	0.71	0.25	0.188237	0.038449	0.003589
						MS Error	0.00197

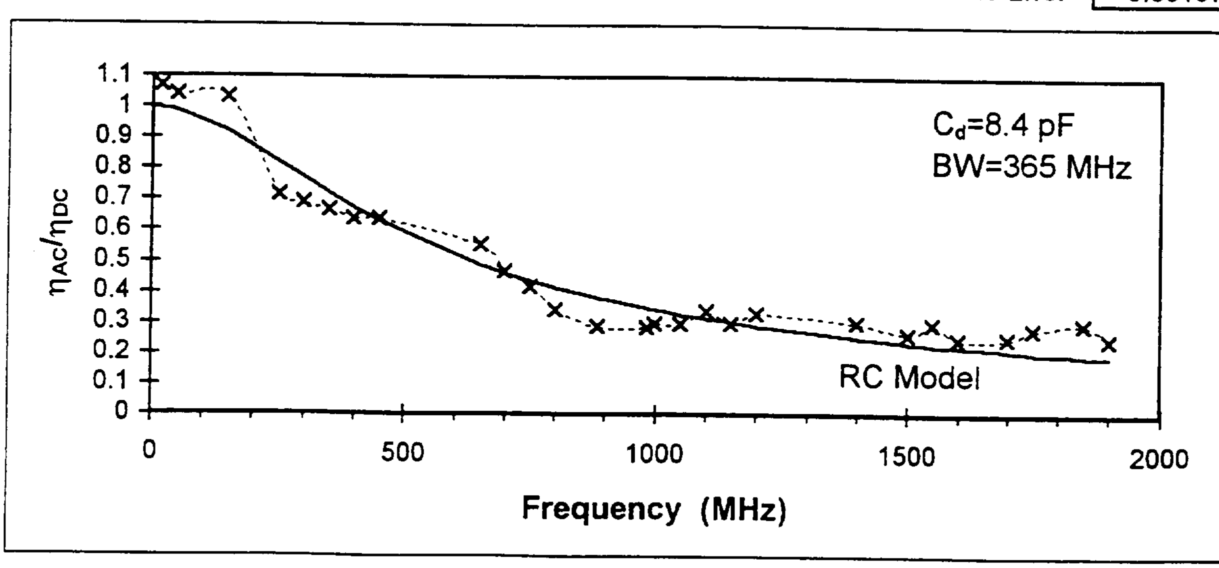

VB=-3.0V

amplifier bias=7.9mV

Frequency (MHz)	Beam #1 (mV)	Beam #2 (mV)	Het. Sig. (RMS mV)	Frequency Response	Detector RC Model	Het. Qum. Efficiency	RC Model MS Error
0					1		
20	72.2	32.2	2.47	1.01	0.99868	0.63698	4.26E-05
200	71	32.8	2.47	1.00	0.893299	0.633453	0.011907
250	71	32.8	1.98	0.80	0.846514	0.40541	0.001987
300	71	32.8	1.63	0.66	0.798216	0.27722	0.018246
400	53	65.7	1.86	0.59	0.704922	0.216972	0.013984
700	27.2	116.2	1.63	0.57	0.493785	0.208385	0.006587
800	27.2	116.2	1.29	0.45	0.444937	0.130283	9.35E-05
900	15.7	116.2	0.76	0.42	0.403953	0.111546	0.000279
1100	15.5	116.2	0.72	0.40	0.339739	0.103319	0.004238
1400	52.2	50.4	0.80	0.30	0.272941	0.055178	0.000525
						MS Error	0.005789

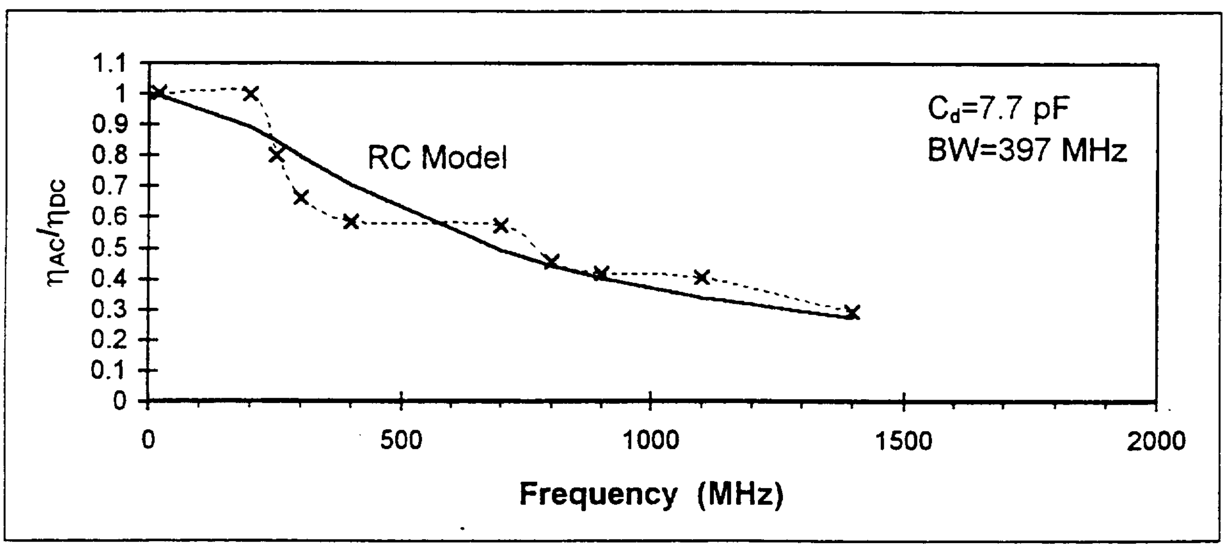

VB=-4.0V
amplifier bias=8.0mV

Frequency (MHz)	Beam #1 (mV)	Beam #2 (mV)	Het. Sig. (RMS mV)	Frequency Response	Detector RC Model	Het. Qum. Efficiency
0					1	
20	70.7	33.6	2.48	1.00	0.998867	0.66079
50	70.7	34.2	2.28	0.90	0.993274	0.545718
100	70.7	34.9	2.36	0.92	0.974039	0.569471
250	70.7	34	2.12	0.84	0.864829	0.475443
250	56	52.4	2.28	0.79	0.864829	0.420643
300	56	52.4	2.04	0.71	0.820532	0.336747
400	56	52.4	1.76	0.61	0.732705	0.250651
700	40.4	85.8	1.80	0.58	0.523952	0.22166
800	23.5	109.8	1.20	0.49	0.473933	0.15738
900	23.2	109.8	1.08	0.44	0.43154	0.129994
1000	23	109.1	1.08	0.45	0.395414	0.13264
1100	33.2	101.50	1.28	0.42	0.364413	0.119916
1450	45.9	40.00	0.84	0.39	0.284472	0.100331

RC Model MS Error
9.52E-06
0.007804
0.002462
0.000407
0.004947
0.012028
0.01426
0.002786
0.000145
0.000103
0.002573
0.003574
0.010722

MS Error 0.004755

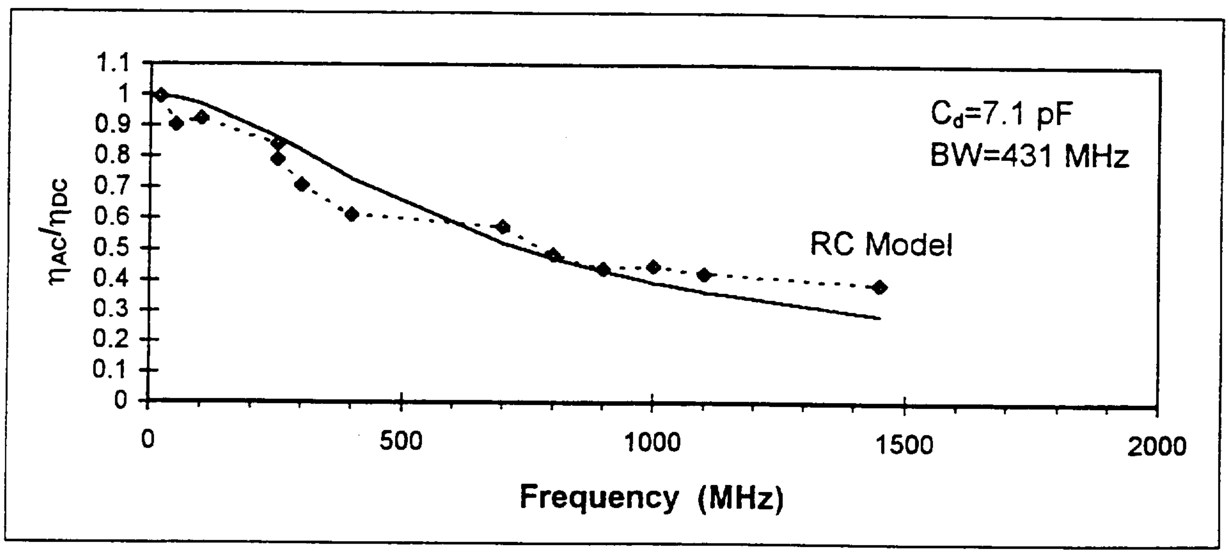

VB=-5.0V

amplifier bias=7.6mV

Frequency (MHz)	Beam #1 (mV)	Beam #2 (mV)	Het. Sig. (RMS mV)	Frequency Response	Detector RC Model	Het. Qum. Efficiency
0					1	
10	69	37.4	2.774	1.04	0.997739	
20	69.0	37.4	2.622	0.99	0.997105	0.712134
100	67.9	37.2	2.432	0.93	0.977435	0.628057
200	68.3	37.7	2.318	0.87	0.922732	0.557382
300	68.3	37.7	1.9	0.72	0.848959	0.374484
400	68.3	37.7	1.634	0.61	0.770211	0.276968
600	68.3	37.7	1.596	0.60	0.627704	0.264236
700	29.7	104.2	1.444	0.50	0.56868	0.185117
800	29.7	104.2	1.444	0.50	0.517657	0.185117
950	29.5	104.1	1.33	0.47	0.454003	0.15864
1200	29.5	104.1	1.444	0.51	0.374075	0.187001
1400	72.8	36	1.33	0.50	0.326708	0.181058
1500	72.8	36	1.064	0.40	0.307015	0.115877
1600	72.8	36	0.836	0.31	0.289449	0.071537

RC Model MS Error
0.00207
0.000122
0.002642
0.002536
0.017929
0.024106
0.000732
0.004347
0.000222
0.00013
0.01722
0.029069
0.008235
0.000533
MS Error 0.006343

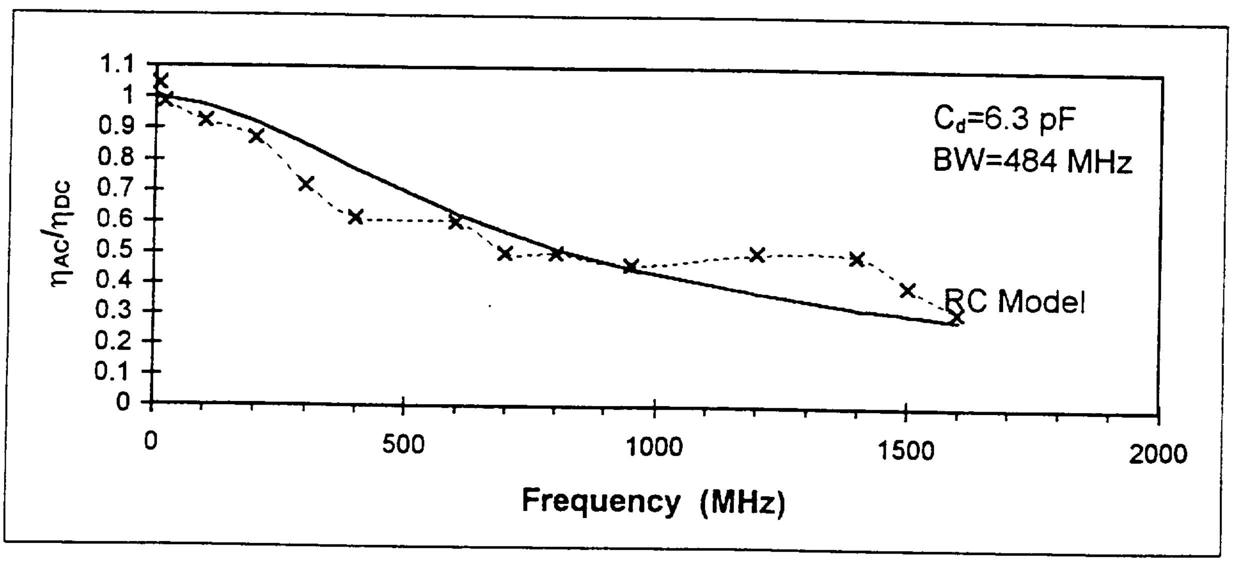

VB=-6.0V

amplifier bias=8.2mV

Frequency (MHz)	Beam #1 (mV)	Beam #2 (mV)	Het. Sig. (RMS mV)	Frequency Response	Detector RC Model	Het. Qum. Efficiency
0					1	
20	78.8	21.4	2.05	1.08	0.997279	0.877408
100	78.6	21.4	1.86	0.98	0.981572	0.7245
180	79	21.2	1.60	0.85	0.947627	0.537421
300	79	21.2	1.52	0.81	0.874294	0.487457
400	49.3	66.7	2.09	0.69	0.804568	0.352793
450	49.3	66.7	2.09	0.69	0.769582	0.352793
700	49.2	66.7	1.98	0.65	0.613078	0.316126
800	26.5	119	1.63	0.58	0.561839	0.255705
1000	27.2	118.2	1.41	0.49	0.477475	0.183675
1100	49	52.4	1.22	0.46	0.44292	0.159225
1500	78.3	36.2	1.14	0.41	0.340531	0.128576
1600	77.8	36.6	1.10	0.40	0.321478	0.119306
1700	77.8	36.6	0.91	0.33	0.304331	0.081712

	RC Model MS Error
	0.007063
	1.04E-06
	0.010273
	0.004668
	0.014137
	0.007042
	0.001295
	0.00048
	0.000298
	0.000314
	0.005388
	0.005969
	0.000658
MS Error	0.004799

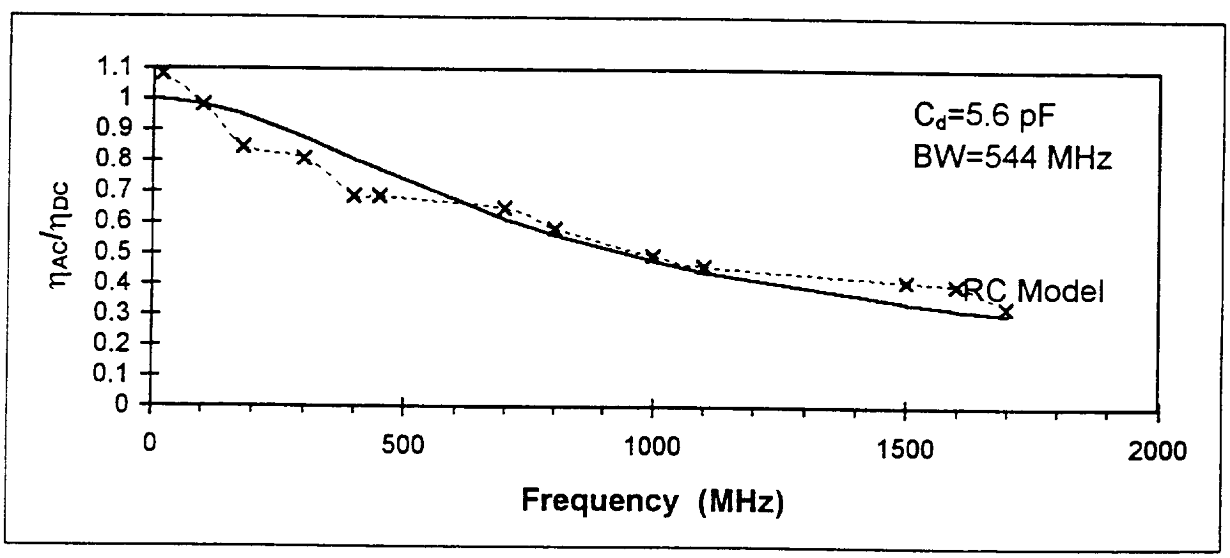

VB=-9.0V

amplifier bias=11.0mV

Frequency (MHz)	Beam #1 (mV)	Beam #2 (mV)	Het. Sig. (RMS mV)	Frequency Response	Detector RC Model	Het. Qum. Efficiency	RC Model MS Error
0					1		
10	78.2	51.4	3.72	1.15	0.998764	0.88092	0.022795
20	78	51.0	3.50	1.09	0.998477	0.786459	0.007722
50	77.7	51	3.19	0.99	0.996472	0.658579	5.56E-06
100	77.7	51	3.23	1.01	0.989411	0.674353	0.000274
250	78	50.6	3.04	0.95	0.943851	0.600682	3.09E-05
300	78.3	50.6	2.66	0.83	0.922364	0.457847	0.008739
450	77.8	50.6	2.36	0.74	0.84761	0.361865	0.012258
700	53.1	79.3	2.36	0.71	0.716975	0.332901	0.000104
750	53.1	79.3	2.36	0.71	0.692555	0.332901	0.000203
800	32.4	124.2	2.05	0.67	0.669021	0.299752	2.74E-06
1000	46.6	118.60	2.09	0.54	0.584423	0.196652	0.001697
1100	47.2	118.60	2.05	0.53	0.547777	0.186424	0.000356
1200	46.6	118.60	2.13	0.55	0.514598	0.203868	0.001483
1500	86.4	27.6	0.99	0.45	0.432738	0.134494	0.000273
1700	88.2	27.8	1.06	0.48	0.389914	0.15053	0.007286
						MS Error	0.004516

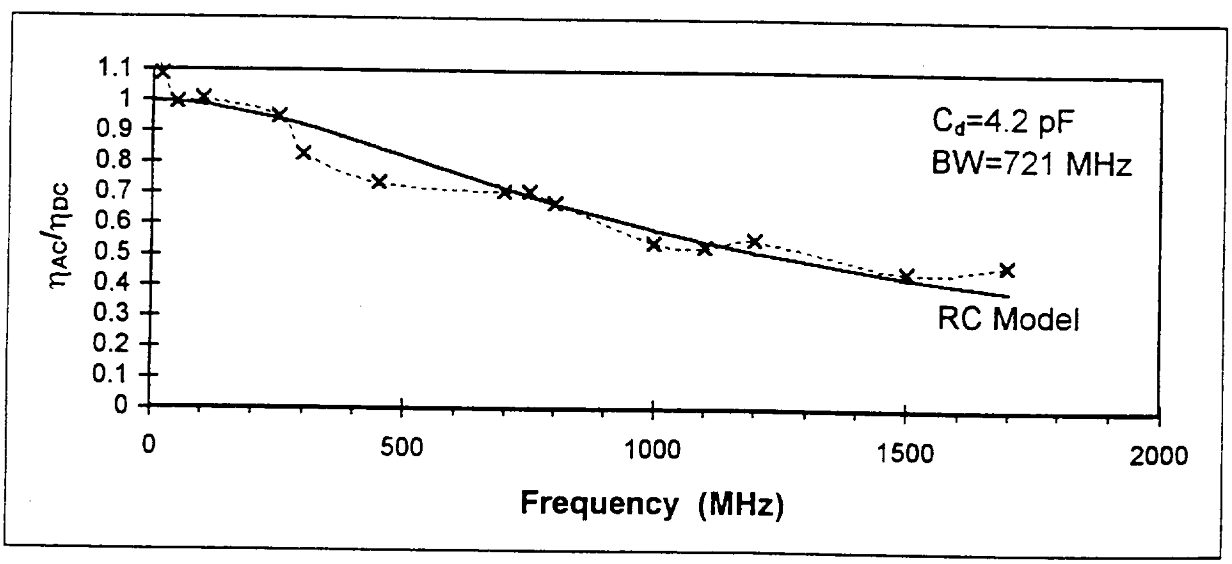

Detector Capacitance

V_B (V)	C_d (pF)
0.0	34.9
0.5	17.8
1.0	8.4
3.0	7.7
4.0	7.1
5.0	6.3
6.0	5.6
9.0	4.2

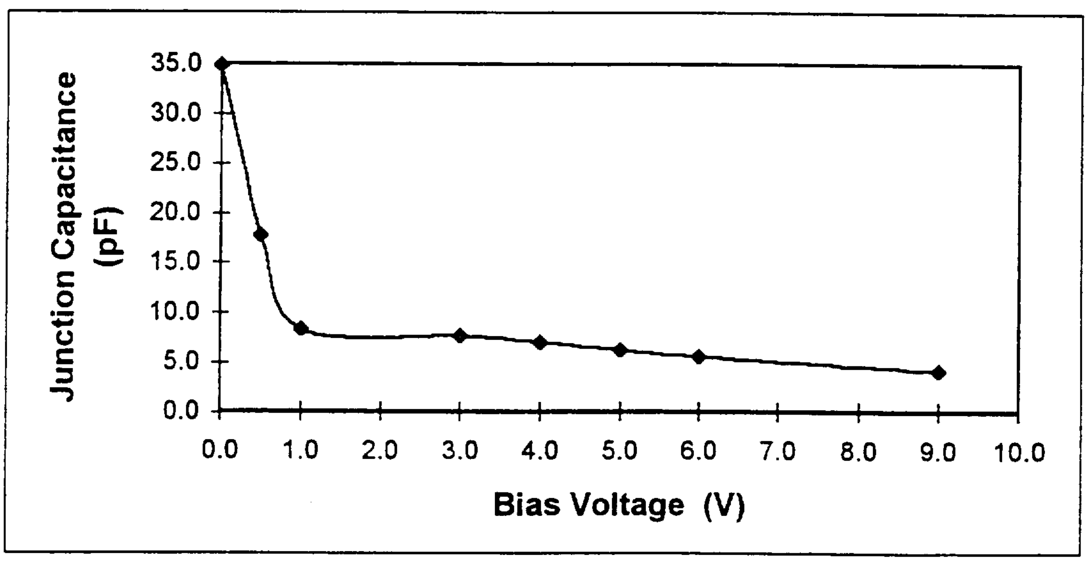

3.0 LIDAR OPTICAL SUBSYSETM PERFORMANCE MODELING AND ANALYSIS

3.1 SYSTEM MODELING

The lidar optical subsystem has been modeled which includes Primary mirror, secondary mirror, quarter wave plate, recollimating lens, beam splitter, beam derotator, and lag angle compensator. Figure 1 is the perspective view of the entire telescope optics. The analysis covers wavefront error, boresight, and polarization. Because of non-traditional design concept, the performance analysis has to address some special issues, such as the effect of the quarter wave plate and the off-axial related performance changes.

3.1.1 System Layout

Three-element Catadooptric off-axial Galilean telescope has been designed to eliminate the central obscuration, reduce the back scattering, and lower the parametric sensitivities. The telescope has no real focus to prevent air breakdown. The mirrors and lens are general conical surface operated at off-axis. One quarter wave plate is located in the front of the lens to converting circular polarized beam to linear polarized beam. A beam splitter is follows the telescope to reflect the output beam into the telescope and transmit the input beam to the monolithic beam derotator. The pupil relay has been omitted to simplify the system structure. The beam derotator remove both angular and linear displacements caused by scanner and telescope. A single electro-mechanical controlled folding mirror has been used to perform lag angle compensation.

The primary mirror, secondary mirror, and recollimating lens share the total power to lower the parametric sensitivity. The conical constants of the secondary mirror and two lens surfaces are also optimized to achieve the overall optical performance.

3.1.2 The effect of the quarter wave plate

The quarter wave plate is located in the convergent ray path. Any parallel plate in the non-collimated ray path will introduce aberrations. In the design, a fused silica plate has been added in to model the effect. The telescope optics has to be reoptimized to obtain acceptable performance. The surface shape of the mirrors as well as lens have changed slightly after introducing the quarter wave plate. The location of the mirrors and lens stay same.

The sensitivity analysis shows the location of the quarter wave plate is not sensitive to the performance. The thickness and wedge errors of the plate are sensitive. The tilt of the element has little effect on the performance.

3.2 Performance

The system specifications are as follows:

Magnification	25	X	(afocal)
Entrance aperture	250	mm	(diameter)
Exit pupil	10	mm	(diameter)
Over axial length	200	mm	
Off-axial value	187.5	mm	
Wavelength	2.067	micron	
Field of view	0.0802	degree	(conical scan angle)

The performance analysis as well as sensitivity analysis have not included the scanner. The conical scan field of view has been considered in the modeling and analysis.

3.2.1 Wavefront performance

Wavefront error has been used to quantitatively describe the beam quality of the telescope. The RMS wavefront error of less 1/10 wave is required by the coherent operation. The well optimized design has achieved much lower wavefront errors. This leaves enough margin for the tolerance of the fabrication and integration.

3.2.1.1 Off-axis effect

Because of the off-axial operation of the telescope, the field characteristics of the performance is not symmetric. Performance can not be simply checked by on-axis and full field as those in the traditional rotation symmetrical system. However, The field character is Plano symmetrical. We check the performances at the (1) center of the field, (2) top most field, (3) low most field, and (4) right most field. Left most field is mirror symmetrical to the right most field.

3.2.1.1Wave front for the emitting beam and returning beam at different field angles

Figures 2 to 5 are plots of the wave front maps at different field angles. The RMS wave front error are:

0.0017	wave	(At the top most field shown in Figure 2)
0.0020	wave	(At the low most field shown in Figure 3)
0.0043	wave	(At the right most field shown in Figure 4)

The peak-to-valley errors are also well below required.

3.2.2 Boresight

Boresight is the other most important performance of the optical system for the coherent operation. An error of 1 micro-radians is required in the object space.

3.2.2.1 Distortion problem

Distortion of the off-axial optics is not axial symmetrical anymore. The beam with conical scan motion will have slight ray angle changes at different scanning clock angle caused by the non-symmentrical distortion. It will be a nightmare to correct this kind of error. The distortion check has to be performed to ensure the ray angle uncertainty is within the boresight requirement.

3.2.2.2 Boresight at different beam angle

The boresight error at different scanning positions are listed:

0.365	micro-radians	(At top most of the field)
0.365	micro-radians	(At low most of the field)
0.271	micro-radians	(At right most of the field)

Boresight error introduced by other parts, such as beam derotator and lag angle compensator is controlled by the tolerance of these parts.

3.2.2.3 Beam position shift on the detector

Beam shift caused by telescope distortion has been checked:

0.0166 mm (At top most of the field)
0.0173 mm (At low most of the field)
0.0119 mm (At right most of the field)

These are negligible.

3.2.3 Polarization

One common question to the off-axial telescope is the polarization. The high steep angle of incidence on the mirrors will introduce polarization changes. The polarization performance has been checked for the telescope.

3.2.3.1 Mirror coating

The effective measure to concur the polarization problem is the suitable coating of the optics. The gold coating has been selected for the primary and secondary mirrors. Because of the very high reflectivity of the gold coating in the operation wavelength. The change in two components of the polarization must be within few percent because the total reflectivity is the average of the two polarization components.

3.2.3.2 Polarization analysis of the telescope

Figure 5 is the polarization map onto the field for the telescope mirrors. Figure 6 is the polarization map onto the entrance pupil for the telescope mirrors. The polarization ray trace shows the polarized throughputs for the mirror pair are:

Total	S-component	P-component
0.983	0.702	0.674

Table 1 is the polarization ray trace through the mirror pair.

Figure 7 is the polarization map onto the field for the complete telescope (mirror pairs, quarter wave plate and recollimating lens). Figure 8 is the polarization map onto the entrance pupil for the complete telescope. The polarized throughputs for the complete telescope are:

Total	S-conponent	P-component
0.366	0.423	0.433

Table 2 is the polarization ray trace trough the complete telescope. The low efficience is caused by no coating has been considered on the quarter wave plate and recollimating lens at this time.

Table 1. Ploarization ray trace through telescope mirrors

pray 2 0 0 0 surf

SURF. NO.			MAGN.	X	Y	Z	PHASE
INCID.	S	1	.707107E+00	.000000E+00	.707107E+00	.000000E+00	.000000E+00
INCID.	P	1	.707107E+00	.707107E+00	.000000E+00	.000000E+00	.900000E+02
REFR.	S	1	.707107E+00	.000000E+00	.707107E+00	.000000E+00	.000000E+00
REFR.	P	1	.707107E+00	.707107E+00	.000000E+00	.000000E+00	.900000E+02
INCID.	S	2	.707107E+00	.707107E+00	.000000E+00	.000000E+00	.900000E+02
INCID.	P	2	.707107E+00	.000000E+00	-.707107E+00	.000000E+00	.180000E+03
REFL.	S	2	.704396E+00	.704396E+00	.000000E+00	.000000E+00	-.884040E+02
REFL.	P	2	.703837E+00	.000000E+00	.462439E+00	-.530599E+00	.181926E+03
INCID.	S	3	.704396E+00	.704396E+00	.000000E+00	.000000E+00	-.884040E+02
INCID.	P	3	.703837E+00	.000000E+00	.462439E+00	-.530599E+00	-.178074E+03
REFL.	S	3	.701889E+00	.701889E+00	.000000E+00	.000000E+00	-.266922E+03
REFL.	P	3	.700333E+00	.000000E+00	-.674395E+00	-.188832E+00	-.176000E+03

V1: (X,Y,Z),PHASE .701889E+00 .000000E+00 .000000E+00 -.266922E+03
V2: (X,Y,Z),PHASE .000000E+00 -.674395E+00 -.188832E+00 -.176000E+03
INTENSITY: APOD., POLAR., PROD. .100000E+01 .983114E+00 .983114E+00

Table 2. Ploarization ray trace through telescope mirrors, quarter wave plate, and lens
pray 2 0 0 0 surf

SURF. NO.	MAGN.	X	Y	Z	PHASE
INCID. S 1	.707107E+00	.000000E+00	.707107E+00	.000000E+00	.000000E+00
INCID. P 1	.707107E+00	.707107E+00	.000000E+00	.000000E+00	.900000E+02
REFR. S 1	.707107E+00	.000000E+00	.707107E+00	.000000E+00	.000000E+00
REFR. P 1	.707107E+00	.707107E+00	.000000E+00	.000000E+00	.900000E+02
INCID. S 2	.707107E+00	.707107E+00	.000000E+00	.000000E+00	.900000E+02
INCID. P 2	.707107E+00	.000000E+00	-.707107E+00	.000000E+00	.180000E+03
REFL. S 2	.704396E+00	.704396E+00	.000000E+00	.000000E+00	-.884040E+02
REFL. P 2	.703837E+00	.000000E+00	.462439E+00	-.530599E+00	.181926E+03
INCID. S 3	.704396E+00	.704396E+00	.000000E+00	.000000E+00	-.884040E+02
INCID. P 3	.703837E+00	.000000E+00	.462439E+00	-.530599E+00	-.178074E+03
REFL. S 3	.701889E+00	.701889E+00	.000000E+00	.000000E+00	-.266922E+03
REFL. P 3	.700333E+00	.000000E+00	-.674395E+00	-.188832E+00	-.176000E+03
INCID. S 4	.701889E+00	.701889E+00	.000000E+00	.000000E+00	.930783E+02
INCID. P 4	.700333E+00	.000000E+00	-.674395E+00	-.188832E+00	-.176000E+03
REFR. S 4	.689244E+00	.689244E+00	.000000E+00	.000000E+00	.930783E+02
REFR. P 4	.690166E+00	.000000E+00	-.677911E+00	-.129483E+00	-.176000E+03
INCID. S 5	.689244E+00	.689244E+00	.000000E+00	.000000E+00	.930783E+02
INCID. P 5	.690166E+00	.000000E+00	-.677911E+00	-.129483E+00	-.176000E+03
REFR. S 5	.676828E+00	.676828E+00	.000000E+00	.000000E+00	.930783E+02
REFR. P 5	.680148E+00	.000000E+00	-.654957E+00	-.183390E+00	-.176000E+03
INCID. S 6	.676828E+00	.676828E+00	.000000E+00	.000000E+00	.930783E+02
INCID. P 6	.680148E+00	.000000E+00	-.654957E+00	-.183390E+00	-.176000E+03
REFR. S 6	.535197E+00	.535197E+00	.000000E+00	.000000E+00	.930783E+02
REFR. P 6	.542261E+00	.000000E+00	-.536572E+00	-.783381E-01	-.176000E+03
INCID. S 7	.535197E+00	-.535197E+00	.000000E+00	.000000E+00	-.869217E+02
INCID. P 7	.542261E+00	.000000E+00	.536572E+00	.783381E-01	.400035E+01
REFR. S 7	.422707E+00	-.422707E+00	.000000E+00	.000000E+00	-.869217E+02
REFR. P 7	.432827E+00	.000000E+00	.432827E+00	-.586503E-05	.400035E+01

V1: (X,Y,Z),PHASE -.422707E+00 .000000E+00 .000000E+00 -.869217E+02
V2: (X,Y,Z),PHASE .000000E+00 .432827E+00 -.586503E-05 .400035E+01
INTENSITY: APOD., POLAR., PROD. .100000E+01 .366021E+00 .366021E+00

The coating design has not been completed for the rest of the optics.

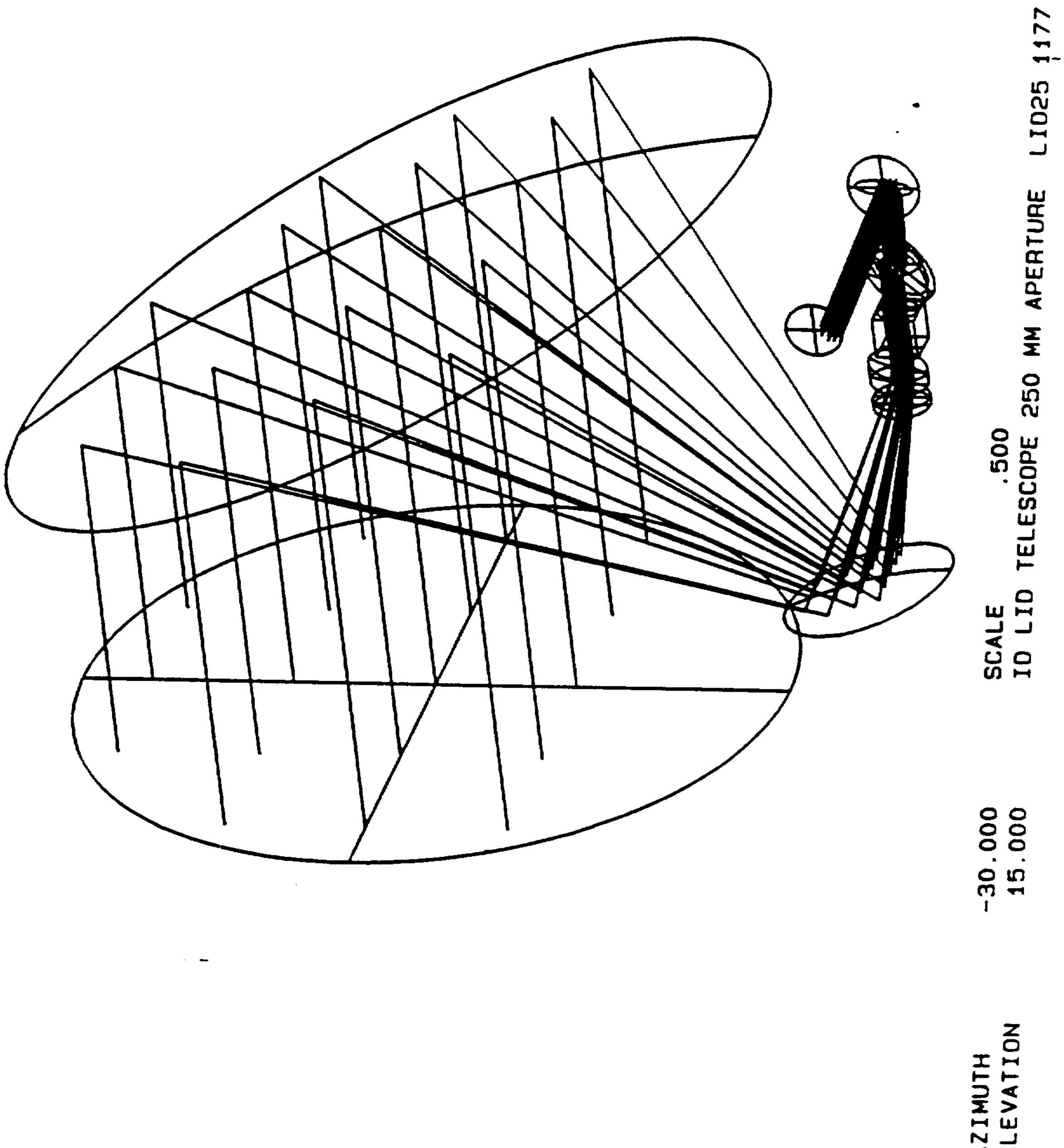

Figure 1. Optical system layout

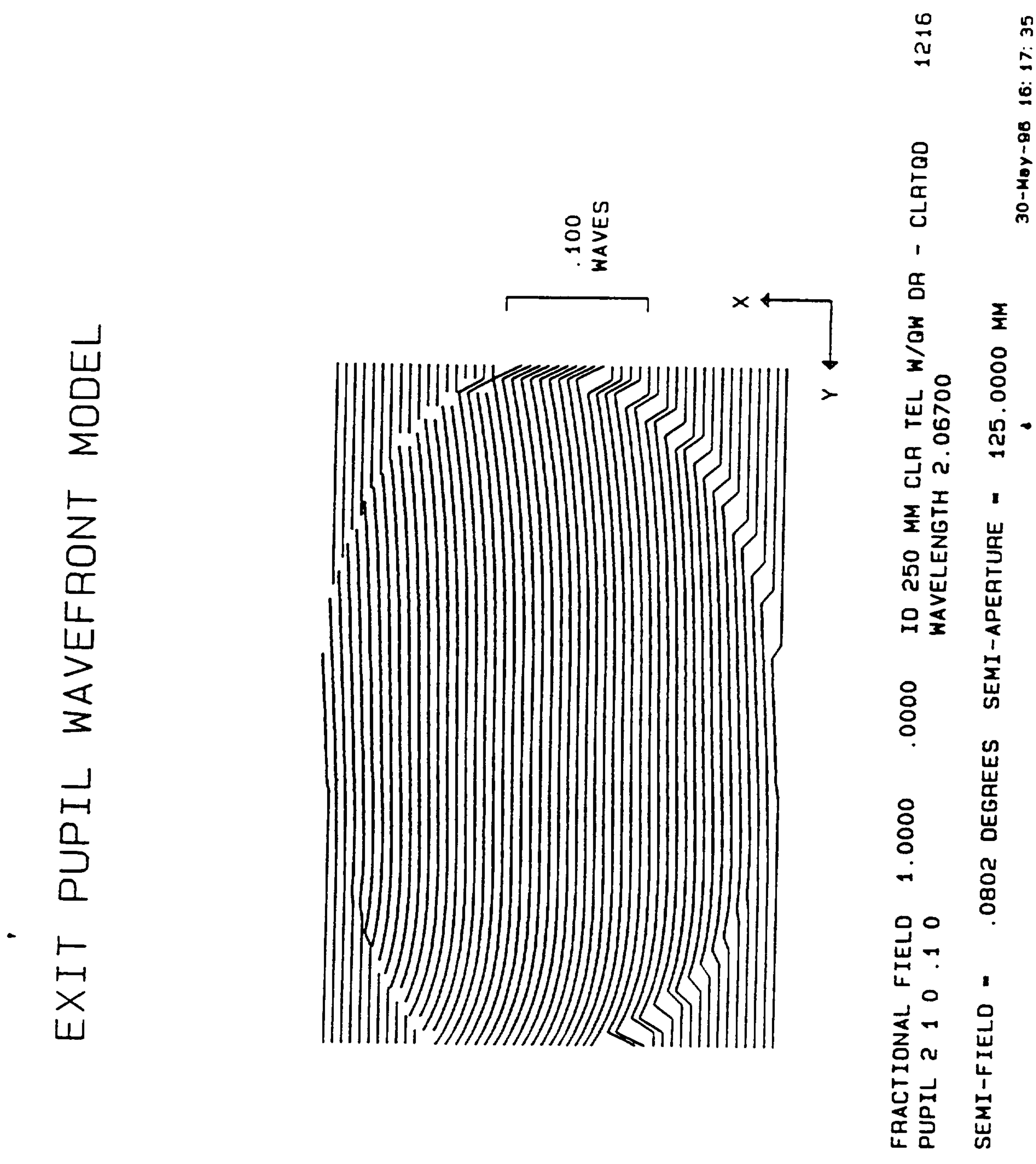

Figure 2. Wavefront error at the top most field

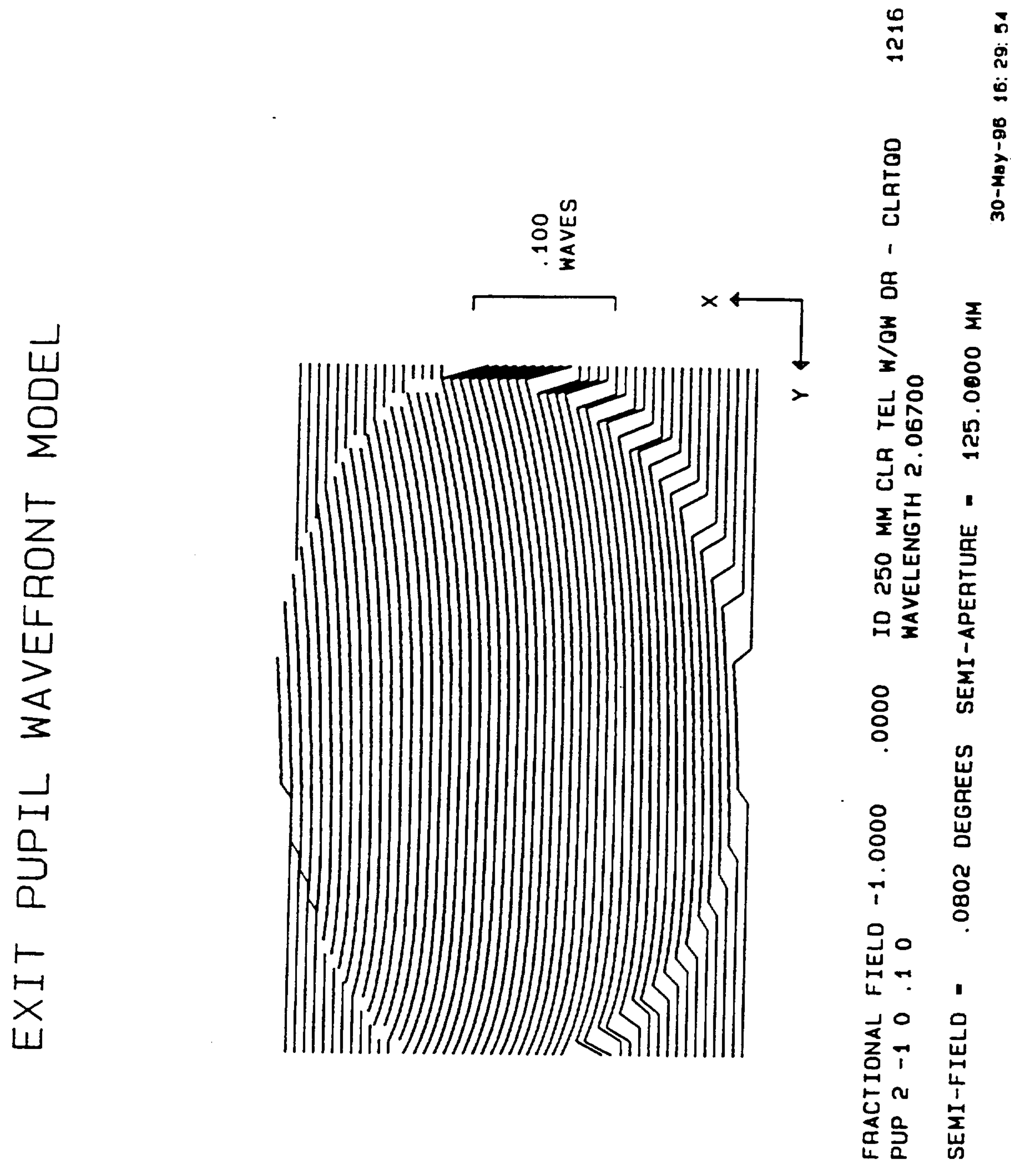

Figure 3. Wavefront error at the low most field

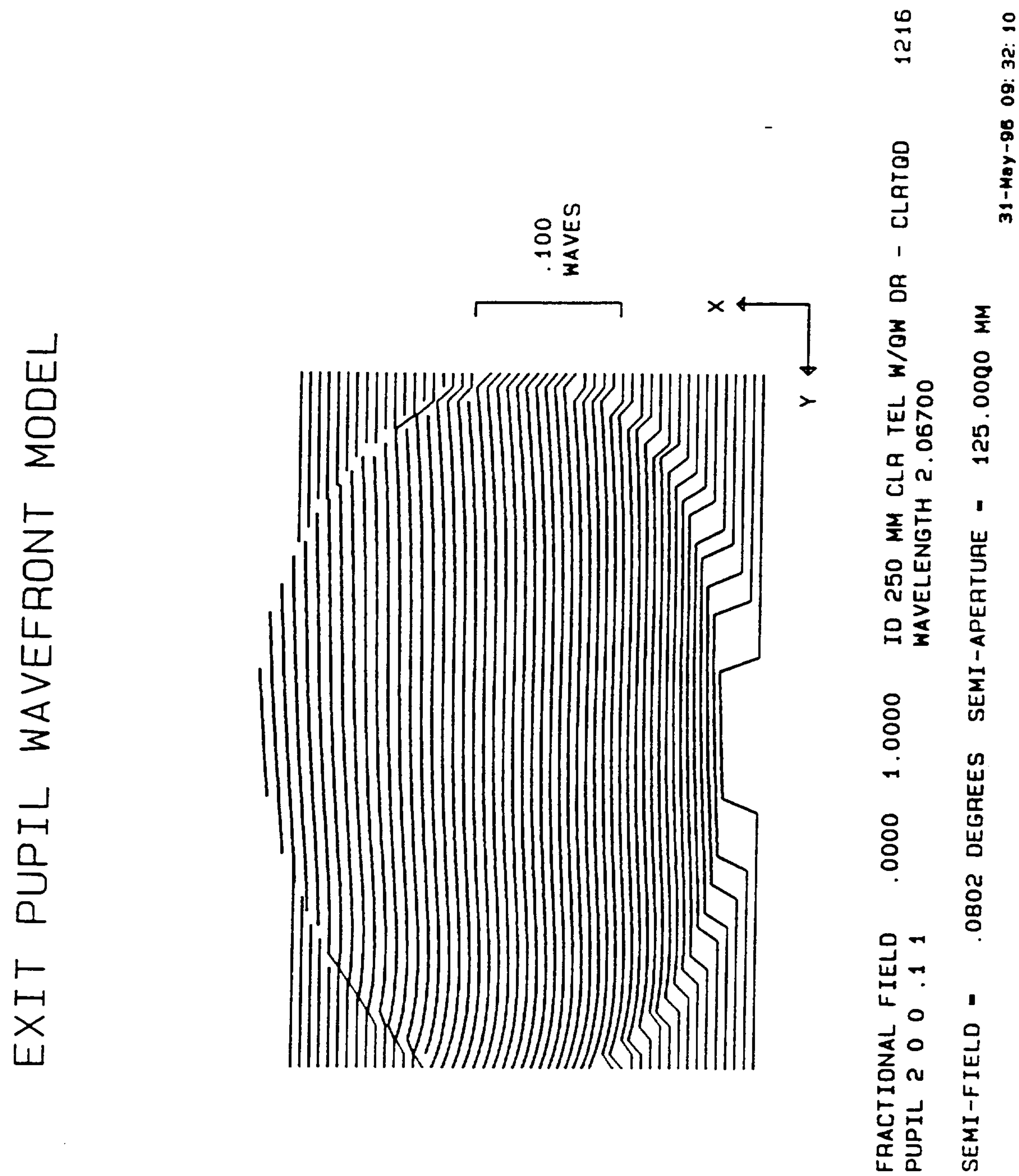

Figure 4. Wavefront error at the right most field

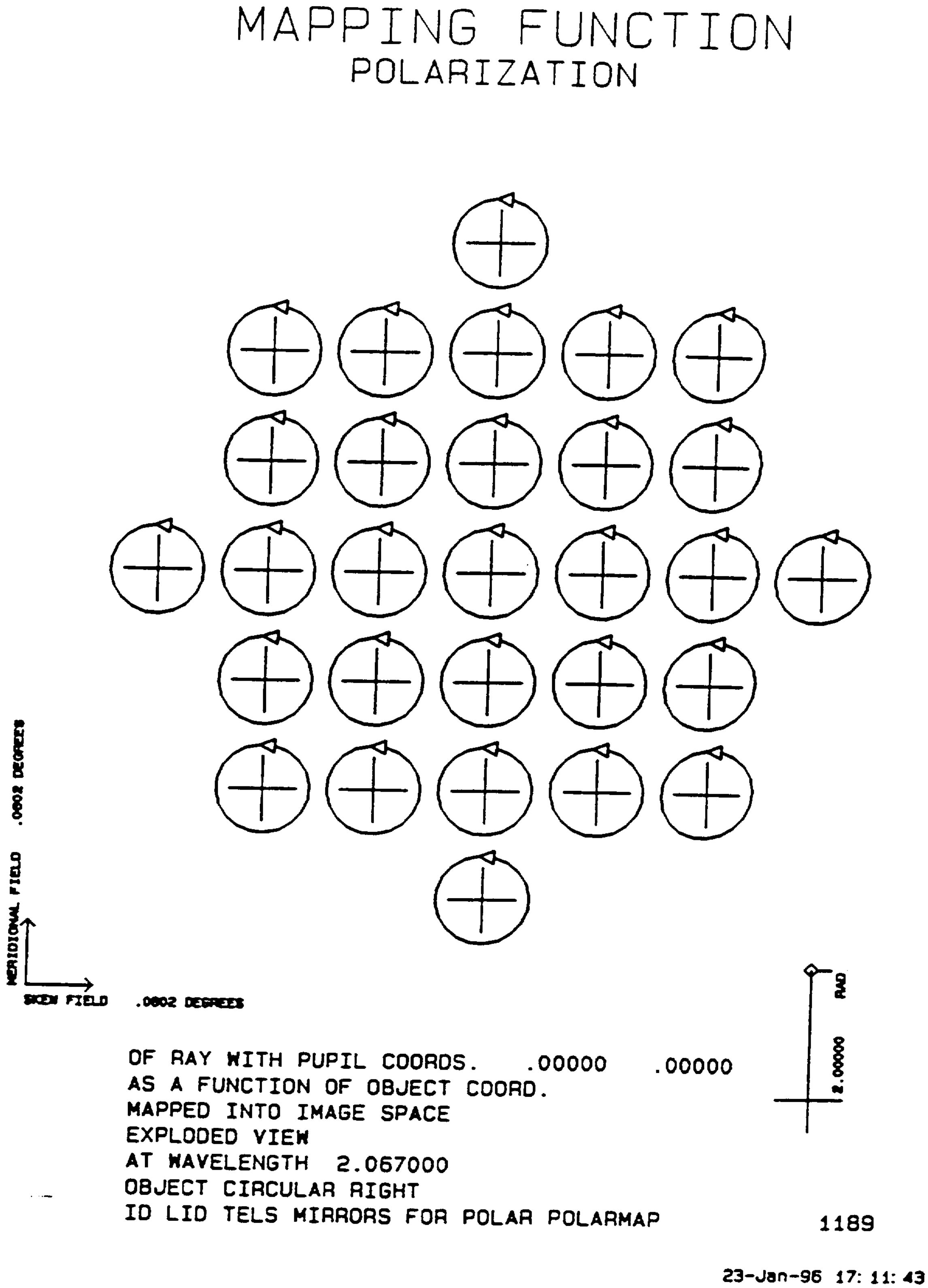

Figure 5. Polarization map over the field for the mirror mair

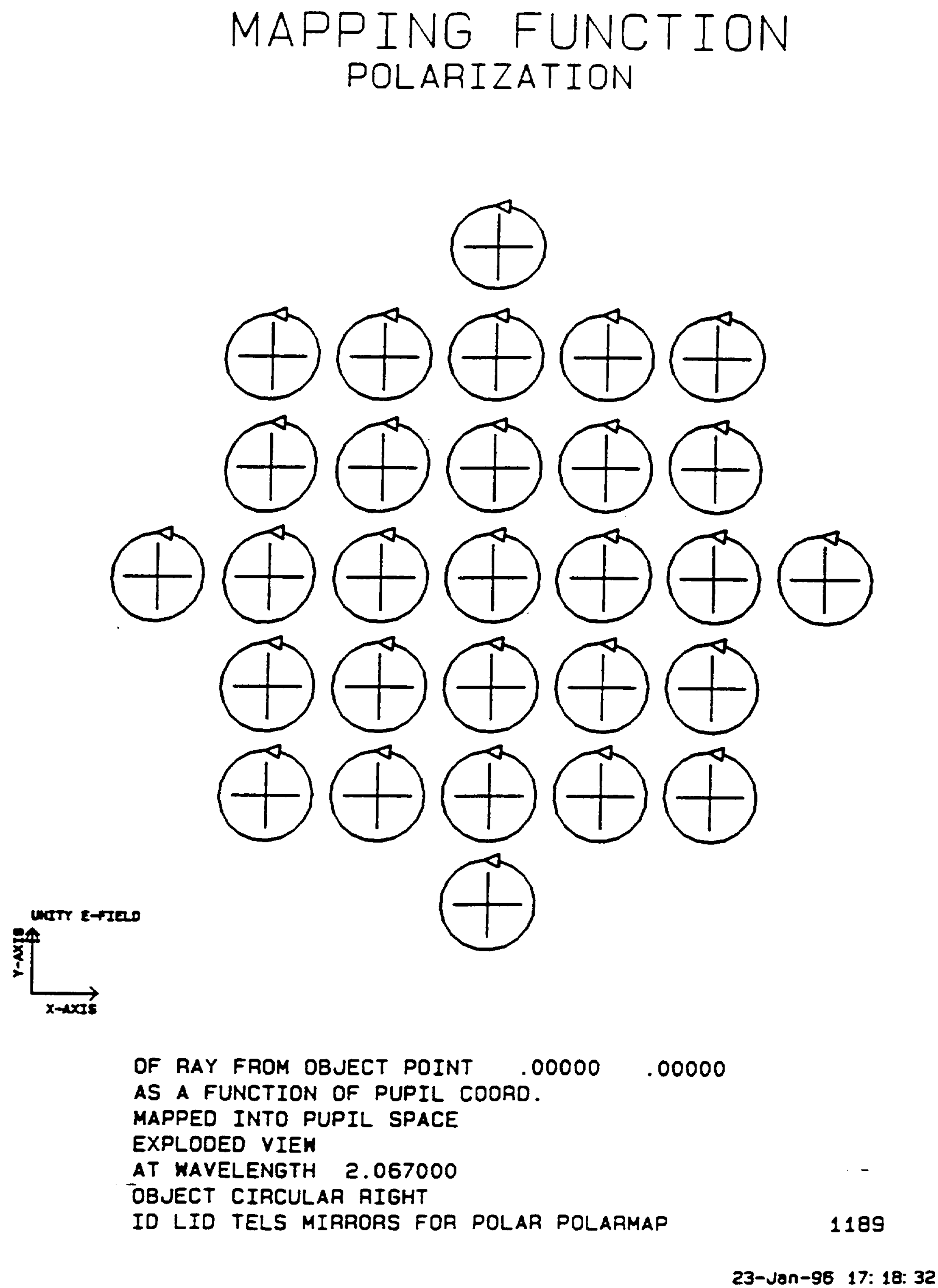

Figure 6. Polarization map over the pupil for the mirror pair

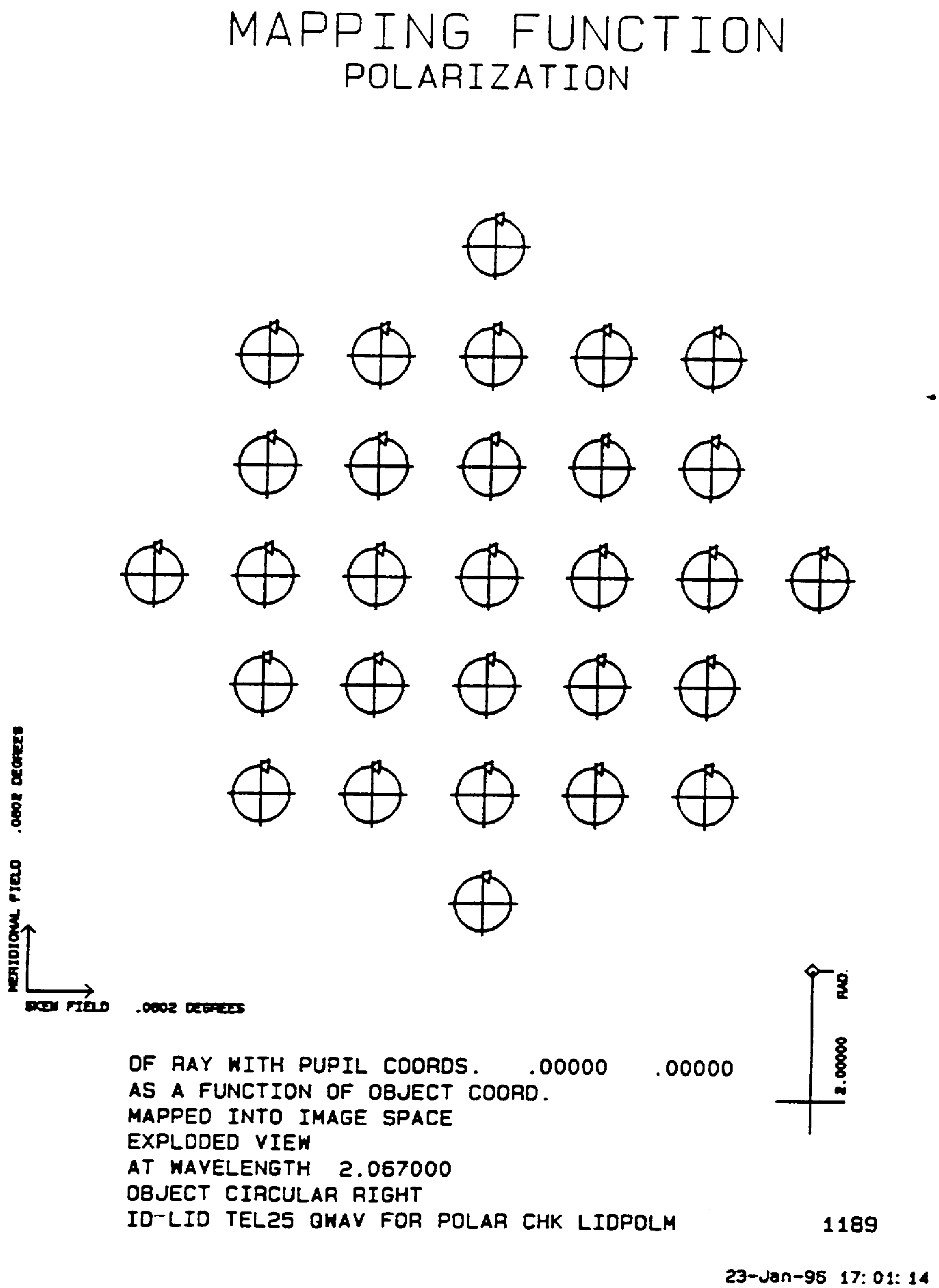

Figure 7. Polarization map over the feld for the complete telescope

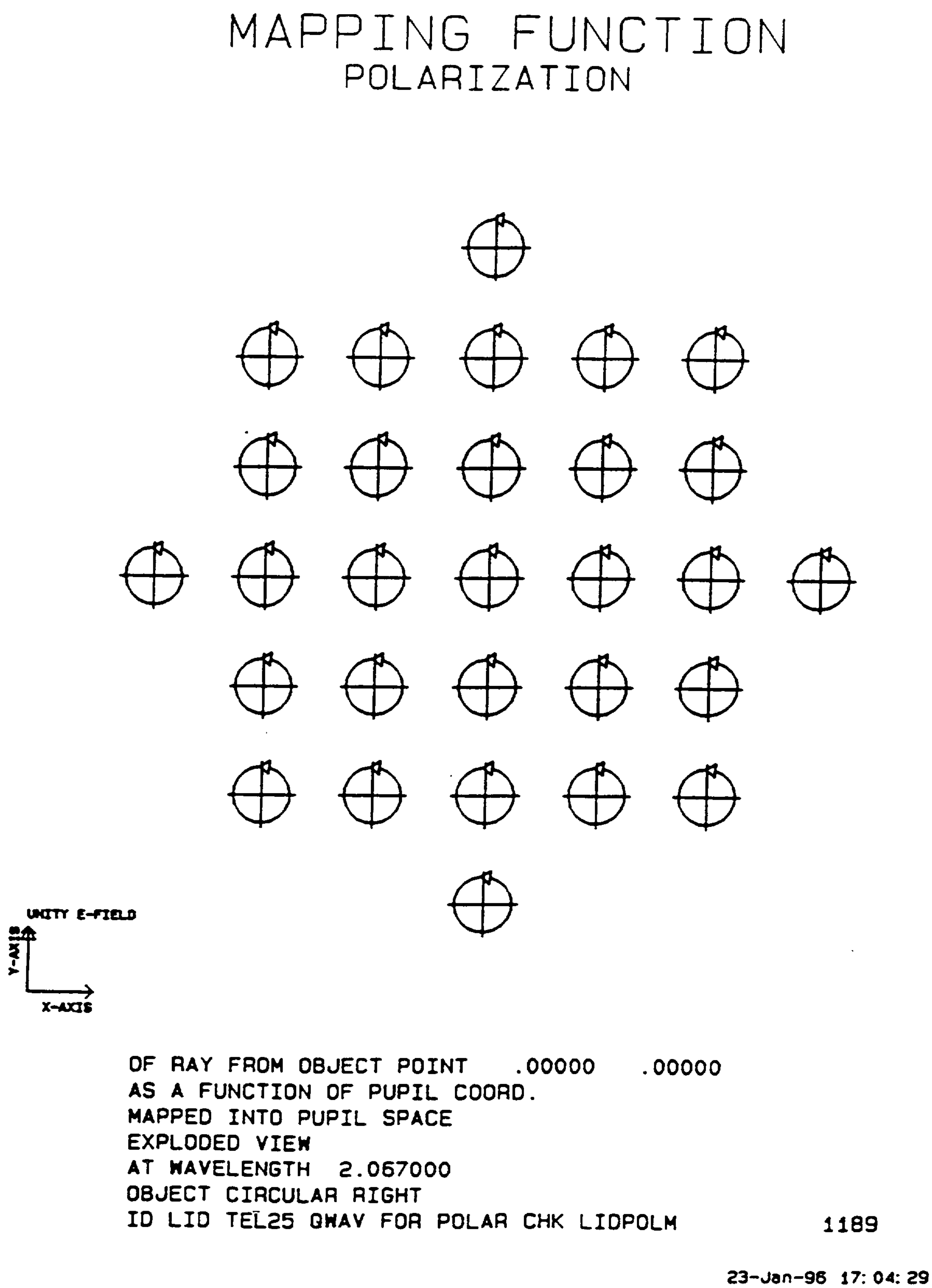

Figure 8. Polarization map over the pupil for the complete telescope

3.3 Sensitivity Analysis

Sensitivities for each part have been checked by varying one parameter at a time in the complete system to evaluation of its effect on the overall performance. The performance degradations are rms wave front error, boresight error, and beam shift on the detector. Wave front errors are in wave at 2.067 micron. Boresight errors are in micro-radians in object space. Beam shift errors are in mm at detector surface. Parametric errors are decenters, tilts, thickness error, and wedge error of each element. Decenter and thickness errors are in mm. Tilt and wedge errors are in milli-radians.

Table 3 lists all the sensitivities with parametric errors and corresponding performance errors. Sensitivities not listed are much looser than 1 mm in length and 1 milli-radians in angle.

3.3.1 Primary and secondary mirrors

Because of non-symmetrical natural of the off-axis telescope, all six parametric errors are independent for each mirror. Linear displacement errors are in order of 0.01 mm to contribute little over 1/10 wave rms wave front errors. Angular errors are in order of 0.017 milli-radians for the primary and 0.17 milli-radians for the secondary to introduce little under than 1/10 wave rms wave front errors. Some numbers are not symmetrical about the sign. The most sensitivities values are listed for these non-symmentric sensitivities. The most sensitive displacement is the axial spacing. 0.01 mm axial position change of the secondary will introduce 0.164 wave rms wave front error. The most sensitive tilt is the tilt around X axis. 0.017 milli-radians change of the primary will introduce 0.054 wave rms wavefront error.

Secondary mirror tilt sensitivities are lower. It is difficult to maintain the angular position for the small secondary mirror.

3.3.2 Quarter wave plate

Quarter wave plate will introduce error because it is located in the convergent ray path. Quarter wave plate is simply a plate with symmetrical shape. Only tilt, thickness, and wedge errors are checked. Thickness error of 0.01 mm will introduce 0.015 wave rms wave front error. 17.5 milli-radians of tilt and 1.7 milli-radians of wedge will introduce 0.019 wave and 0.051 wave rms wave front error respectively. The location of the quarter wave plate shows almost no effect to the performance.

3.3.3 Re-collimating lens

Collimating lens is working at off-axis. All six variations have been checked. Compared to the primary and secondary mirrors, collimating lens has much lower sensitivities. The axial displacement of 0.01 mm will introduce 0.023 wave rms wavefront error. In the real practice, this axial displacement can be used to final tune the wavefront performance to compensate error caused by element fabrication error and assembly alignment error. The in plane location of the lens has the range of 0.1 mm. Tilts are in 1.7 milli-radians. The in plane rotation can be 17.5 milli-radians. The wedge in two directions are 1.75 milli-radians.

The reason of lower sensitivities of the lens compared to mirror is the two close parallel surface. When displacement happen on both surface, effect are partly canceled.

3.3.4 Cubic beam splitter

Cubic beam splitter is located in a collimated beam path. The effect to the wave front performance is very low, so as the rest of the optical parts. However, changes in these parts will introduce boresight error or beam shift on the detector. The thickness of 1.00 mm change will introduce 0.011 mm beam position on the final detector.

The effect of the beam splitter position error is essentially none.

3.3.5 Beam derotator

Axial position of the derotator will introduce beam shift only. The 1.00 mm of the axial displacement will create 0.036 mm beam shift on the detector. The thickness of the derotator also introduce beam shift. In the real practice, the axial position of the derotator can be used to compensate the fabrication error of the derotator thickness. The tilt change of the derotator only introduces boresight error. The wedge angle also introduces boresight error. Again, the tilt angle can be used to compensate the fabrication of the derotator wedge. The synchronous error (clocking angle) of 1.0 milli-radians of the derotator will introduce 1.40 micron radians of the boresight error in the object space.

Center of the derotator should be on the center of the beam. Any error in the axis offset will cause residual beam shift in the same amount.

3.3.6 Lag angle compensator

Lag angle compensator is a simple flat mirror. The normal position of the mirror surface change in 0.01 mm will introduce 0.014 mm beam position on the detector. The two directional tilts will introduce boresight change of 0.57 micron radians and 0.80 micron-radians respectively for the 0.01 milli-radians changes in tilt angle.

These two ratios are the angular transfer function of the lag angle compensator required by lag angle compensator driver.

All the sensitivities are the effects of one parameter at a time. The combination of the errors need more detailed modeling. One simple estimate can be made based on satitistically reducing the values by square root of the number of the dominant variables. The dominant variables are those hard to fabricate or align.

Table 3. Parametric sensitivities

Primary mirror						
Decenter	X	0.01	mm	0.108	wave	rms wavefront
Decenter	Y	0.01	mm	0.148	wave	rms wavefront
Decenter	Z	0.01	mm	0.143	wave	rms wavefront
Tilt	X	0.017	mr	0.054	wave	rms wavefront
Tilt	Y	0.017	mr	0.039	wave	rms wavefront
Tilt	Z	0.017	mr	0.035	wave	rms wavefront
Secondary mirror						
Decenter	X	0.01	mm	0.104	wave	rms wavefront
Decenter	Y	0.01	mm	0.142	wave	rms wavefront
Decenter	Z	0.01	mm	0.164	wave	rms wavefront
Tilt	X	0.17	mr	0.087	wave	rms wavefront
Tilt	Y	0.17	mr	0.065	wave	rms wavefront
Tilt	Z	0.17	mr	0.053	wave	rms wavefront
Quart wave plate						
Tilt		17.5	mr	0.019	wave	rms wavefront
Thickness		0.01	mm	0.015	wave	rms wavefront
Wedge		1.75	mr	0.051	wave	rms wavefront
Collimating lens						
Decenter	X	0.10	mm	0.044	wave	rms wavefront
Decenter	Y	0.10	mm	0.073	wave	rms wavefront
Decenter	Z	0.01	mm	0.023	wave	rms wavefront
Tilt	X	1.75	mr	0.024	wave	rms wavefront
Tilt	Y	1.75	mr	0.019	wave	rms wavefront
Tilt	Z	17.5	mr	0.077	wave	rms wavefront
Thickness		0.01	mm	0.028	wave	rms wavefront
Wedge	X	1.75	mr	0.081	wave	rms wavefront
Wedge	Y	1.75	mr	0.022	wave	rms wavefront
Cubic beam splitter						
Thickness		1.00	mm	0.011	mm	shift on detector
Beam derotator						
Axial position		1.00	mm	0.036	mm	shift on detector
Tilt (x)		1.00	mr	1.64	mr	boresight error
Synchrnous (z)		1.00	mr	1.40	mr	boresight error

Thichness	0.10	mm	0.058	mm	shift on detector
Wedge	0.01	mr	1.86	mr	boresight error

Lag angle compensator

Normal position (Dec. z)		0.01	mm	0.014	mm	shift on detector
Tilt	X	0.01	mr	0.57	mr	boresight error
Tilt	Y	0.01	mr	0.80	mr	boresight error

3.4 System data

Figures 9 and 10 are the side view and top view of the telescope optics. Some dimensions are somewhat arbitrary, such as the distance between derotator and lag angle compensator, the distance between lag angle compensator and detector. Figure 11 is the recollimating lens fabrication drawing.

Table 4 lists the detailed prescription of the optical system.

Table 4. Optical system priscription

SYNOPSYS AI>
SPE
LENS SPECIFICATION
ID 250 MM CLR TEL W/QW DR - CLRTQD1216

OBJ. DIST.	INFINITE	FOCAL HEIGHT	INFINITE
OBJ. HEIGHT	INFINITE	BACK FOCAL DIST.	0000
MARG. RAY HEIGHT	125.0000	PARAXIAL FOCAL P..	0000
CHEIF RAY HEIGHT	.0000	OVERALL LENGTH	101.1737
MARG. RAY ANGLE	.0000	ENTR. PUPIL POS.	.0000
CHEIF RAY ANGLE	.0802	EXIT PUPIL POS.	-189.1906
DIAIM	-9.9964	GAUSSIAN IM. HT.	.0350
X-OBJ. HEIGHT	INFINITE	X-CHIEF RAY HT.	.0000
X-CHIEF RAY ANGLE	.0802	X-MARG. RAY HT.	.125.0000

WAVELENGTHS 2.07700 2.06700 2.05700
UNITS MM
STOP IS ON SURF. NO. 1
AFOCAL MAGNIFICATION 25.0013
GLOBAL OPTION IS ON
POLARIZATION AND COATINGS ARE IGNORED.

SURF. NO.	RADIUS	THICKNESS	MEDIUM			
1	INFINITE	225.0000	AIR			
2A	-412.13152	-175.00232	-AIR			
CONIC B	-.412131E+13					
AXES A	.412132e+08	CC	-.100000E+01			
3	-89.441144	65.88759	AIR			
CONIC B	.353935E+02					
AXES A	-.562640e+02	CC	-.352705E+01			
4	INFINITE	1.20000	CRQZB	1.51979T	1540.55	UNUSUA
5	INFINITE	6.30513	AIR			
6	180.15394	3.29231	ZNS	2.26422T	6394.74	UNUSUA
CONIC B	-.311206E+02					
AXES A	-.748765E+02	CC	-.678890E+01			
7	28.39464	10.00000	AIR			
CONIC B	.155652E+03					
AXES A	.664807E+02	CC	-.817576E+00			
8	INFINITE	15.00000	FUSILICA	1.43719T	1452.40	UNUSUA
9	INFINITE	.00000	AIR			
10A	INFINITE	15.00000	AIR			
11A	INFINITE	4.49094	ZNS	2.26422T	6394.74	UNUSUA
12A	INFINITE	.00000	AIR			
13	INFINITE	.00000	AIIR			
14	INFINITE	30.00000	AIR			
15A	INFINITE	.00000	-AIR			
16A	INFINITE	-100.00000	-AIR			
17	INFINITE	.00000	AIR			
18	INFINITE	.6035E+06	AIR			

NOTE: ITEMS MARKED "P" OR "S" ARE SUBJECT TO PICKUPS OR SOLVES

DEFORMATION COEFFICIENTS

TILTS AND DECENTERS ALPHA,BETA,GAMMA,AXIS
X-DEC, YDECN, ZDECN

2	TDC 39	SURFACES			
	.000000E+00	.000000E+00	.000000E+00		.000000E+00
	.000000E+00	-.187400E+03	.000000E+00		
2	TDC 29	SURFACES			
	.000000E+00	.000000E+00		.000000E+00	.000000E+00
	.000000E+00	.750000E+01		.000000E+00	
11	TDC 3	SURFACES			
	-.450000E+02	.000000E+00		.000000E+00	.000000E+00

```
        .000000E+000        .000000E+00              .000000E+00
12      TDC     1           SURFACES
        .971609E+00         .000000E+00              .000000E+00   .000000E+00
        .000000E+00         .000000E+00              .000000E+00
SURFACE NO.  13 WILL UNDO TDC OF NO. 12
SURFACE NO. 14 WILL UNDO TDC OF NO. 11
15      TDC     19          SURFACES
        .000000E+00         -.450000E+02             .000000E+00   .000000E+00
        .000000E+00         .000000E+00              .000000E+00
16      TDC     9           SURFACES
        .000000E+00         -.450000E+02             .000000E+00   .000000E+00
        .000000E+00.000000E+00          .000000E+00
SYNOPSYS AI>
CAP
CLEAR APERTURE RADII

(Y-COORDINATE ONLY)

     1      125.000
     2      137.500   USER-ENTERED CAO
                        CENTERED AT (X,Y)              .000000E+00  187.50
     3         30.0000USER-ENTERED CAO
               CENTERED AT (X,Y)         .000000E+00  30.0000
     4         10.0000USER-ENTERED CAO
               CENTERED AT (X,Y)         .000000E+00  10.0000
     5         10.0000USER-ENTERED CAO
               CENTERED AT (X,Y)         .000000E+00  10.0000
     6         10.0000USER-ENTERED CAO
               CENTERED AT (X,Y)         .000000E+00  10.0000
     7         10.0000USER-ENTERED CAO
               CENTERED AT (X,Y)         .000000E+00  10.0000
     8         15.0000             15.0000USER-ENTERED RAO
               CENTERED AT (X,Y)         .000000E+00  7.50000

     9         15.0000             15.0000USER-ENTERED RAO
               CENTERED AT (X,Y)         .000000E+00  7.50000
    10         7.09678
    11         15.0000USER-ENTERED CAO
    12         15.0000USER-ENTERED CAO
    13         13.2639
    14         10.3582
    15         10.0000USER-ENTERED CAO
    16         12.7979
    17         10.0000USER-ENTERED CAO
    18         10.0000USER-ENTERED CAO
```

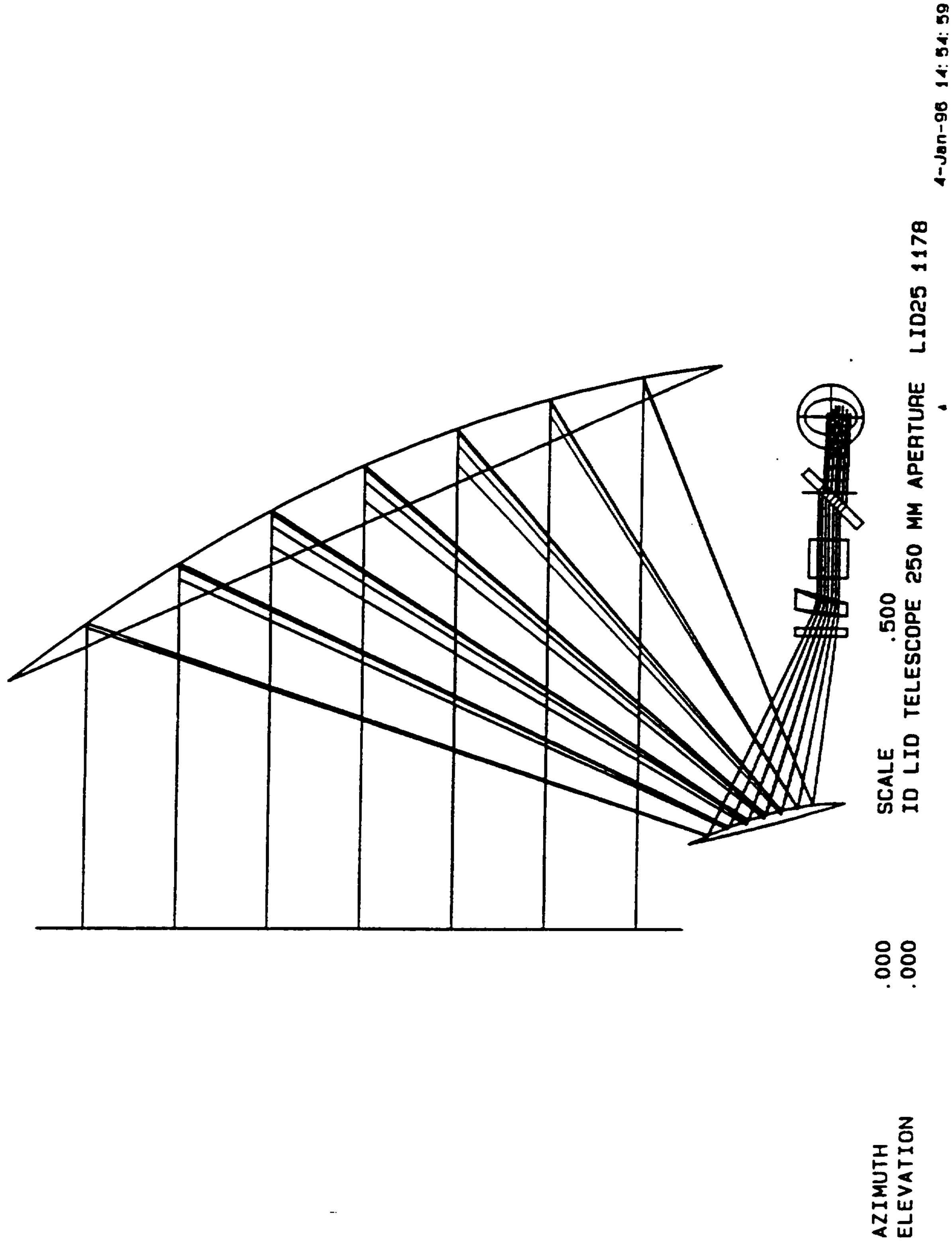

Figure 9. Optical system side view

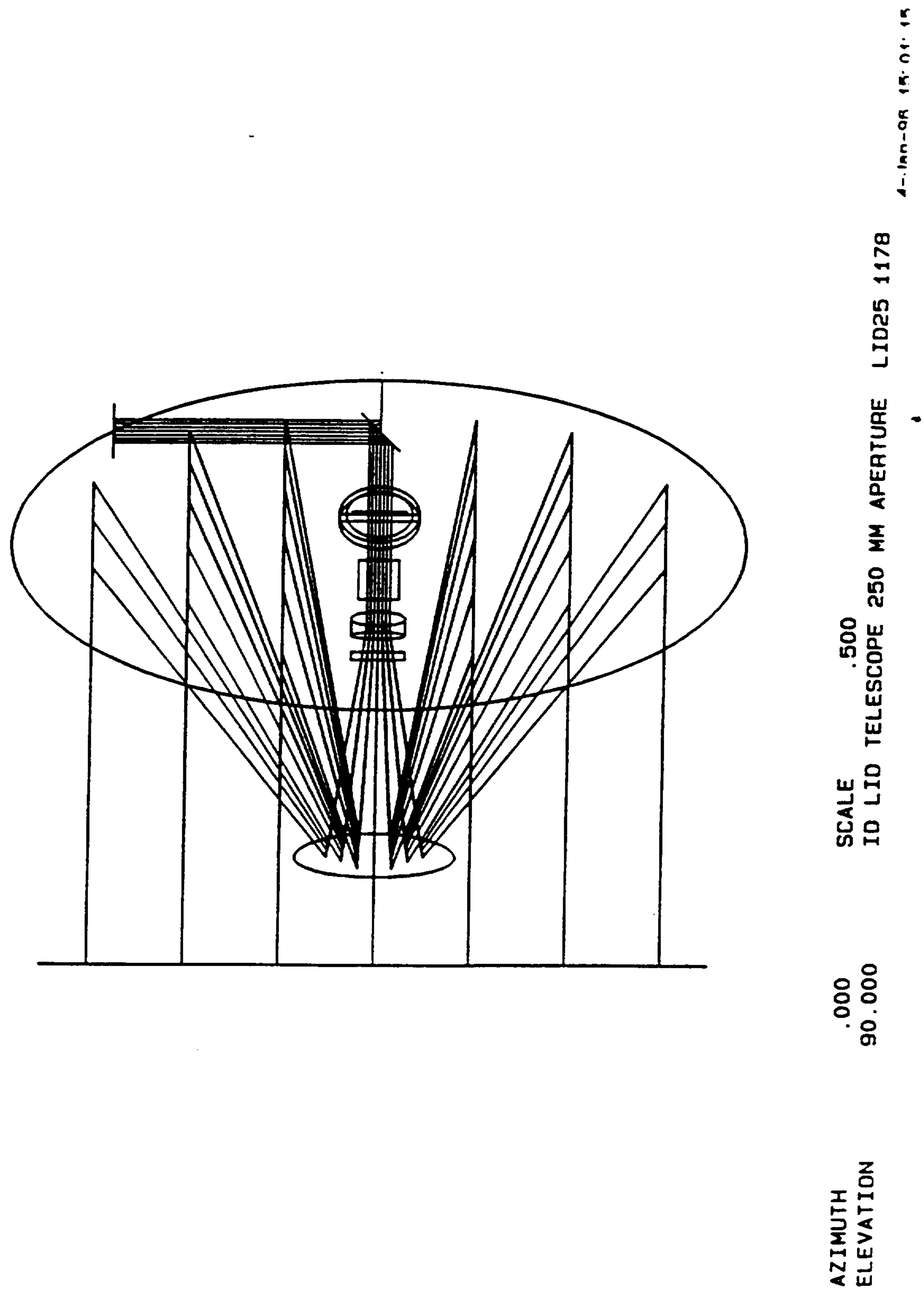

Figure 10. Optical system top view

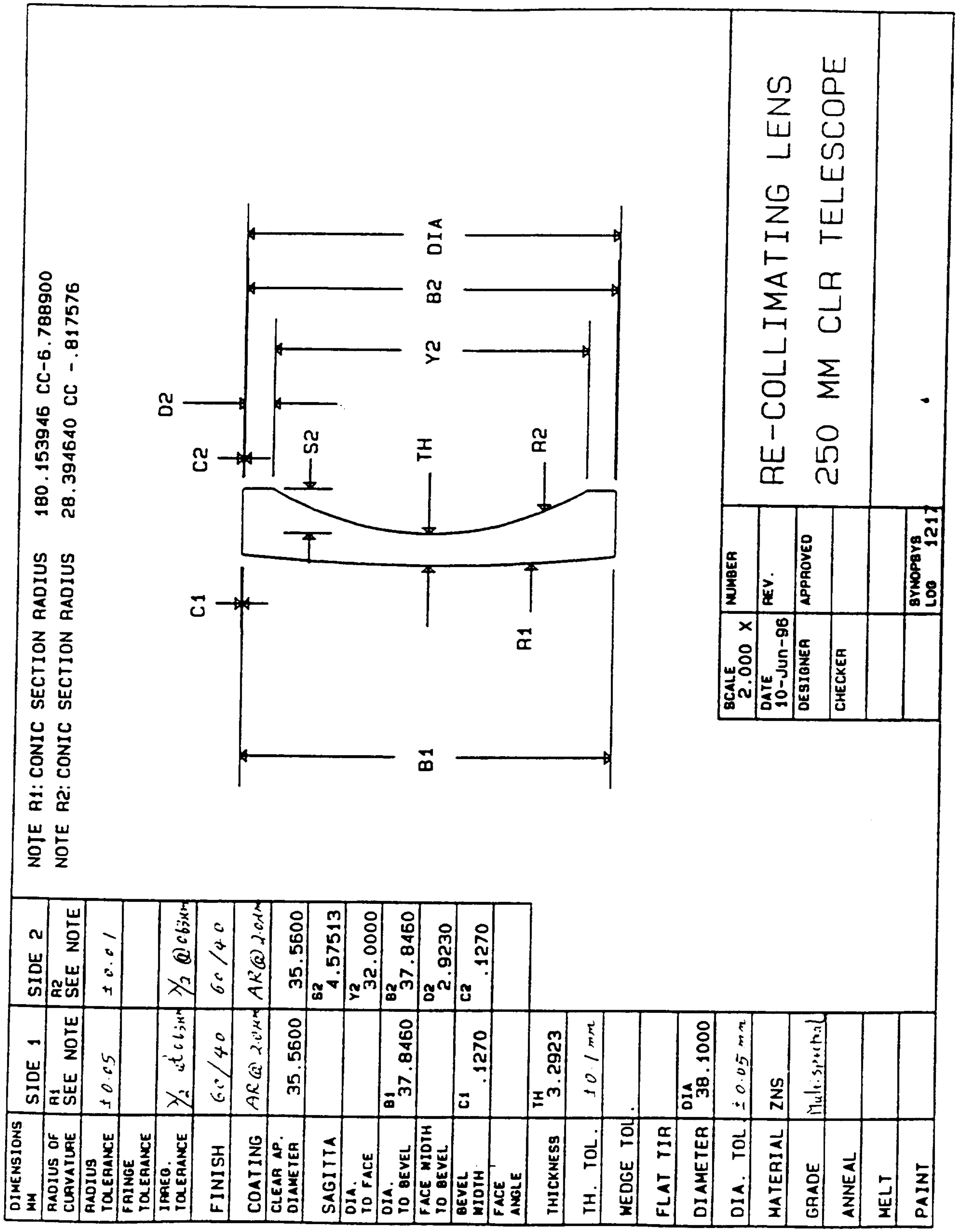

Figure 11. Recollimation fabrication drawing

3.4.1 Telescope

Telescope consists of three optical power elements:

Primary mirror			
Radius of curvature	412.13152	mm	(Concave)
Conic constant	-1.0		(Paraboloid)
Secondary mirror			
Radius of curvature	89.44114	mm	(Convex)
Conic constant	-3.52705		(Hyperboloid)
Recollimating lens			
Radius of curvature 1	180.15394	mm	(Convex)
Conic constant	-6.78890		(Elliposoid)
Radius of curvature 2	28.39464	mm	(Concave)
Conical constant	-0.817576		(Elliposoid)
Central thickness	3.29231	mm	
Material	ZnS		

The Fused silica quarter wave plate is located in the front of the recollimating lens with the thickness of 1.2 mm. The optical material of Re-collimating lens was originally chosen to be Germenium. However, the material was later changed to Zinc Sulfide because it can transmit HeNe laser beam for the purpose of the system alignment. The final wave-front error has been optimized to be about l/200. The index of refraction of ZnS is 2.26 @ 2.0 microns wavelength.

3.4.2 Derotator

The material of beam derotator was originally selected to be Germanium, but like the recollimating lens, it was changed to ZnS to facilitate the system alignment and integration. The tilt angle is 45 degree (the angle between the normal of front surface and rotational axis). The wedge angle is 0.971609 degree (the angle between front and back surface). The central thickness is 4.491 mm. The wedge angle error caused by fabrication can be compensated by adjusting the tilt angle. The thickness error can be compensated by adjusting the axial location of the derotator. However the linear beam offset caused by thickness error will be very small compared to the system requirement. The axial adjustment may not be necessary. The angular offset caused by wedge angle error must be compensated to satisfy the system boresight requirement. See Sensitivity section for the detail.

3.4.3 Lag angle compensator

The lag angle compensator is a simple two dimmensional electro-mechanical addressable folding mirror. The angular beam offset caused by scanning and satellite motion can be compensated by correctly driving the mirror. The linear beam offset on the final detector by this mirror tilts is very small because the tilt angles are very small and the separation between the telescope exit pupil to the lag angle compensator is also small. The linear beam offset on the final detector is the product of lag angle and pupil distance. For the dynamic lag angle change of 80 micron-radians and pupil distance of 87 mm:

Linear offset = 80 X 10 -6 * 87 * 25 = 0.174 mm

Where 25 is the telescope magnification. The linear bean offset is only 1.74 % of the 10 mm beam diameter.

The transfer functions of the lag angle compensator are linear factors of 0.71429 and 0.5 (ratio of mirror tilt and beam deviation) for the horizontal and vertical directions respectively. The tilt ranges for the 80 micro radians dynamic lag angle are:

Horizontal range	= 0.71429 * 80 * 25 = 1.4286 milliradians
Vertical range	= 0.5 * 80 * 25 = 1.0 milliradians

The accuracy of the mirror positions for the 1 micro radians of system boresight requirement are:

Horizontal range	= 0.71429 * 1 * 25 = 17.8573 micro radians
Vertical range	= 0.5 * 1 * 25 = 12.5 micro radians

The swing rates of the mirrors for the 160 microseconds pulse reception time are:

Horizontal rate	= 0.001429 / 0.00016 = 8.931 radians/second
Vertical rate	= 0.001 / 0.00016 = 6.25 radians/second

3.5 Future work on optical subsystem

Complete coating design is needed for all the elements. Detail polarization analysis is necessary upon the completion of coating design. Complete system performance modeling and analysis can be performed. Scattering analysis is necessary to minimize possible signal to noise ratio lose.

4.0 LOW-MASS SCANNER

A study, that was initiated previously, continued under this delivery order to determine the feasibility of using Diffractive and Holographic Optical Elements (DOE and HOE) for scanning the lidar transmitter beam. The diffractive and holographic optical elements have the potential of substantially reducing the mass of the lidar systems and allowing for a much easier spacecraft accommodation design. The diffractive and holographic optical elements change the direction of a laser beam by diffraction, as opposed to the conventional scanning techniques that are based on refraction and reflection. The diffractive and holographic optical elements can potentially reduce the mass of the lidar scanner to less than one fourth of a wedge scanner with the same clear aperture diameter. Wedge scanners have frequently been used in the past for airborne lidar measurements and is now being considered for spaceborne measurements. A wedge scanner element was also specified and acquired by the NASA/MSFC.

As part of this effort, an experimental HOE scanner was specified by the UAH personnel. This scanner element was then designed, fabricated, and delivered to MSFC by the Teledyne Brown Engineering (TBE). This HOE scanner was designed for operation at 2-micron wavelength using dichromated gelatin (DCG) holographic material. The scanning element consists two 15 cm substrates with the holographic material sealed between them. The actual useful area has a 10 cm diameter. Figure 1 shows the HOE scanner in a measurement set up at MSFC. This HOE scanner was characterized at the MSFC Detector Characterization Facility at 2-micron wavelength. The following summerizes the results of these measurements and the desired quantities for operation in a coherent lidar.

	Desired	Measured
Beam Deflection Angle	~30°	28°
Transmission Efficiency		
- First Order	95%	13%
- Zero Order	5%	55%
Wavefront Quality	0.09 waves RMS	0.49 waves RMS

It is recommended that the future work on the low-mass scanner to be continued by concentrating on the Diffractive Optical Element (DOE) techniques.

Figure 1. Holographic Optical Element Scanner

5.0 RELATED ACTIVITIES

5.1 TECHNICAL AND NOAA SPACE-BASED LIDAR WORKING GROUP MEETINGS

UAH personnel attended the NOAA Working Group on Space-Based Lidar Winds Meeting on July 10-12, 1996 in Frisco, Colorado. In this meeting, the status of the NASA/MSFC and UAH 2-micron solid state coherent lidar efforts were described in these meetings. UAH personnel also participated in a technical coordination meeting for the NASA solid state coherent lidar program at NASA Langley Research Center MSFC on October 10, 1996.

5.2 CONFERENCES

Two conference papers, describing some of the work performed under this deliver order, were prepared and presented at the SPIE International Symposium on Optical Science, Engineering, and Instrumentation, in Denver, Colorado, August 4-9, 1996; and the Conference on Lasers and Electro-Optics, in Anaheim, California, June 2-7, 1996. The followings provide the summaries of these papers.

Experimental Evaluation of InGaAs photodetectors for 2-micron coherent lidars

Farzin Amzajerdian
The University Of Alabama in Huntsville
Center for Applied Optics
Huntsville, Alabama 35899
(205)890-6030

ABSTRACT

The heterodyne detection characteristics of InGaAs photodetectors have been experimentally evaluated and their optimum operating parameters and interface requirements for 2-micron coherent lidars have been determined.

SUMMARY

In view of growing interest in eye-safe, solid state coherent lidars using Thulium and Holmium based lasers, it has become necessary to investigate the properties of wideband, 2-micron detection devices and evaluate their performance as heterodyne detectors. For this purpose, a detector measurement system has been developed that is capable of measuring all the necessary detector parameters for optimal designs of optical heterodyne receivers and predicting their sensitivities. Several commercially available InGaAs detectors with different active area sizes have been characterized and their optimum operating and electronic interface parameters have been determined as a function of the signal IF bandwidth requirement.

The detector measurement system utilizes two diode-pumped, single mode, continuous wave, Tm, Ho:YLF lasers. Both lasers can be tuned using an intra-cavity etalon over a wide range of about 22 nm or 1500 GHz centered at 2060 nm. The frequency of one of the lasers can be further controlled by adjusting its resonator length using a piezoelectric (PZT) translation stage. This laser can be continuously tuned over a frequency range of about 1 GHz by applying the appropriate voltage to the PZT stage. Both lasers can produce about 100 mW of single frequency power.

As shown in figure 1, the measurement system can operate the detector in both direct and heterodyne detection modes. When operating in the direct detection mode, the output of the continuously tunable laser is focused by a short focal length lens (~25 mm) to a spot size considerably smaller than the detector effective area to avoid introducing any truncation error in the measurements. For the heterodyne detection measurements, the short focal lens immediately in front of the detector is removed from the optical path. The two laser beams are combined and directed toward the detector by a 50% beamsplitter. By varying the frequency of the continuously tunable laser, the detector heterodyne detection properties can then be determined as a function of heterodyne signal IF frequency. The measured properties include the detector non-linearity coefficient, junction capacitance and resistance as a function of applied bias, AC and DC quantum efficiencies, and voltage-current relationship.

Using the experimental data, the optimal designs of 2-micron optical heterodyne receivers operating in different IF signal bandwidth regimes have been defined and their performance analyzed. Figure 2 is an example of a 2-micron optical heterodyne receiver performance that illustrates the receiver departure from the shot noise-limited operation as the signal IF bandwidth increases beyond a few hundred MHz. For this example, it has been assumed that a 75 μm diameter InGaAs detector is interfaced with a wideband GaAs MESFET transimpedance amplifier. In figure 2, the transimpedance of the amplifier has been adjusted accordingly with the required IF bandwidth for optimum low-noise operation.

References

1. T. G. Blaney, "Signal-to-noise ratio and other characteristics of heterodyne radiation receivers," Space Science Reviews 17, 1975

2. D. L. Spears, "Long-wavelength photodiode development," NASA report no. NAS-5-25717, August 1983

3. J. M. Hunt, J. F. Holmes, and F. Amzajerdian, "Optimum local oscillator levels for coherent detection using photoconductors," Appl. Opt. 27, August 1988

4. J. F. Holmes and B. J. Rask, "Optimum optical local-oscillator power levels for coherent detection with photodiodes," Appl. Opt. 34, February 1995

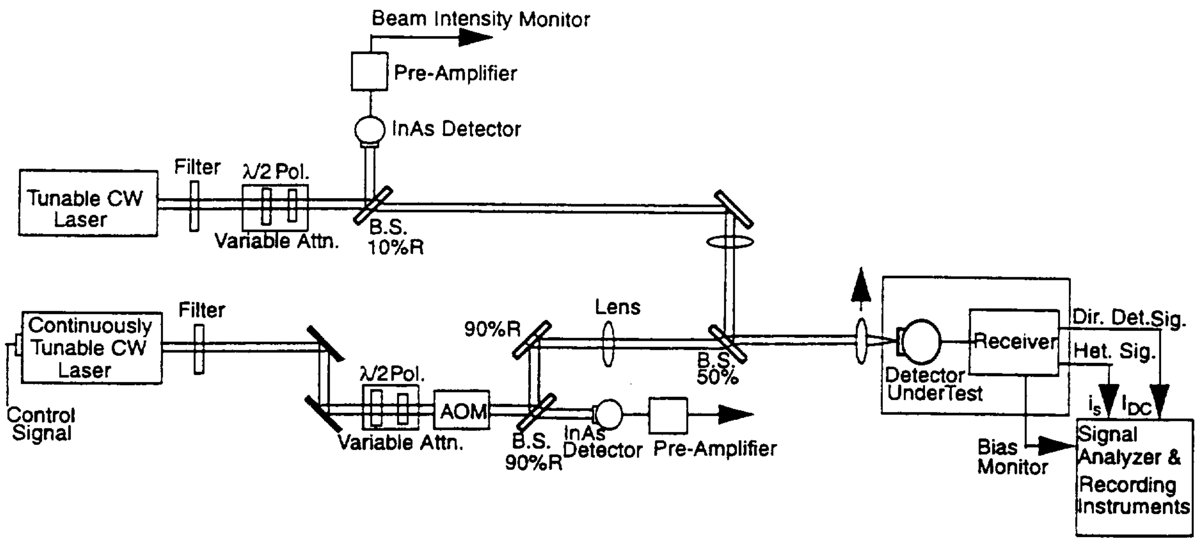

Figure 1. Detector Measurement System.

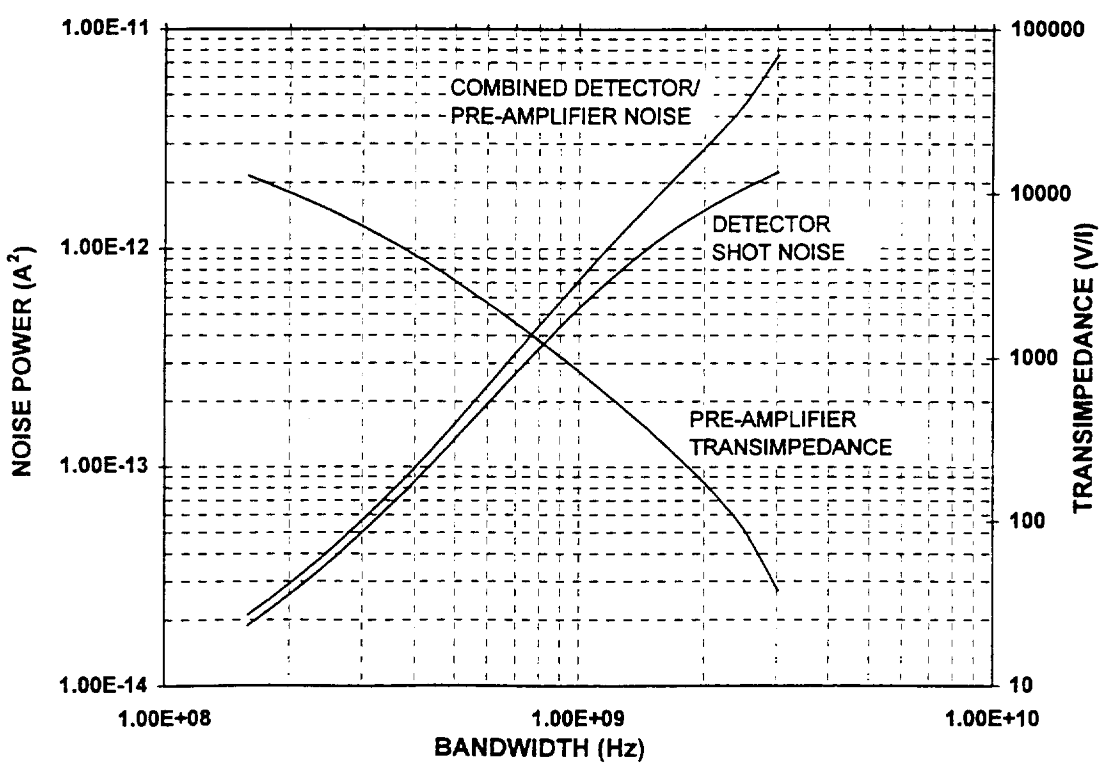

Figure 2. An example of a two-micron coherent lidar receiver performance.

SPIE Proceedings Vol. 2832, August 4-9, 1996

Design and fabrication of a compact lidar telescope

Anees Ahmad, Farzin Amzajerdian, Chen Feng and Ye Li

Center for Applied Optics
The University of Alabama in Huntsville
Huntsville, AL 35899

ABSTRACT

A prototype compact off-axis reflective lidar telescope has been designed and fabricated for remote sensing of atmospheric winds from space and airborne platforms. The 250 mm aperture telescope consists of two mirrors and a collimating lens to achieve a very compact size, without any central obscuration. It has no internal focal point to prevent air breakdown, and the pupil relay optics has also been eliminated. This paper presents the results of optical design and sensitivity analysis along with the predicted performance. The major design issues for lidar systems, particularly the one that utilizes coherent detection for higher sensitivity and Doppler frequency extraction, are the wavefront quality, polarization purity, and a minimum backscattering off the reflective surfaces. These design issues along with the other optical characteristics of this lidar telescope are presented. The effect on the wavefront quality of the tilt, decentration and axial spacing tolerances for the mirrors, collimating lens and quarter wave plate is discussed.
The important optomechanical design features include high rigidity, long term stability and a low fabrication cost. The mirrors are directly bolted and pinned to the support structure to achieve the required alignment accuracies and long term stability. The mirrors and structure are made from aluminum for low cost, and to minimize the adverse effects of differential thermal expansion. The aluminum mirrors are stress relieved and electroless nickel plated prior to single-point diamond machining. The mirrors are also post-polished to achieve a very low surface roughness to minimize the backscattering.

Key words: Lidar telescope, off-axis reflective optics, tolerance analysis, metal mirrors, diamond machining

1. INTRODUCTION

Recent advances in diode-pumped solid lasers have provided the new possibilities for the development of robust, compact and efficient coherent lidars [1]. However, space applications of coherent lidars continue to demand for more compact and robust designs with a higher degree of sensitivity [2,3]. For a space-based coherent lidar, the telescope and scanner along with their associated support structures and control units account for most of the weight and size budget of the system. Therefore, any reduction in their mass will have a major impact on the mission cost. This paper describes the design, performance and fabrication technique of a 250 mm telescope that can significantly reduce the size and weight of a space-based coherent lidar operating at 2 microns wavelength. Although this lidar telescope has been designed and fabricated based on requirements of a space-based instrument, it can directly benefit many airborne applications of coherent lidars.

As opposed to non-coherent lidars, coherent lidars impose stringent wavefront quality, polarization and boresight stability requirements on the telescope. Furthermore, a space-based coherent lidar system must be structurally and thermally robust enough to survive the launch and the space environment.

2. OPTICAL DESIGN

The overall function of the coherent lidar optical system is to expand the laser beam, and direct it towards the atmosphere in a conical scan, to receive the back scattered radiation, and compensate for the wavefront and boresight errors caused by the scanner and spacecraft/aircraft motions. The major lidar system requirements are: (1) beam expanding aperture of 250mm; (2) input laser beam diameter of 10 mm; (3) conical scan rate of 10 RPM; (4) nadir angle of 30 degrees; (5) no internal focal point to avoid air break down in ground system testing; (6) diffraction limited beam quality; (7) lag angle compensation to maintain the boresight to within 1 micro-radian.

The beam expanding telescope is an off-axis catadioptric system, which serves both as the transmitter laser beam expander and as the receiver collecting telescope. Various configurations for the telescope were evaluated against the performance requirements. An off-axis configuration has been selected to eliminate the central obscuration of an on-axis design, which degrades the beam quality due to the diffraction pattern of the obscuration. The off-axis configuration also effectively reduces the back scattering of the transmitted pulses by the front surface of the telescope secondary mirror. A Galilean type of telescope has been employed to eliminate the real focus of the Keplierian type of telescope. The beam wander problem of a Galilean telescope (because of no real exit pupil) can be solved by using additional corrective optics. A catadioptric design with a refractive exit lens has been used to provide enough back-relief space to accommodate the beamsplitter, derotator and lag angle compensator. Figure 1 is the optical layout of this compact two-mirror and one lens off-axis telescope.

The two mirror are a parabola and a hyperbola as in a standard Cassegrain type of telescope. An aspheric negative lens been used to recollimate the beam. Zinc Sulfide has been selected for the re-recollimating lens to facilitate the integration and alignment of telescope using visible HeNe laser. The designed telescope has: (1) a field of view of 0.17 degree to cover the lag angle of the return beam; (2) afocal magnification of 25X to expand the 10 mm beam to a 250 mm diameter; (3) RMS wavefront error of 1/10 wave at the exit pupil for 2.067 micron wavelength; (4) zero obscuration and vignetting; (5) no internal real focus; and (6) two mirrors axial spacing of only 175 mm. Figure 2 shows the wavefront error of this telescope for the transmitted and return beams, and Figure 3 shows the point spread function in the telescope exit space for both the beams.

3. TOLERANCE ANALYSIS

It is easy to design an optical system that can never be built because of its parametric sensitivity, i.e. very tight fabrication and assembly tolerances. Parametric sensitivity of the telescope has been analyzed to determine its performance for real fabrication and assembly tolerances. The details of wavefront error and boresight sensitivity analysis for the two mirrors and collimator lens are given in Reference 3 with the wavefront error for the ideal telescope, zero allowance for fabrication and assembly tolerance, is $\lambda/200$ P-V. Table 2 lists the boresight errors induced due to all these tolerances. The most sensitive element is the primary mirror. To maintain 1/10 λ RMS wavefront and a one micro-radians boresight system performance, the decenters should be less then 0.01 mm, and the tilts should be less than 0.017 milli-radians.

4. OPTOMECHANICAL DESIGN

A simple approach was used for the optomechanical design of the prototype telescope to minimize the fabrication cost and time. The telescope consists of a box-type support structure, a primary and a secondary mirror, and a quarter-wave plate and a collimating lens as shown in Figure 3. The primary mirror is designed to be back-surface mounted and the secondary mirror front-surface mounted so that their mounting surfaces on the support structure can be machined from the same side in one setup. The mirror and support structure are made from 6061-T6 aluminum alloy to minimize the problems due to differential thermal expansion as a result of the ambient temperature variations. The primary and secondary mirrors are ideally suited for diamond machining because of their off-axis aspherical configuration, and the large size of the primary mirror. A brief description of some of the important design features of the two mirrors and the support structure is given in the following sections.

4.1 Design of mirrors

The primary mirror has a clear aperture diameter of 250 mm and its mechanical axis is offset 187.5 mm from the optical axis. The diameter of primary mirror is 270 mm to provide an extra 10 mm margin around the edges to account for the edge roll-off and other polishing and machining errors. The back of the mirror is designed to be orthogonal to the optical axis to simplify the design of the diamond machining fixture. This design approach results in a mirror of non-uniform thickness, the top edge being much thicker than the edge closest to the optical axis. Although this non-uniform thickness of the mirror compromises its thermal performance, it results in substantial cost savings in the fabrication of the mirror blank and the diamond machining fixture.

The mirror is mounted to the support structure by using three screws and two dowel pins located on a common bolt circle of 200 mm diameter. The three 0.25-20 screws are equally spaced 120° apart, while the two 6.35 mm (0.25") diameter dowel pins are located 180° apart from each other as shown in Figure 4. The threaded holes for the screws and a precision hole and a slot for the two pins are machined into the back surface of the mirror. Three small raised pads are provided around the threaded holes for a semi-kinematic mounting of the mirror to the structure and the machining fixture to minimize mirror distortion. The front of the primary mirror substrate is made spherical to a best fit radius of 555 mm to facilitate its rough machining. A small flat surface is also provided at the top outer edge for alignment and machining reference purposes. The secondary mirror is relatively much smaller in size (60 mm diameter), with an offset of only 30 mm between its mechanical axis and the telescope optical axis. The back surface of this mirror is also designed to be orthogonal to the optical axis to simplify the design of its diamond machining fixture. Since the secondary mirror is much thinner than the primary mirror, a flange is provided for its mounting features as depicted in Figure 5. This flange could not be made full round because of the space constraints, thereby resulting in a slightly modified spacing between the screws. In this case, four screws have been provided for adequate mounting instead of the three screws normally used in kinematic mounting designs. The precision hole and slot for the two dowel pins are located 180° apart on the same bolt circle as the screws. The front surface of the secondary mirror substrate was made flat and tapered to minimize the fabrication cost.

4.2 Design of diamond machining fixtures

Since the back surfaces of both mirrors are normal to the optical axis, the design of their diamond machining fixtures is fairly simple and straight forward. Both fixtures basically consist of flat circular plates with appropriate mounting features for the mirrors. These fixtures are designed to support and diamond machine two mirrors each simultaneously to minimize the imbalance problems due to centrifugal forces during machining.

The diamond machining fixture for the primary mirror consists of two circular plates, 660 mm in diameter and 25 and 50 mm thick as shown in Figure 6. A two-piece fixture design is needed in this case because of the back-mounting configuration of the primary mirror and the design of the chuck of diamond machine. The 50 mm thick plate is designed to mount to the chuck directly using six 0.625-13 screws located on 356 mm (14") diameter bolt circle. The 25 mm thick plate has two 6.35 mm (0.25") diameter dowel pins and three counter-bored clearance holes for 0.25-20 screws on 200 mm diameter bolt circles, whose centers are located 187.5 mm (offset distance) from the center (spin axis) of the plate. The two mirrors are bolted to this plate first, and then this 25 mm thick plate is designed to be bolted to the other 50 mm thick plate.

The diamond machining fixture for the secondary mirror is a simple 140 mm diameter x 19 mm thick circular plate as illustrated in Figure 7. It is also designed to support two mirrors simultaneously for machining. This fixture has two dowel pins and four 6-32 threaded holes on a common bolt circle for each mirror. The centers of these bolt circles are located at 30 mm (offset distance) from the center (spin axis) of the plate.

4.3 Design of support structure

A box-type structure has been designed to support the two mirrors and other components of the telescope as depicted in Figure 8. This design configuration was selected to minimize the weight and cost of fabrication. The support structure consists of a front and a back plate, which are connected by a top and a bottom plate, plus six gussets (three on each side). All these ten 0.25" thick plates can be machined individually, and then bolted and pinned together to produce a very rigid and lightweight support structure. Raised areas have been provided on the front and back plates for mounting the two mirrors. Extra material is provided on the raised areas so that these mounting surfaces can be machined flat and parallel to each other from the same side in the assembled box to obtain the correct axial spacing between the two mirrors.

The front plate has four 6-32 threaded holes and two 3 mm (0.125") diameter dowel pins for securely mounting the secondary mirror. The back plate has three clearance holes for the 0.25-20 screws and two 6.35 mm (0.25") diameter dowel pins for mounting the primary mirror. Mounting features have also been provided in the bottom plate to install the quarter-wave plate and collimating lens linear translation stage. A number of additional threaded holes are provided in different plates of the structure to install other components of the lidar system such as the wedge scanner, derotator and beamsplitter.

4.4 Design of quarter-wave plate and collimating lens mounts

Since the alignment tolerances for the quarter-wave plate and collimating lens are quite loose, simple bonded type mounts have been designed for these two optical elements as depicted in Figure 10. This bonded design not only simplifies the design of the mounts resulting in low fabrication cost, it also minimizes the thermally induced stresses in the optics due to differential expansion as a result of changes in the ambient temperature. The 25 mm diameter x 1 mm thick quartz quarter-wave plate is directly bonded into an L-shaped aluminum bracket using an appropriate RTV. As the axial spacing and decentration of this flat optical element are not critical, only two screws are used for securing its mount to the structure.

The collimating lens mount is similar in design, but it is designed to mount to a linear translation stage for varying the focal length of the telescope from 100 meters to infinity. Although only a small off-axis part of the aspherical lens is needed, a complete 37 mm diameter circular lens, which is centered on the optical axis, is used. This configuration simplifies the mounting design and fabrication of the lens. The Cleartran (ZnS) lens is directly bonded into its aluminum mount using RTV.

5. FABRICATION OF MIRRORS

As the support structure, mirrors and other optical mounts are all made from 6061-T6 aluminum alloy, these components can be machined using standard tooling and methods for precision optical applications. All these parts were rough machined and then stress-relieved prior to finish machining of the critical mounting features. A brief description of the fabrication procedures employed for the two mirrors and their diamond machining fixtures is given as follows.

5.1 Fabrication of diamond machining fixtures

The surface figure of the finished mirrors directly depends on the quality of the fixtures used for their diamond machining. Therefore, it is very critical to achieve best possible flatness on these fixtures to prevent distortion of the mirrors when mounted to these fixtures during diamond machining. After rough machining and stress relieving, the 50 mm thick primary mirror fixture plate was mounted on the chuck of Moore diamond turning machine. The outer diameter and front surface of this plate were then diamond machined to obtain a highly flat surface. The 25 mm thick fixture platewas then bolted to the 50 mm thick plate and its front surface was diamond machined. This plate was then removed, turned over and then rebolted to the 50 mm thick plate to diamond machine the other side of the plate. This diamond machining of all mating surfaces of the fixture plates eliminated the possibility of any warping when the plates and mirrors are rigidly bolted to each other.

5.2 Fabrication of mirrors

The rough machined mirrors were thermally cycled to enhance their long term stability prior to diamond machining. The mirror were placed in a boiling water bath for 5 minutes, then removed and brought to the room temperature. Next, they were held above the liquid nitrogen (LN2) surface in a container for a few minutes and then submerged in it until the LN2 stopped boiling. Next, they were again put into the boiling water for one minute. This thermal cycle was repeated three times.Then the three pads on the back side of primary mirrors were lapped flat and coplanar before installing the two mirrors on the 25 mm thick plate. This plate was then bolted to the 50 mm plate already installed on the chuck of the diamond turning machine. The mirrors were then diamond machined to the required aspherical shape using a single point tool. These mirrors were then plated with a thin layer (125 - 150 microns thick) of electroless nickel (11% phosphor by weight) before finish diamond machining them again.

A similar procedure was followed for fabricating the secondary mirrors. This included thermally cycling the mirrors, lapping the back surfaces, then diamond machining the desired aspherical surface in bare aluminum. The mirrors were then electroless nickel plated, and finally finish diamond machined.

The surface roughness obtained on these mirrors after diamond machining was of the order of 200-300 A on the primary mirrors and 50 A on the secondary mirrors. This level of surface roughness is deemed too high for lidar applications because it can produce excessive scattering and back reflection especially from the secondary mirror. Therefore, both the primary and secondary mirrors were post polished using diamond paste and aluminum oxide. A surface roughness of better than 15A and 50 A was obtained on the secondary and primary mirrors respectively after polishing. The figure error of both mirrors was controlled to one wave peak-valley at HeNe wavelength. Then, the two mirrors were coated with gold and a protective material for high reflectivity and durability.

6. CONCLUSIONS

The optical design and sensitivity analysis of a compact off-axis prototype telescope for space-based lidar applications has been presented. The optomechanical design emphasizes the low cost and lightweight by using aluminum for the two mirrors and other structural parts. A very stable and rugged telescope has been designed by using simple designs and standard precision machining methods. The two mirrors are rigidly bolted to a lightweight box-type of structure, requiring no alignment at assembly. The next phase of work will involve assembly, integration and testing of the telescope. The telescope performance will be then demonstrated in a coherent lidar system along with the other optical subsystems and components including the scanner and the signal beam derotator. This work was supported by the Electro-Otics Branch of NASA Marshall Space Flight Center.

7. REFERENCES

1. Sammy W. Henderson et al, "Coherent Laser Radar at 2 mm using solid state lasers" IEEE Transactions on Geoscience and Remote Sensing 31 (1), 4-15, 1993

2. Michael J. Kavaya et al, "Direct global measurements of tropospheric winds employing a simplified coherent laser radar using fully scalable technology and technique," SPIE Proceedings Vol. 2214-31, 1994.

3. C. Feng, A. Ahmad and F. Amzajerdian, "Design and analysis of a spaceborne lidar telescope," SPIE Proceedings Vol. 2540-09, 1995.

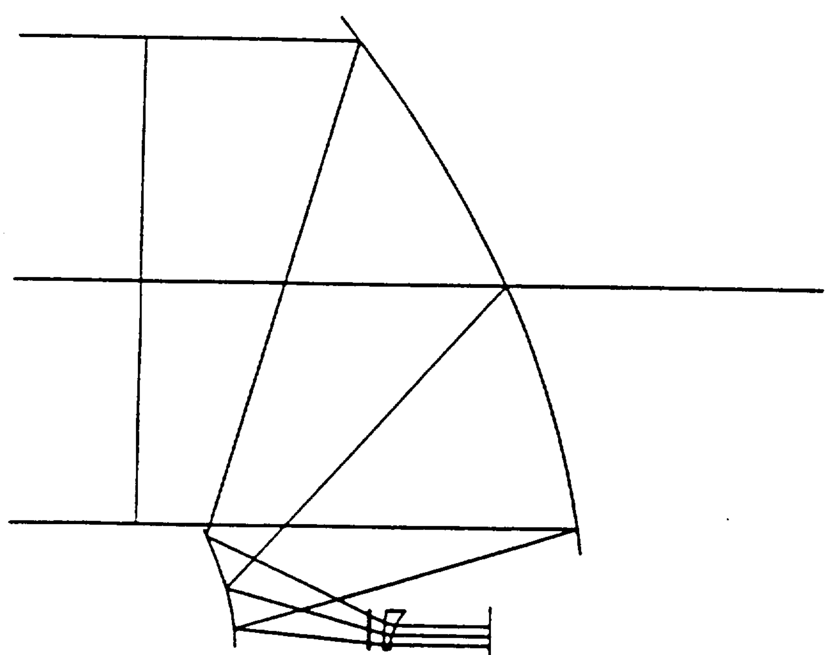

Figure 1. Optical layout of the telescope showing configuration of major optical elements.

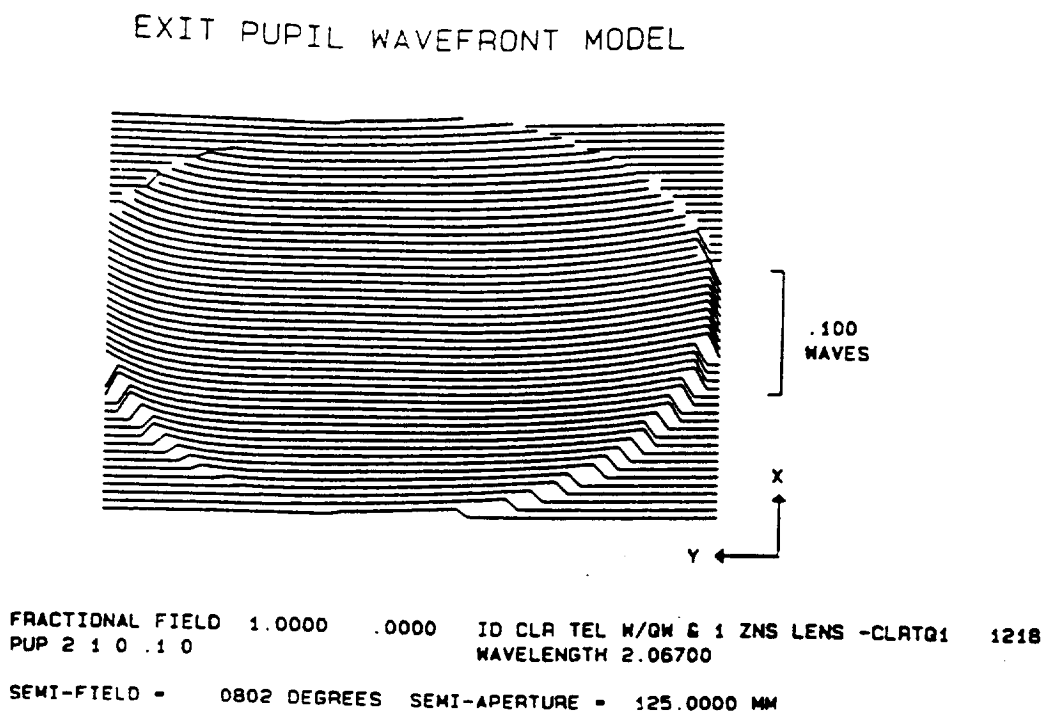

Figure 2(a). Wavefront error in telescope exit space.

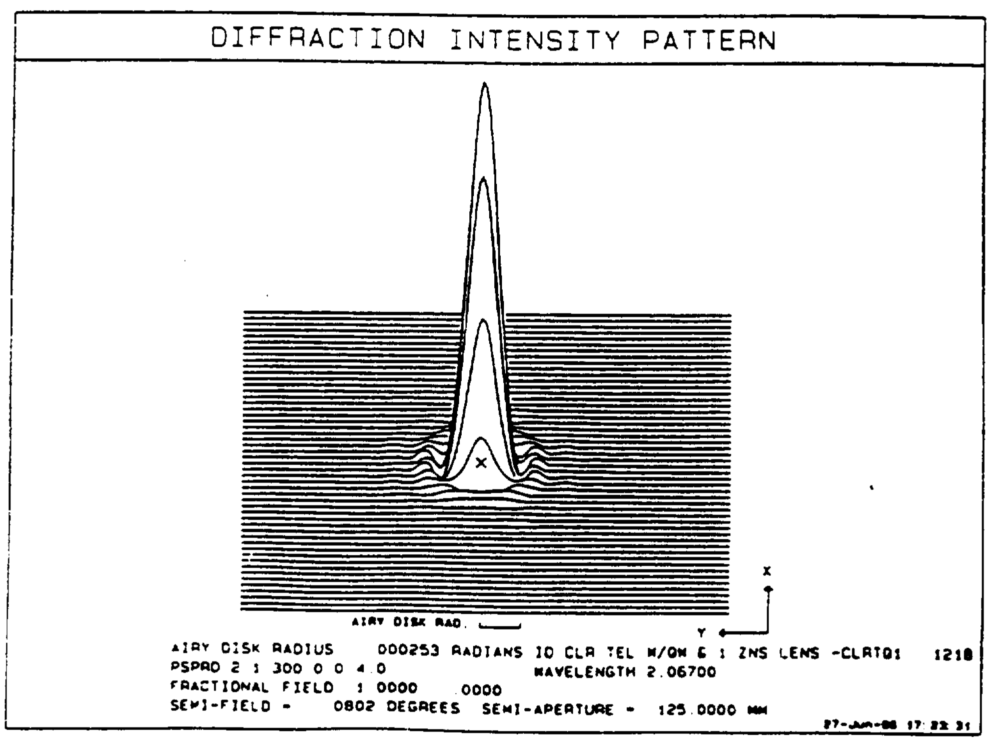

Figure 2(b). Point spread function in the exit space.

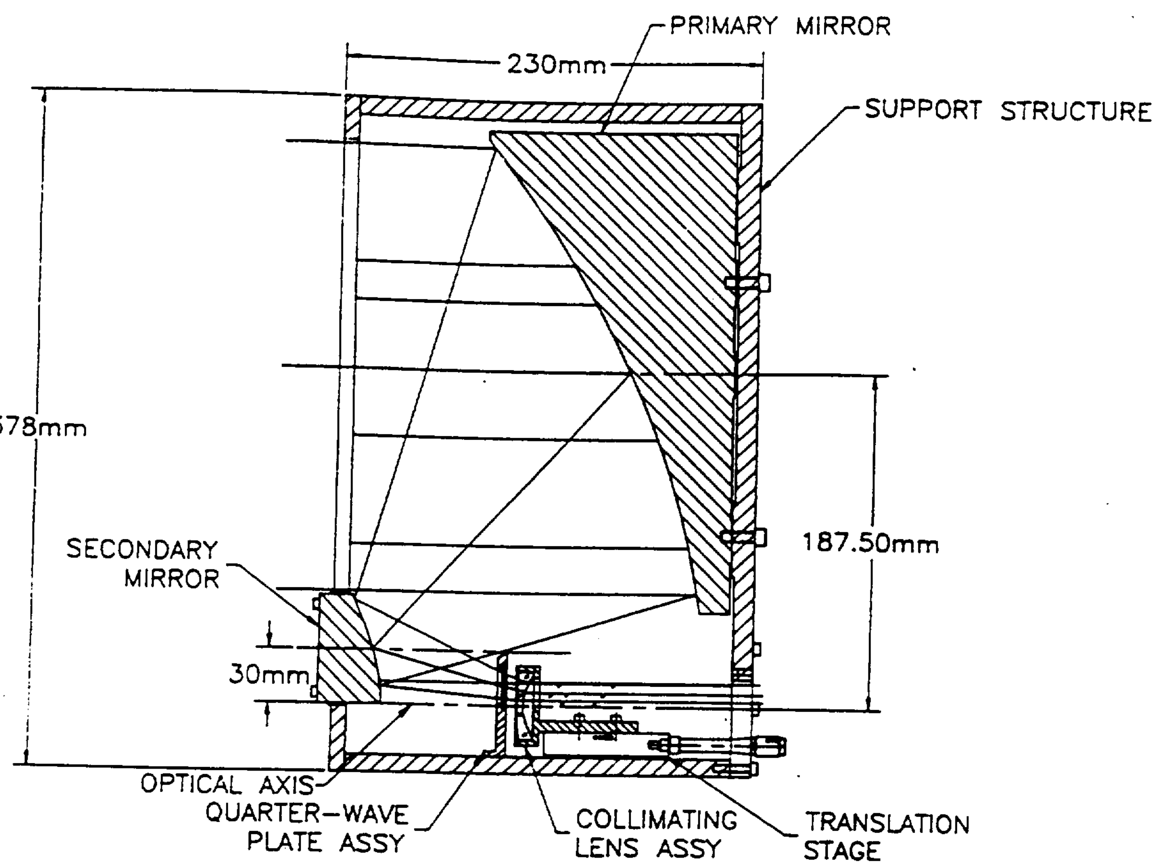

Figure 3. The telescope assembly showing major optical and structural parts.

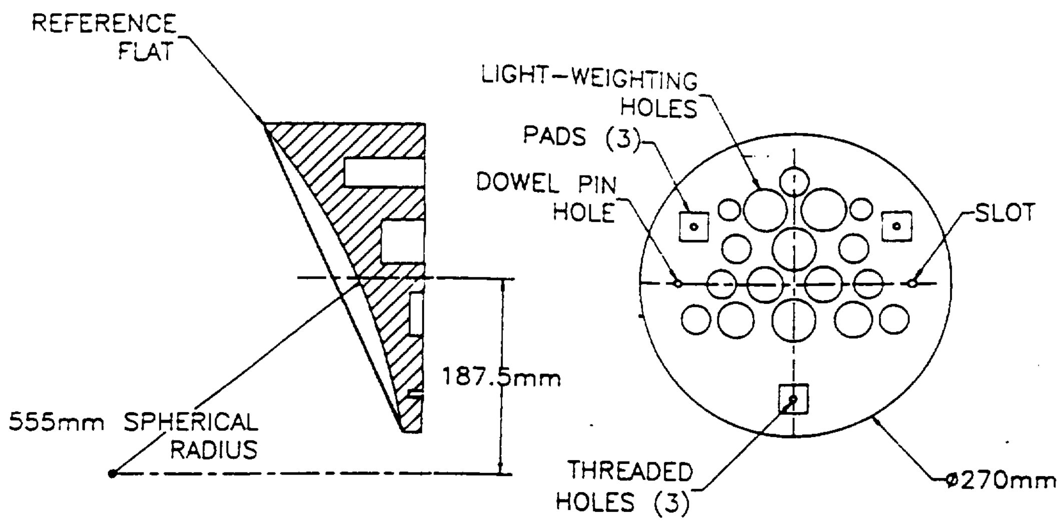

Figure 4. The mounting features and light weighting scheme for the primary mirror.

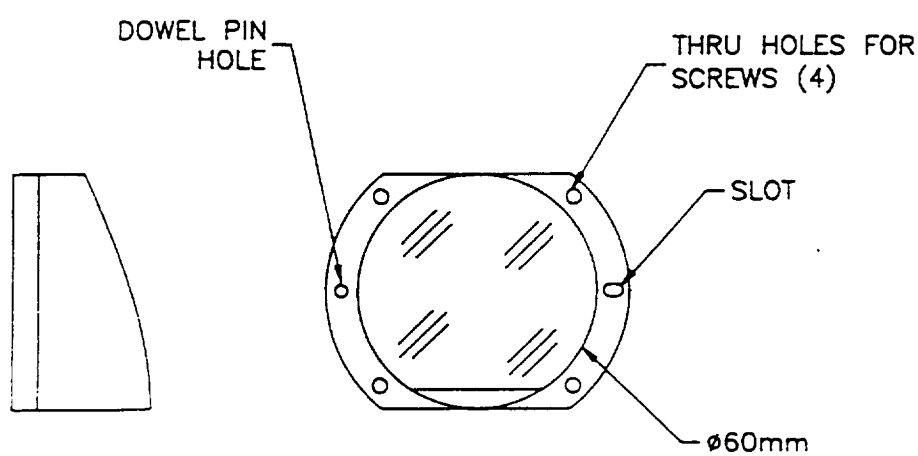

Figure 5. The mechanical design features of the secondary mirror.

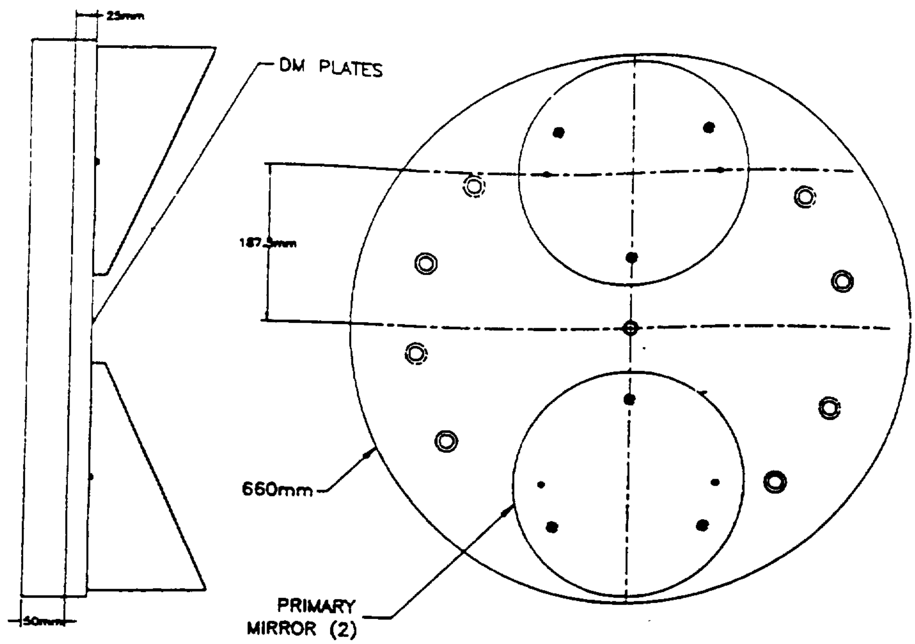

Figure 6. The primary mirror diamond machining fixture

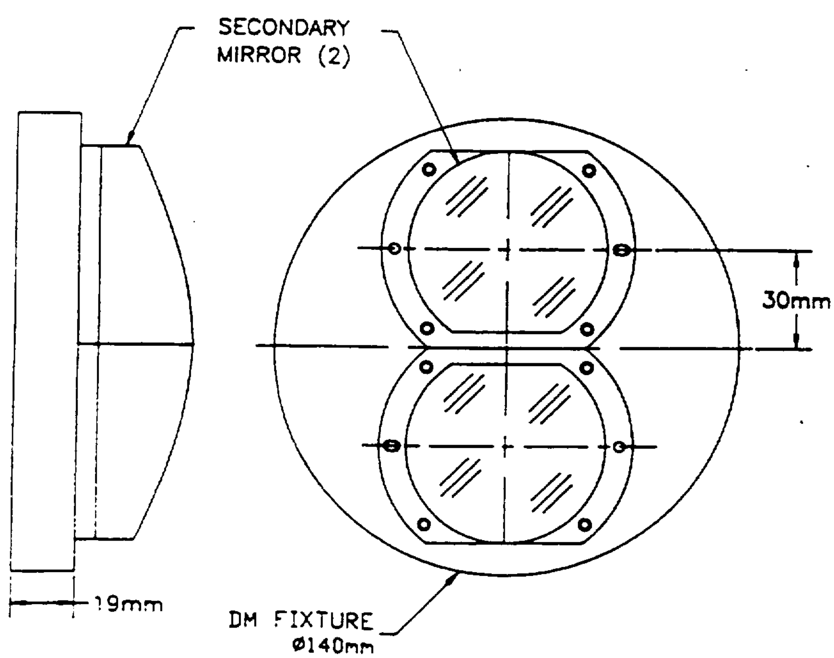

Figure 7. The secondary mirror diamond machining fixture.

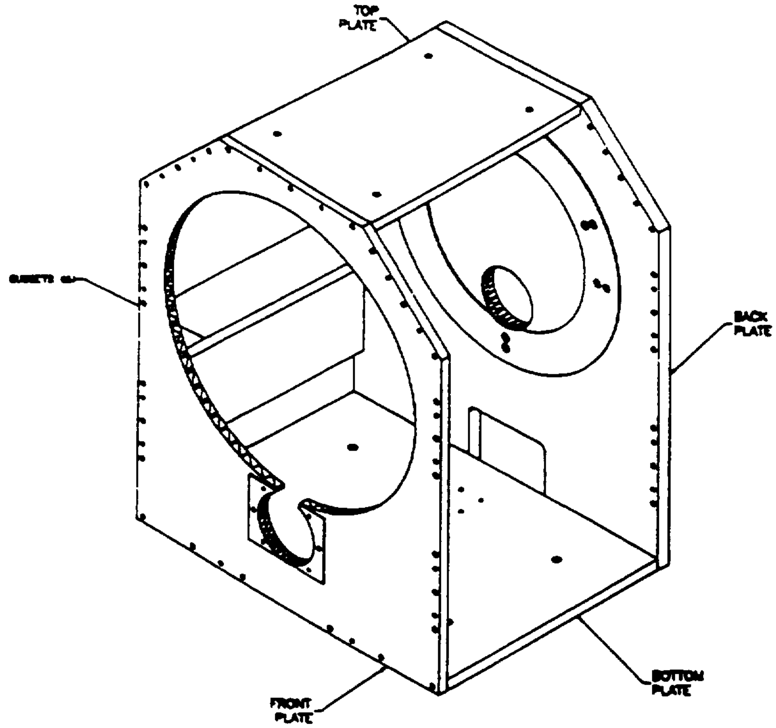

Figure 8. The telescope support structure showing bolted and pinned construction.

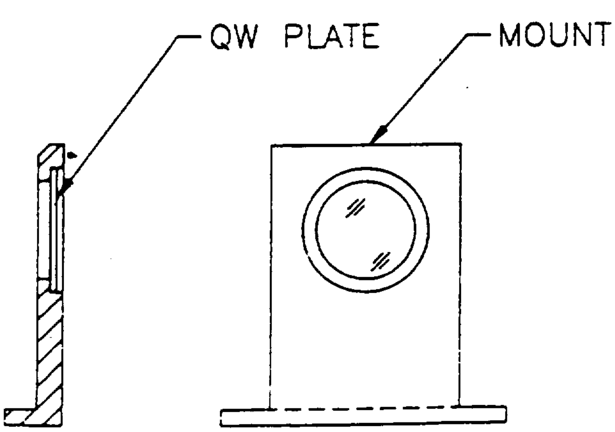

Figure 9(a). The bonded type optical mount for quarter-wave plate.

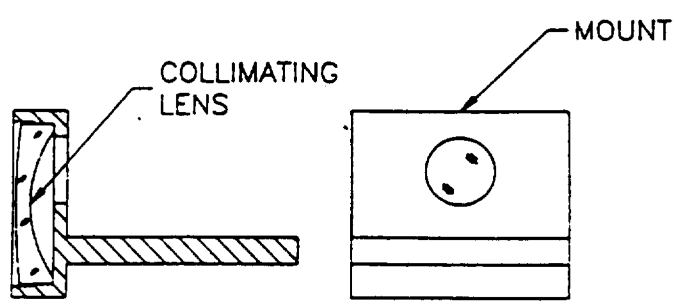

Figure 9(b). The bonded type optical mounts for collimating lens.

REFERENCES

1. Farzin Amzajerdian, "Analysis of measurements for solid state laser remote lidar system," Final Report, Contract No. NAS8-38609/D.O. 77, September 31, 1994

2. Farzin Amzajerdian, "Analysis of measurements for solid state lidar development," Final Report, Contract No. NAS8-38609/D.O. 118, August 13, 1996

3. D.L. Spears and R.H. Kingston, "Anomalous noise behavior in wide-bandwidth photodiodes in heterodyne and background-limited operation," Appl. Phys. Lett. 34, May 1979.

4. R. G. Frehlich and M. J. Kavaya, "Coherent laser radar performance for general atmospheric refractive turbulence," Appl. 30, December 1991

5. R.T. Ku and D.L. Spears, "High-sensitivity infrared heterodyne radiometer using a tunable-diode-laser local oscillator," Opt. Lett. 1, September 1977.

6. R. G. Frehlich, "Estimation of the nonlinearity of a photodetector," Appl. Opt. 31, October 1992.

7. J. F. Holmes and B. J. Rask, "Optimum optical local-oscillator power levels for coherent detection with photodiodes," Appl. Opt. 34, February 1995

8. J. M. Hunt, J. F. Holmes, and F. amzajerdian, "Optimum local oscillator levels for coherent detection using photoconductors," Appl. Opt. 27, August 1988

9. M.J. Post and R.E. Cupp, "Optimizing a pulsed Doppler lidar," Appl. Opt. 29, October 1990.

10. H. van de Stadt, "Heterodyne detection at a wavelength of 3.39 μm for astronomical purposes," Astron. and Astrophys. 36, 341-348, 1974.

11. J. J. Morikuni, A. Dharchoudhury, Y. Leblebici, and S. M. Kang, "Improvements to the standard theory for photoreceiver noise," IEEE J. Lightwave Technol., v. 12, July 1994.

14. "Definition and Preliminary Design of the LAWS (Laser Atmospheric Wind Sounder) Phase II Final Report Volume II," NASA Contract No. NAS8-37589, GE Astro Space Division, September 1992.

15. "Design Definition of the Laser Atmospheric Wind Sounder (LAWS)", Lockheed Missiles & Space Company, Huntsville, AL, Phase II Final Report, Contract No. NAS8-37590, November 1992. Pages from 3-60 to 3-70.

16. J. Bilbro, G. Fichtl, D. Fitzjarrald, M. Krause, and R. Lee, "Airborne Doppler lidar wind field measurements", Am. Met. Soc. 65, April 1984.

17. M.J. Kavaya, G.D. Spiers, E.S. Lobl, J. Rothermel, and V.W. Keller, "Direct global measurements of tropospheric winds employing a simplified coherent laser radar using fully scalable technology and technique," Proc. Of SPIE International Symposium on Optical Engineering in Aerospace Sensing, Technical Conference on Space Instrumentation and Dual-Use Technologies, 2214-31, Apr 6, 1994.

18. J.G. Hawley, R. Targ, S.W. Henderson, C.P. Hale, M.J. Kavaya, and D. Moerder, "Coherent launch-site atmospheric wind sounder: theory and experiment" Appl. Opt. 32, August 1993.

19. R.T. Menzies, "Doppler lidar atmospheric wind sensor: a comparative performance evaluations for global measurement applications from earth orbit," Appl. Opt. 25, August 1986.

20. W.E. Baker, G.D. Emmitt, P. Robertson, R.M. Atlas, J.E. Molinari, D.A. Bowdle, J. Paegle, R.M. Hardesty, R.T. Menzies, T.N. Krishnamurti, R.A. Brown, M.J. Post, J.R. Anderson, A. C. Lorenc, T.L. Miller, and J. McElroy, "Lidar measured winds from space: An essential component for weather and climate prediction," To be published in the Bulletin of American Meteorological Society, 1995.

NASA
National Aeronautics and Space Agency

Report Document Page

1. Report No.	2. Government Accession No.	3. Recipient's Catalog No.
4. Title and Subtitle Analyses of Technology for Solid State Coherent Lidar		5. Report Due June 30, 1997
		6. Performing Organization Code University of Alabama in Huntsville
7. Aurthor(s) Farzin Amzajerdian		8. Performing Organization Report No.
		10. Work Unit No.
9. Performing Organization Name and Address University of Alabama in Huntsville Huntsville, Alabama 35899		11. Contract or Grant No. NAS8-38609 D.O. 150
12. Sponsoring Agency Name and Address National Aeronautics and Space Administration Washington, D.C. 20546-001 Marshall Space Flight Center, AL 35812		13. Type of report and Period covered Oct. 1, 1995 - June 30, 1997
		14. Sponsoring Agency Code
15. Supplementary Notes		
16. Abstract		
17. Key Words (Suggested by Author(s))	18. Distribution Statement	

19. Security Class. (of this report)	20. Security Class. (of this page)	21. No. of pages	22. Price
Unclassified	Unclassified	85	

NASA FORM 1626 OCT 86